

2015

Cellular properties of the medial entorhinal cortex as possible mechanisms of spatial processing

<https://hdl.handle.net/2144/16251>

Downloaded from DSpace Repository, DSpace Institution's institutional repository

BOSTON UNIVERSITY
SCHOOL OF MEDICINE

Dissertation

**CELLULAR PROPERTIES OF THE MEDIAL ENTORHINAL CORTEX AS
POSSIBLE MECHANISMS OF SPATIAL PROCESSING**

by

CHRISTOPHER FRANK SHAY

B.S., Northeastern University, 2009

Submitted in partial fulfillment of the
requirements for the degree of
Doctor of Philosophy

2015

© 2015
CHRISTOPHER FRANK SHAY
All rights reserved

Approved by

First Reader

Michael E. Hasselmo, D. Phil.
Professor of Psychological and Brain Sciences

Second Reader

Ian Davison, Ph.D.
Associate Professor of Biology

Third Reader

John Lisman, Ph.D.
Professor of Biology, Brandeis University

ACKNOWLEDGMENTS

No accomplishment is achieved alone. Many wonderful people have made either direct or indirect contributions to the work presented in this thesis. First and foremost, I must thank my advisor Dr. Michael Hasselmo. I could not have asked for a better mentor. Dr. Hasselmo has provided unwavering support throughout my graduate career. He is as kind as he is intelligent, just two of the many reasons why working with him has been an honor.

I thank my committee members, Dr. Jen-Wei Lin, Dr. Ian Davison, Dr. Timothy Gardner, and Dr. John Lisman for their guidance and expertise during this process. Thanks to all my colleagues in the Hasselmo lab that I have had the privilege of working with: Dr. Mark Brandon, Dr. Kishan Gupta, Dr. Vardhan Dani, Dr. Nathan Schulteiss, Caitlin K. Monaghan, Jason R. Climer, Dr. James R. Hinman, G.W. Chapman IV, Dr. Ian Boardman, Dr. Motoharu Yoshida, Dr. Yusuke Tsuno, Dr. Michele Ferrante, Dr. Ehren L. Newman, and Dr. James G. Heys. I would also like to thank Dr. Nelson Spruston and Dr. Bernardo Rudy for extending their resources and expertise towards training me.

I would like to give a special thanks to Mikele Rauch. Over the years her work has encouraged personal awareness and growth. I thank my parents Richard Shay, Denise Shay, Deborah Mitchell, and Joseph Mitchell for their love and support. I thank my grandfather, Frank Caparco, who taught me the importance of education and hard work. I thank my partner Anna Brousaides who has given me the most precious gift, my son Theodore. Without her sacrifice and love this work would not be possible. Lastly, I thank my son Theodore for the inspiration and joy he brings to my life everyday.

**CELLULAR PROPERTIES OF THE MEDIAL ENTORHINAL CORTEX AS
POSSIBLE MECHANISMS OF SPATIAL PROCESSING**

CHRISTOPHER FRANK SHAY

Boston University School of Medicine, 2015

Major Professor: Michael E. Hasselmo, D. Phil., Professor of Psychological and Brain Sciences

ABSTRACT

Cells of the rodent medial entorhinal cortex (EC) possess cellular properties hypothesized to underlie the spatially periodic firing behaviors of ‘grid cells’ (GC) observed *in vivo*. Computational models have simulated experimental GC data, but a consensus as to what mechanism(s) generate GC properties has not been reached. Using whole cell patch-clamp and computational modeling techniques this thesis investigates resonance, rebound spiking and persistent spiking properties of medial EC cells to test potential mechanisms generating GC firing.

The first experiment tested the voltage dependence of resonance frequency in layer II medial EC stellate cells. Some GC models use interference between velocity-controlled oscillators to generate GCs. These interference mechanisms work best with a linear relationship between voltage and resonance frequency. Experimental results showed resonance frequency decreased linearly with membrane potential depolarization,

suggesting resonance properties could support the generation of GCs. Resonance appeared in medial EC but not lateral EC consistent with location of GCs.

The second experiment tested predictions of a recent network model that generates GCs using medial EC stellate cell resonance and rebound spiking properties. Sinusoidal oscillations superimposed with hyperpolarizing currents were delivered to layer II stellate cells. Results showed that relative to the sinusoid, a limited phase range of hyperpolarizing inputs elicited rebound spikes, and the phase range of rebound spikes was even narrower. Tuning model parameters of the stellate cell population to match experimental rebound spiking properties resulted in GC spatial periodicity, suggesting resonance and rebound spiking are viable mechanisms for GC generation.

The third experiment tested whether short duration current inputs can induce persistent firing and afterdepolarization in layer V pyramidal cells. During muscarinic acetylcholine receptor activation 1-2 second long current injections have been shown to induce persistent firing in EC principal cells. Persistent firing may underlie working memory performance and has been used to model GCs. However, input stimuli during working memory and navigation may be much shorter than 1-2 seconds. Data showed that input durations of 10, 50 and 100 ms could elicit persistent firing, and revealed time courses and amplitude of afterdepolarization that could contribute to GC firing or maintenance of working memory.

TABLE OF CONTENTS

PRELIMINARY PAGES	i
ACKNOWLEDGMENTS	iv
ABSTRACT	v
TABLE OF CONTENTS	vii
LIST OF TABLES	xii
LIST OF FIGURES	xiii
LIST OF ABBREVIATIONS	xv
CHAPTER 1: Introduction	1
1.1 Spatially modulated cells of the hippocampal system.....	2
1.2 Anatomy	3
1.2.1 Hippocampal-entorhinal circuitry	4
1.2.2 Parahippocampal-entorhinal afferents.....	5
1.2.3 Basal forebrain-entorhinal connectivity	6
1.3 Theta rhythm	6
1.3.1 Generation of theta rhythm.....	6
1.3.2 Theta rhythm and learning and memory	7
1.4 Entorhinal lamina and cell types	8
1.5 Entorhinal intrinsic electrophysiological properties.....	9
1.5.1 Physiology of cells in superficial layers.....	9

1.5.2 Physiology of cells in deep layers	11
1.6 Cholinergic modulation of EC principal cells	11
1.7 Computational models of grid cells.....	13
1.7.1 Oscillatory interference models.....	13
1.7.2 Continuous attractor models.....	14
1.7.3 Model limitations	15
1.8 Motivation for experiments	16
1.8.1 Voltage dependence of resonance frequency in medial EC stellate cells	16
1.8.2 Phase specificity of rebound spiking in medial EC stellate cells	17
1.8.3 Cholinergic induction of ADP and persistent spiking in medial EC deep layer cells.....	17
 CHAPTER 2: Voltage dependence of subthreshold resonance frequency in layer II of medial entorhinal cortex ¹	
2.1 Introduction	19
2.2 Materials and Methods	21
2.2.1 Slice preparation.....	21
2.2.2 Electrophysiological recordings	22
2.2.3 Cell anatomical locations	24
2.2.4 Data analysis.....	26
2.2.5 Biophysical simulation methods	27
2.2.7 Resonance characterization of the model.....	30
2.3 Results	31

2.3.1 Anatomy and morphology of Layer II EC cells	31
2.3.2 Physiology of medial and lateral EC cells.....	31
2.3.3 Resonant frequency varies with anatomical location	32
2.3.4 Resonant frequency varies with voltage.....	33
2.3.5 Biophysical simulations of resonance properties	34
2.3.6 Experimental controls.....	35
2.3.7 Pharmacological blockade of HCN channels	36
2.3.8 Resonance slope along the dorsal-ventral axis of medial EC	36
2.4 Discussion	37
2.4.1 Summary of findings	37
2.4.2 Implications	38
2.5 Tables	43
2.6 Figures	44
CHAPTER 3: Rebound spiking in layer II medial entorhinal cortex stellate cells: possible mechanism of grid cell function ²	58
3.1 Introduction	59
3.2 Materials and methods.....	61
3.2.1 Slice preparation.....	61
3.2.2 Electrophysiological recordings	62
3.2.3 Data analysis.....	65
3.2.4 Biophysical simulation methods	67
3.3 Results	70

3.3.1 Confirmation of stellate cell type	70
3.3.2 Phase specificity of rebound spiking	72
3.3.3 Oscillation frequency and phase analyses	74
3.3.4 Magnitude of hyperpolarizing inputs and phase analyses	75
3.3.5 Pharmacological blockade of HCN channels	76
3.3.6 Single cell simulations of rebound spiking	76
3.3.7 Network simulations of rebound spiking	77
3.4 Discussion	80
3.4.1 Summary of findings	80
3.4.2 Relationship to previous <i>in vitro</i> data	81
3.4.3 Relationship to <i>in vivo</i> recording data	82
3.4.4 Relationship to the resonance frequency of different neurons	83
3.4.5 Significance of magnitudes of hyperpolarization	85
3.4.6 Relationship of model to MSDB-medial EC anatomical connectivity	86
3.4.7 Significance to other grid cell models	88
3.5 Figures	88
CHAPTER 4: Cholinergic modulation of ADP and persistent spiking properties in layer	
V medial entorhinal cortex	100
4.1 Introduction	101
4.2 Materials and Methods	103
4.2.1 Slice preparation	103
4.2.2 Electrophysiological recordings	104

4.2.3 Data analysis.....	106
4.3 Results	108
4.3.1 Cholinergic modulation of sag and resonance properties	108
4.3.2 Input duration affects persistent spiking	109
4.3.3 Input duration affects ADP properties.....	110
4.3.4 Spike number affects ADP properties	111
4.3.5 Voltage affects ADP properties.....	112
4.4 Discussion	113
4.4.1 Summary of findings	113
4.4.2 Implications	115
4.5 Figures	118
CHAPTER 5: Discussion	124
5.1 Implications	125
5.2 Future directions.....	130
BIBLIOGRAPHY	133
CURRICULUM VITAE	154

LIST OF TABLES

Table 1. Model parameters	43
---------------------------------	----

LIST OF FIGURES

Figure 2.1 Anatomy and morphology in layer II cells of medial and lateral EC	45
Figure 2.2 Slice orientation and anatomical location of recording sites in medial and lateral EC	46
Figure 2.3 Physiological properties differ between cells of medial and lateral EC	47
Figure 2.4 Resonant frequency decreases along the D/V axis of medial EC	48
Figure 2.5 The medial EC population shows a clear decrease of the resonant frequency along the D/V axis at membrane potentials near resting potential.....	49
Figure 2.6 Resonant frequency decreases with membrane potential depolarization in medial EC	51
Figure 2.7 Biophysical model of medial EC cells displays relationship between increase in membrane potential and decrease in resonant frequency	53
Figure 2.8 The resonant frequency in medial EC approaches an asymptotic value at membrane potentials below -70 mV, does not display hysteresis, and is not affected by the amplitude of the ZAP stimulus.....	54
Figure 2.9 ZD7288 abolishes resonance properties in medial EC	56
Figure 2.10 Population data showing resonant frequencies at all membrane potentials in dorsal medial EC compared to ventral EC	57
Figure 3.1 Intrinsic electrophysiological properties of stellate cells and loss of these properties with the h current blocker ZD7288	89

Figure 3.2 Stellate cells display rebound spiking in response to a limited range of phases of hyperpolarizing input pulses and with a limited range of output spiking phases .	90
Figure 3.3 Hyperpolarizing and depolarizing input pulses have differential preferred input phases that induce spiking.....	91
Figure 3.4 Preferred inhibitory input and spiking phases correlate with increased relative input frequency.....	93
Figure 3.5 Decreasing magnitude of inhibitory synaptic input correlates with later spiking output phase.....	95
Figure 3.6 I_h is necessary for phase specificity of hyperpolarization induced rebound spiking	96
Figure 3.7 Izhikevich neuron possesses similar intrinsic and rebound spiking properties as stellate cells.....	97
Figure 3.8 A model with stellate cells, possessing resonance and rebound spiking properties, embedded in an inhibitory network creates theta skipping and grid cell firing patterns on a linear track.....	98
Figure 4.1 Cholinergic modulation of sag amplitude and resonance frequency	118
Figure 4.2 Pulse duration affects onset of persistent spiking	120
Figure 4.3 Pulse duration affects ADP amplitude and time constants	121
Figure 4.4 Pulse number affects ADP amplitude and time constants	122
Figure 4.5 Voltage affects ADP amplitude and time constants.....	123

LIST OF ABBREVIATIONS

aCSF	Artificial cerebral spinal fluid
ADP	After-spike depolarization potential
AHP	After-spike hyperpolarization potential
CANN	Continuous attractor neural network model
CA1	Cornu ammonis region 1
CA3	Cornu ammonis region 3
CCh	Carbachol
DG	Dentate gyrus
DMS	Delayed match to sample task
DMNS	Delayed non-match to sample task
D/V	Dorsal-to-ventral
EC	Entorhinal cortex
EPSP	Excitatory postsynaptic potential
fMRI	Functional magnetic resonance imaging
GABA	Gamma-aminobutyric acid
HCN	Hyperpolarization-activated cyclic nucleotide-gated channel
I_{CAN}	Calcium-activated non-specific cation current
I_h	Hyperpolarization-activated current
I_{NaP}	Persistent sodium current
LFP	Local field potential
mAChR	Muscarinic acetylcholine receptor

M/L	Medial-to-lateral
MRA	Mean resultant angle
MRL	Mean resultant length
MSDB.....	Medial septum/diagonal band of Broca
PV	Parvalbumin
R/C.....	Rostral-to-caudal
sMPO.....	Subthreshold membrane potential oscillation
ZAP	Impedance amplitude profile

CHAPTER 1: Introduction

The important role of the medial temporal lobe in memory function was first observed in humans by Scoville and Milner (1957). To alleviate patient HM's severe epilepsy he underwent a surgery bilaterally removing his hippocampi and adjacent cortical structures. The surgery improved HM's seizures but left him with partial retrograde amnesia and full anterograde amnesia, despite leaving his general intelligence and personality intact. This seminal finding has sparked immense research about the hippocampal system in efforts to find answers to the question, "How do we remember?"

1.1 Spatially modulated cells of the hippocampal system

Lesion studies have shown the importance of the hippocampus and medial entorhinal cortex (EC) in spatial memory tasks (Morris et al., 1982; Steffenach et al., 2005; Moser and Moser, 2008). The spatial nature of both the hippocampus and the medial EC is further supported by the presence of place and grid cells found throughout each structure, respectively (O'Keefe and Dostrovsky, 1971; Hafting et al., 2005). It should be noted that grid cells are also present in the pre- and parasubiculum (Boccaro et al., 2010). While place cells fire at one particular location of an environment, grid cell firing fields can be described as appearing on the vertices of tightly packed equilateral triangles, creating a repeating hexagonal array that tessellates the floor of the environment.

Grid and place cells share many properties in common. The size of place and grid cell firing fields, as well as grid cell field spacing, vary as a function of dorsal-to-ventral (D/V) location, such that dorsal cells have smaller fields than ventral cells (Jung et al., 1994; Hafting et al., 2005; Brun et al., 2008; Kjelstrup et al., 2008; Stensola et al., 2012).

Place and grid cells possess a property known as theta phase precession (O'Keefe and Recce, 1993; Hafting et al., 2008). As an animal runs through a firing field, action potentials gradually shift to earlier phases of the local field potential (LFP). Phase precession has been theorized to result from summation of oscillations of different frequencies and has been extended to modeling grid cell properties in the medial EC as discussed in greater detail below (O'Keefe and Recce, 1993; O'Keefe and Burgess, 2005a; Burgess et al., 2007; Hasselmo et al., 2007).

Three additional spatial cells are present throughout parts of the hippocampal system. Head-direction cells fire action potentials when an animal's head is oriented at a preferred angle to the horizontal plane. Head-direction cells are present in layers III, V, and VI of medial EC, dorsal presubiculum (postsubiculum) and the parasubiculum (Ranck, 1984; Taube et al., 1990; Sargolini et al., 2006; Bjercknes et al., 2014; Giocomo et al., 2014). A subset of grid cells located in layers III, V and VI are also conjunctive with the head/running direction of the animal (Sargolini et al., 2006). Finally, boundary cells fire at a fixed distance from environmental boundaries, while border cells fire directly at boundaries such as walls. These cell types are found in the medial EC, presubiculum, parasubiculum, and the subiculum (Solstad et al., 2008; Lever et al., 2009; Boccara et al., 2010).

1.2 Anatomy

The anatomical location of EC is strategically situated to function as the major gate of information flow between the neocortex and hippocampus. The EC is adjacent to a number of cortical regions and the hippocampal formation. The EC is surrounded

rostrally by the piriform (olfactory) cortex and the amygdala, laterally by the perirhinal cortex, medially by the parasubiculum, and caudally by the postrhinal cortex (Canto et al., 2008). The EC can be further subdivided into the medial EC and lateral EC based upon a number of connectivity differences discussed below.

1.2.1 Hippocampal-entorhinal circuitry

The EC is a six-layered structure that can be separated into superficial (I-III) and deep layers (IV-VI). Generally, superficial layers receive cortical afferents and send efferents, via the perforant path, to the hippocampal formation, while deep layers receive hippocampal feedback and send afferents that target the entire cortical mantle. The medial and lateral EC send projections from layer II and layer III to the hippocampus with specific laminar and topographical targets. Layer II medial EC projections terminate in the middle third of the molecular layer of dentate gyrus (DG) and lacunosum-moleculare of cornu ammonis region 3 (CA3), while layer II lateral EC projections terminate in the outer third of these molecular layers (Steward, 1976; Witter et al., 1989; Witter and Amaral, 1991; van Groen et al., 2003; Witter, 2007). Layer III cells of medial EC send projections to proximal CA1 (close to DG) and distal subiculum (far from DG), while layer III lateral EC sends projections to distal CA1 and proximal subiculum (Steward, 1976; Amaral, 1993; Witter, 1993).

The perforant pathway is the first synapse of the ‘tri-synaptic loop.’ The second synapse is formed by DG granule cells, which send mossy fiber projections that terminate on the dendrites of CA3 pyramidal cells (Blackstad et al., 1970; Swanson et al., 1978). The final synapse of the ‘tri-synaptic loop’ is formed by CA3 pyramidal cells whose

axons, termed Schaffer collaterals, target CA1 pyramidal cells (Ishizuka et al., 1990).

The entorhinal-hippocampal loop is closed via projections from CA1 and subiculum that specifically target the deep layers (V-VI) of EC. Moreover these hippocampal inputs to the EC reciprocate the EC layer III perforant path inputs to CA1 and subiculum.

Proximal parts of CA1 and distal parts of subiculum specifically target medial EC, while distal CA1 and proximal subiculum target lateral EC (Witter et al., 1988; Naber et al., 2001). Overall the medial and lateral EC send information to very distinct regions and cell types of the hippocampus. Feedback from the hippocampus reciprocates this specificity creating two streams of information.

1.2.2 Parahippocampal-entorhinal afferents

The medial and lateral EC receive inputs from the postrhinal and perirhinal cortex, respectively (Burwell and Amaral, 1998a). The postrhinal cortex receives the majority of its inputs from visual, posterior parietal, and retrosplenial cortices, while the perirhinal cortex receives inputs from the temporal, piriform, frontal, and insular cortices (Burwell and Amaral, 1998b; Kerr et al., 2007). EC pre- and parasubicular afferents show specific targeting for medial and lateral EC. The presubiculum selectively targets layers I and II of medial EC, and parasubiculum targets layer II of both medial and lateral EC (Caballero-Bleda and Witter, 1993). While the majority of inputs to the presubiculum originate from primary and secondary visual cortices, the parasubiculum only receives little cortical input from the retrosplenial and visual association areas (Vogt and Miller, 1983). The variety of spatially modulated cells reported in the medial EC is reflective of its dominant visuo-spatial inputs from perirhinal cortex and presubiculum.

In contrast, cells of the lateral EC lack spatial selectivity and grid cells have not been found in lateral EC (Hargreaves et al., 2005; Yoganarasimha et al., 2010).

1.2.3 Basal forebrain-entorhinal connectivity

The rodent EC receives subregion specific inputs from the basal forebrain. Both medial and lateral EC receive inputs from the diagonal band of Broca. However, the medial septal nucleus selectively targets the medial EC, and the nucleus basalis of Meynart selectively targets lateral EC (Beckstead, 1978; Burwell and Witter, 2002). The EC is reciprocally connected with the medial septum/diagonal band of Broca (MSDB). MSDB inputs to the medial and lateral EC terminate in layers II and V, whereas EC projections to the MSDB originate in layer V of medial EC and layers II-V of lateral EC (Alonso and Köhler, 1984).

1.3 Theta rhythm

1.3.1 Generation of theta rhythm

Large amplitude oscillations at theta frequency (first termed regular slow activity, 6-10 Hz) dominate the LFP in the hippocampus (Vanderwolf, 1969; Buzsáki et al., 1983) and the EC (Mitchell and Ranck, 1980). The MSDB contains cells expressing glutamate, gamma-aminobutyric acid (GABA), and acetylcholine that project to the hippocampus and EC (Kiss et al., 1990; Stewart and Fox, 1990; Manns et al., 2001; Buzsáki, 2002; Hajszan et al., 2004; Colom et al., 2005). Data suggest that GABAergic cells of the MSDB are largely responsible for pacing theta. Some cells of the MSDB and hippocampus have been termed ‘theta’ cells due to their rhythmic bursting behavior

(Petsche et al., 1962; Ranck, 1973). Based on their spike waveforms the majority of these ‘theta’ cells have been identified as putative GABAergic cells (King et al., 1998). Recently Varga and colleagues (2008) have shown theta rhythmicity in MSDB GABAergic cells is due to the expression of hyperpolarization-activated cyclic nucleotide-gated (HCN) channels. A subset of GABAergic cells expressing parvalbumin (PV) selectively innervate other GABAergic cells of the hippocampus, while cholinergic terminals arising from medial septum are found on hippocampal principal cells and GABAergic cells (Freund and Antal, 1988). Moreover, inhibitory connections are reciprocal, as PV cells of the hippocampus selectively innervate GABAergic cells of the MSDB (Toth et al., 1993). GABAergic cell reciprocity may be a general principle between the MSDB and other theta rhythmic brain regions, as MSDB GABAergic inputs selectively target GABAergic interneurons of the medial EC (Gonzalez-Sulser et al., 2014).

1.3.2 Theta rhythm and learning and memory

The theta rhythm is physiologically and behaviorally important. Various cells of the hippocampus (Klausberger et al., 2003) and EC (Alonso and Garcia-Austt, 1987) fire at preferred phases of hippocampal theta. Pyramidal cells of the hippocampus have membrane potential oscillations that are phase locked to theta (Fujita and Sato, 1964; Kamondi et al., 1998). The theta rhythm has been proposed as a mechanism by which cells can carry out computations to support memory function (Hasselmo et al., 2002). Behavioral data support this notion, as theta power and spike-field coherence is correlated with memory performance in humans (Poch et al., 2011; Rutishauser et al.,

2010; Tesche and Karhu, 2000). Electrolytic lesions of the MSDB completely abolish theta activity in the hippocampus and impair spatial learning (Winson, 1978; Bland, 1986) and bilateral lesions to the EC in conjunction with administration of atropine or physostigmine completely abolish theta activity in the rat hippocampus (Buzsáki et al., 1983). Pharmacological inactivation of the medial septum with muscimol or lidocaine abolishes the theta rhythm and the spatial modulation of grid cells in medial EC (Brandon et al., 2011; Koenig et al., 2011). These data demonstrate the importance of theta and the brain regions generating theta for learning and memory functions.

1.4 Entorhinal lamina and cell types

The laminar organization of the EC used here was first described by Ramon y Cajal (1901a-1902) in his classic Golgi stain studies. Layer I of EC generally lacks cell bodies and consists of a dense plexus of axonal fibers. Layer II is easily identifiable as it is densely packed with large spiny stellate cells and pyramidal cells. Both Layer II stellate and pyramidal cells have large cell bodies with basal dendrites extending throughout layers II and III. However, only stellate cells contain multiple thick primary dendrites radiating in all directions into layer I, while pyramidal cells have a single apical dendrite extending into layer I (Klink and Alonso, 1997). In contrast to layer II, layer III is wider and contains loosely packed pyramidal-like cells with morphologies very similar to layer II pyramids except their basal dendrites are largely confined to layer II (Gloveli et al., 1997). Layer IV, or the lamina denticata, is a cell sparse layer that demarcates the transition between the superficial and deep layers of EC. Adjacent to lamina denticata is layer V, a relatively thin layer, containing cell bodies of medium to large principal cells.

Morphological cell types in this layer include pyramidal cells, polymorphic cells and horizontal cells (Hamam et al., 2000, 2002). Pyramidal and horizontal cells have an apical dendrite that extends to superficial layers (I-II) and basal dendrites in layers V-VI. Horizontal cells can be differentiated from pyramidal cells by the more expansive horizontal spread of their basal dendrites. Polymorphic cells have dendrites radiating in all directions from the cell body. Layer VI consists of loosely arranged cells varying in size and shape. Adjacent to layer VI is the angular bundle, the axon fiber tract connecting the EC and the hippocampal formation.

1.5 Entorhinal intrinsic electrophysiological properties

1.5.1 Physiology of cells in superficial layers

Electrophysiological data of the EC has greatly focused on layer II medial EC stellate cells. The hallmark electrophysiological property of stellate cells is a prominent inward rectification or sag potential in response to a hyperpolarizing step current (Alonso and Llinas, 1989; Alonso and Klink, 1993). Upon release from hyperpolarization, stellate cells respond with post inhibitory rebound spikes. Additionally, stellate cells display subthreshold membrane potential oscillations (sMPOs) in the theta frequency band that increase in amplitude and rhythmicity with membrane depolarization (Alonso and Llinas, 1989; Alonso and Klink, 1993). While the sag potential is solely mediated by activation of a hyperpolarization-activated cation current (h current or I_h), sMPOs are mediated by the interplay of a persistent sodium current (I_{NaP}) with I_h , which operate in a push-pull fashion to depolarize and hyperpolarize membrane potential (Klink and Alonso, 1993; Magistretti and Alonso, 1999; Dickson et al., 2000; Fransén et al., 2004). Additionally,

stellate cells possess resonance in the theta frequency band (Haas and White, 2002; Erchova et al., 2004; Giocomo et al., 2007, Boehlen et al., 2010; Heys et al., 2010; Shay et al., 2012).

Resonance can be described as the ability to selectively respond to a preferred input frequency. Typically an impedance amplitude profile (ZAP), a sinusoidal input with linearly increasing frequencies, is used to test the resonant properties of cells. Resonance occurs by the interplay of passive properties of a cell, i.e. the leak conductance (resistance) and membrane capacitance, with voltage-gated currents that actively oppose changes in membrane voltage, such as I_h (Puil et al., 1986; Hutcheon and Yarom, 2000; Erchova et al., 2004; Heys et al., 2010). This combination of passive (low pass filter) and active (high pass filter) properties creates a notch filter, whose frequency preference is dependent on the difference between a cell's membrane time constant and the activation time constant of the active current.

A number of intrinsic properties of layer II stellate cells show gradients as a function of anatomical location. The frequency of sMPOs and resonance, as well as the I_h time constant, vary along the D/V axis of medial EC (Giocomo et al., 2007; Giocomo and Hasselmo, 2008a, 2008b; Boehlen et al., 2010; Dodson et al., 2011). Stellate cell medium after-spike hyperpolarization potential (AHP) and after-spike-depolarization (ADP) time constants decrease along the D/V axis (Navratilova et al., 2012). The time window for synaptic integration and summation of gamma stimulated excitatory post synaptic potentials (EPSPs) increases along the D/V axis (Garden et al., 2008). The

strength of adaptation also changes along the D/V axis (Yoshida et al., 2013). These gradients correlate with the gradients of grid cell field size and spacing observed *in vivo*.

In contrast to layer II stellate cells, layer II medial EC pyramidal cells have a much smaller sag potential, lack theta rhythmic sMPOs, and do not respond to hyperpolarization with rebound spikes (Alonso and Klink, 1993). Lateral EC layer II fan cells (the morphological correlate to stellate cells) and pyramidal cells lack a sag potential altogether, and although fan cells display sMPOs, they are less rhythmic compared to stellate cells (Tahvildari and Alonso, 2005).

1.5.2 Physiology of cells in deep layers

Medial EC layer III pyramidal cells can be differentiated from layer II pyramidal cells by a complete lack of sag potential and sMPOs (Dickson et al., 1997; Gloveli et al., 1997; Van der Linden and Lopes da Silva, 1998). Although there is some variety among layer V EC principal cells, they generally contain a small sag potential compared to stellate cells and display prominent (2-7 mV) sMPOs in the theta range (5-15 Hz) when held close to spiking threshold. Unlike stellate cells however, I_h does not seem to mediate the sMPOs displayed by layer V cells (Schmitz et al., 1998; Dickson et al., 2000a; Hamam et al., 2000, 2002). Layer V pyramidal cells show unique modulatory properties as discussed below.

1.6 Cholinergic modulation of EC principal cells

Activation of muscarinic acetylcholine receptors (mAChRs) results in a number of modulatory responses in cells of the medial EC. In Layer II stellate cells, application of carbachol (CCh) decreases the frequency of subthreshold oscillations, sag amplitude,

and resonance frequency (Klink and Alonso, 1997b; Heys et al., 2010). Voltage-clamp experiments have shown that the modulation of stellate cell resonance is likely mediated through a decrease in the amplitude of the I_h and a concomitant leftward shift of the I_h activation curve (Heys and Hasselmo, 2012). These findings have intriguing implications in regards to grid cells. Decreases in resonance frequency through modulation of the I_h correlates well with the expansion of grid cell firing fields found in HCN1 knock-out mice as well as with the expansion of grid cell firing fields in novel environments, a condition in which acetylcholine levels are increased (Acquas et al., 1996; Giocomo et al., 2011; Barry et al., 2008; 2012).

Across many brain regions the hallmark neuronal response to mAChR activation is depolarization, increased input resistance, and enhanced excitability through blockade of the slow AHP. These effects are in part mediated via inhibition of calcium-activated potassium channels (Krnjevic et al., 1971; Bernarndo and Prince, 1982; Cole and Nicoll, 1984; McCormick and Prince, 1985, 1986; Klink and Alonso 1997a,c). Additionally, mAChR activation turns on a calcium-activated non-specific cation current (I_{CAN}). This current contributes to depolarization and upon action potential generation results in a slow ADP (Cole and Nicoll, 1984b; Andrade, 1991; Constanti and Bagetta, 1991; Caesar et al., 1993; Haj-Dahmane and Andrade, 1996, 1998; Klink and Alonso, 1997c; Shalinsky et al., 2002). The ADP leads to subsequent spiking that can last for up to minutes without further stimulation. This phenomenon is known as persistent firing. Muscarinic-dependent persistent firing is found in brain regions throughout the parahippocampal region, including the medial and lateral EC, CA1 and DG of the

hippocampus, postsubiculum, perirhinal cortex, as well as the prefrontal cortex (Dickson and Alonso, 1997; Klink and Alonso, 1997b,c; Haj-Dahmane and Andrade, 1998; Dickson et al., 2000a; Egorov et al., 2002; Tahvildari et al., 2007, 2008; Yoshida and Hasselmo, 2009; Navaroli et al., 2012; Jochems et al., 2013; Knauer et al., 2013; Anderson and Strowbridge, 2014). Layer V medial EC pyramidal cells possess the unique modulatory property of graded persistent firing, where depolarizing or hyperpolarizing current inputs incrementally increase or decrease the frequency of persistent spiking, respectively (Egorov et al., 2002). The mechanism of graded persistent firing has been proposed to include activation of I_{CAN} as discussed above (Fransén et al., 2006). The model proposes that a calcium-regulated metabolic cascade, such as de/phosphorylation, affects the conductance of the I_{CAN} and can thereby bi-directionally control the frequency of persistent spiking. This is a realistic mechanism as I_{CAN} can be up-and-down-regulated by intracellular calcium concentration in layer II medial EC neurons (Magistretti et al., 2004).

1.7 Computational models of grid cells

1.7.1 Oscillatory interference models

Computational models describing the spatial firing patterns of grid cells within medial EC fall into two major categories. In the first category are oscillatory interference models that utilize phasic interference patterns between different oscillations, for example this could involve a fixed somatic oscillation and dendritic oscillations with changing frequency. In the model, dendritic oscillation frequencies are controlled by running direction with preferred angles in multiples of 60° and are linearly dependent on

the animal's running velocity (Burgess et al., 2007; Hasselmo et al., 2007; O'Keefe and Burgess, 2005). Therefore, as the animal runs in a preferred direction, the frequency of that particular oscillation increases (or it could decrease), causing it to go in and out of phase with the fixed somatic oscillation, and thus creates constructive and destructive interference patterns. These interference patterns appear as bands of activity oriented along preferred directions. When interference patterns from multiple (usually three) preferred directions are summed or multiplied a grid-like pattern of firing fields emerges. The spatial periodicity of a grid cell is determined by the beat frequency or the difference between the dendritic and somatic oscillations. Oscillatory interference models have successfully predicted the D/V gradient of sMPOs (Giocomo et al., 2007), theta phase precession in grid cells (Hafting et al., 2008), the change of spike frequency with running speed (Jeewajee et al., 2008), and the link between I_h and grid cell spacing (Giocomo et al., 2011).

1.7.2 Continuous attractor models

Continuous attractor neural network (CANN) models use specific patterns of excitatory and inhibitory connections to generate one or more activity bumps and move the activity bumps around a sheet or torus of neurons (Burak and Fiete, 2009; Fuhs and Touretzky, 2006; Guanella et al., 2007; McNaughton et al., 2006). Like the oscillatory interference models, CANN models also depend on a direction signal modulated by running speed. This velocity-modulated input controls the movement of the activity bump creating the grid pattern. The gradient of spatial periodicity along the D/V axis is modeled as a decrease in the gain of the velocity signal. The influence of shared synaptic

connections on attractor properties in the population mean that CANN models successfully predicted multiple networks or modules within medial EC. Support for modular processing within medial EC is provided by Burgalossi et al. (2011) who showed patches of cytochrome oxidase catalytic activity along the D/V axis. The incremental increase in grid cell field size and spacing along the D/V axis of medial EC provides additional support for medial EC modules (Barry et al., 2007; Stensola et al., 2012).

1.7.3 Model limitations

Both oscillatory interference and CANN models are imperfect and have their constraints. For instance, oscillations are very sensitive to noise creating variance in the period, which leads to an inconsistent phasic relationship between dendritic and somatic oscillations over time (Zilli et al., 2009). Also, dendritic oscillations tend to couple with somatic oscillations, making the stability of independent oscillators transient (Remme et al., 2009, 2010). sMPOs do not show a linear increase in frequency with depolarization as required by oscillatory interference models (Yoshida et al., 2011). These problems have led to second generation interference models, that replace single dendritic oscillations with populations of persistent spiking neurons or noisy coupled oscillators (Hasselmo, 2008; Zilli and Hasselmo, 2010).

CANN models require specific connectivity patterns (i.e. a twisted torus or ‘Mexican hat’ inhibitory connectivity between neurons coding nearby spatial locations) and whether or not the entorhinal network is wired in this way is still unclear. However, in support of CANN models, functional connectivity experiments have shown medial EC

stellate cells are embedded in a dense feedback inhibitory network with very little recurrent excitatory connections (Dhillon and Jones, 2000; Couey et al., 2013, Pastoll et al., 2013). The strengths and weaknesses of both classes of models have recently led to ‘hybrid’ models containing aspects of both oscillatory interference and CANN models (Blair et al., 2007, 2008; Navratilova et al., 2012; Mhatre et al., 2012; Hasselmo, 2013; Hasselmo and Shay, 2014).

1.8 Motivation for experiments

1.8.1 Voltage dependence of resonance frequency in medial EC stellate cells

Previous studies have shown that the resonance frequency of layer II stellate cells varies with voltage but only sampled across a narrow range of membrane potentials (Nolan et al., 2007; Boehlan et al., 2010; Heys et al., 2010; cf. Erchova et al., 2004). Oscillatory interference models require a linear relationship between running speed and frequency of oscillations (Burgess et al., 2007; Hasselmo et al., 2007; Giacomo and Hasselmo, 2008a). As discussed above sMPOs do not fulfill this requirement. Therefore, a major objective of this study was to see if resonance could suffice as an alternative mechanism of grid cell spatial periodicity in oscillatory interference models. Additionally, prior to this thesis work the resonance properties of layer II lateral EC fan cells have not been studied. The second objective was to study resonance within these cells of lateral EC.

1.8.2 Phase specificity of rebound spiking in medial EC stellate cells

The data shown in chapter 2 suggest that resonance could be a viable mechanism for grid cell function. Building off of this idea, recent ‘hybrid’ models from our laboratory have combined resonance and rebound spiking properties of layer II stellate cells with network connectivity to simulate grid cell spatial periodicity (Hasselmo, 2013, Hasselmo and Shay, 2014). Predictions of this model have motivated the study presented in chapter 3. The main objective of this study was to analyze phase specificity of hyperpolarizing inputs eliciting rebound spikes as well as rebound spiking phase specificity in reference to theta frequency sinusoidal inputs injected into the soma of layer II medial EC stellate cells.

1.8.3 Cholinergic induction of ADP and persistent spiking in medial EC deep layer cells

Experimental and modeling data suggest persistent activity is a likely mechanism of working memory (Fuster and Jervey, 1982; Funahashi et al., 1989; Lisman and Idiart, 1995; Fransén et al., 2002; Schon et al., 2004, 2005). Persistent spiking has also been used to simulate grid cell spatial periodicity (Hasselmo, 2008; Hasselmo and Brandon, 2008). While the relatively long inputs (1-2 seconds) used to elicit spiking may be appropriate for active maintenance of information during delay periods, it may not be appropriate for a navigating animal. One objective of the study in chapter 4 was to see if shorter inputs (10-100 ms) are able to elicit persistent spiking. Information about the ADP is relatively limited in the EC and so a second objective of the study in chapter 4 was to investigate properties of the ADP, such as the effect of membrane potential, input duration, and spike number on the ADP amplitude and time course.

**CHAPTER 2: Voltage dependence of subthreshold resonance frequency in layer II
of medial entorhinal cortex¹**

¹This work has previously been published as Shay CF, Boardman IS, James NM, Hasselmo ME (2012) Voltage dependence of subthreshold resonance frequency in layer II of medial entorhinal cortex. *Hippocampus* 22:1733-49. Reprinted here with permission.

2.1 Introduction

The entorhinal cortex (EC) plays an important role in spatial memory function, as shown by impairments of spatial memory with lesions of this structure (Steffenach et al., 2005; Moser and Moser, 2008). Spatial coding by medial EC has been shown in unit recordings of layer II medial EC ‘grid cells’, which fire when a rat is in a repeating array of spatial locations falling on a hexagonal grid (Fyhn et al., 2004; Moser and Moser, 2008; Hafting et al., 2005). Computational models of the mechanism of generation of entorhinal grid cells (Burgess et al., 2007) have proposed a role for intrinsic properties of entorhinal neurons that were initially discovered in slice preparations. Layer II of medial EC contains stellate cells that display sMPOs (Alonso and Llinas, 1989; Klink and Alonso, 1993) and membrane potential resonance (Haas and White, 2002; Erchova et al., 2004; Giocomo et al., 2007).

Differences in the resonance properties of individual entorhinal neurons may underlie differences in the spacing and size of grid cell firing fields that have been found to increase along the dorsal to ventral (D/V) axis of the medial EC (Hafting et al., 2005; Sargolini et al., 2006). *In vitro* slice studies (Giocomo et al., 2007; Giocomo and Hasselmo, 2008a; Giocomo and Hasselmo, 2008b; Boehlen et al., 2010; Dodson et al., 2011) have found similar gradients in sMPO frequencies and resonant frequencies along the D/V axis of the medial EC.

An initial model of grid cells developed by Burgess and colleagues used oscillatory interference between oscillations with differences in frequency (Burgess et al., 2005; Blair et al., 2007; Burgess et al., 2007; Hasselmo et al., 2007; Blair et al., 2008;

Burgess, 2008). In some versions of these models, the changes in frequency were proposed to arise from changes in membrane potential driven by cells responding to head direction and running speed (Burgess et al., 2007; Hasselmo et al., 2007), suggesting an important role of changes in intrinsic frequency with membrane potential. A number of subsequent studies have argued against an interaction of sMPOs within single cells based on the variance of sMPOs (Giocomo and Hasselmo, 2008a; Welinder et al., 2008; Zilli et al., 2009) the synchronization properties of sMPOs (Remme et al., 2009) and the lack of linear changes in sMPO frequency with membrane potential (Yoshida et al., 2011). However, models have not yet demonstrated why the intrinsic resonance of neurons appears to correlate with the spacing and size of grid cell firing fields.

As an alternative to sMPOs, differences in resonance frequency at different membrane potentials may contribute to generation of grid cells. The membrane potential dependence of resonance in entorhinal cortex is unclear. An initial study did not find resonance to depend on membrane potential (Erchova et al., 2004), but subsequent studies have shown membrane potential dependence (Nolan et al., 2007; Boehlen et al., 2010; Heys et al., 2010). These studies only plotted three different membrane potentials, leaving the shape of the change in resonance frequency with membrane potential unspecified. In particular, it is not clear if the change in resonance frequency with membrane potential is linear. Oscillatory interference models require that the difference in frequency between pairs of oscillators must vary linearly with velocity. This requirement of the model could be satisfied by a linear change in resonant frequency with membrane potential.

In contrast to medial entorhinal cortex, grid cells have not been shown in lateral EC and recordings of spiking activity in cells of lateral EC shows significantly less spatial selectivity than in medial EC (Hargreaves et al., 2005; Yoganarasimha et al., 2010). Interestingly, this difference in the presence of grid cells appears consistent with the fact that previous studies showed that cells of the lateral EC lack subthreshold membrane potential oscillations (Tahvildari and Alonso, 2005). However, a systematic approach to measuring the resonance properties of neurons to different input frequencies in lateral EC has not previously been published.

To address these issues, we measured the membrane potential dependence of the resonant frequency in layer II of medial EC and lateral EC. We found that the resonant frequency of individual cells in layer II of the medial EC showed a linear decrease in frequency as the membrane potential was depolarized. These results are important for the hypothesis that the regulation of resonant frequency by synaptic inputs influencing membrane potential could contribute to the generation of grid cells. Furthermore, they support the role of I_h in resonant properties that could underlie processing of spatial information in the medial EC. These results were presented previously as an abstract (Shay et al., 2010).

2.2 Materials and Methods

2.2.1 Slice preparation

We measured the effect of membrane potential on the resonant frequency of neurons at different positions along the D/V axis of layer II in the medial entorhinal

cortex and the medial-to-lateral (M/L) axis of lateral entorhinal cortex. All experimental protocols were approved by the Institutional Care and Use Committee at Boston University. Long-Evans rats (postnatal days 17 to 21, Charles River, Wilmington, MA) were deeply anesthetized with isoflurane (Abbot Laboratories). After the absence of both pedal and tail pinch reflexes, brains were rapidly removed and placed in ice-cold artificial cerebral spinal fluid (aCSF) containing (in mM) 125 NaCl, 2.0 CaCl₂, 2.5 KCl, 1.25 NaH₂PO₄, 25 NaHCO₃, 25 D-Glucose, and 1.0 MgCl₂ (pH adjusted to 7.4 with 95% O₂ - 5% CO₂). Horizontal (medial and lateral EC recordings) or coronal (lateral EC recordings) brain slices, 400 μm-thick, were made using a vibroslicer (Leica VT 1000). Immediately after slicing, slices were transferred to a holding chamber filled with aCSF and incubated for 30 minutes at 33°C. Following this incubation, slices were left at room temperature for another 30 minutes before recordings began.

2.2.2 Electrophysiological recordings

Slices were placed in a recording chamber superfused with aCSF containing 2 mM kynurenic acid and 100 μM of picrotoxin to block glutamatergic and GABAergic synaptic transmission, respectively. The temperature was maintained between 34°C and 36°C. Whole cell pipettes were fabricated from borosilicate glass capillaries by means of a P-87 horizontal puller (Sutter Instruments). Pipettes were filled with internal solution containing (in mM) 120 K-gluconate, 10 HEPES, 0.2 EGTA, 20 KCl, 2.0 MgCl₂, 4.0 Na₂ATP, 0.3 Na₃GTP, and 7 phosphocreatine-diTris (pH adjusted to 7.3 with KOH). 0.1% biocytin was included in the internal solution for the purpose of labeling. When filled with internal solution, pipettes had resistances from 3 to 5 MΩ. Cells were

visualized under an upright microscope (Zeiss Axioskop 2 or Olympus BX51I) equipped with a 40x immersion lens and a near infrared charge-coupled device (CCD) camera (JAI CV-M50IR). Tight seals ($>1\text{ G}\Omega$) were obtained and whole cell access was gained by brief negative pressure. Current-clamp recordings were made with the Multi Clamp 700B amplifier (Axon Instruments) using the built-in capacitance compensation and bridge balance circuitry. Signals were sampled at either 10 or 20 kHz using Clampex 9.0 (Axon Instruments).

After obtaining whole cell configuration, cells were left to stabilize for 2 to 5 minutes before recordings began. Only cells with resting membrane potentials below -55 mV were used for this study. Additionally, all cells displayed overshooting action potentials for the entire recording session. We aimed to use only stellate cells in layer II medial EC. Therefore we did not include cells displaying fast spiking, which is often indicative of interneurons. We also excluded pyramidal cells by measuring the sag potential in each cell. Stellate cells displayed a strong sag potential, whereas pyramidal cells did not. The sag potential was measured by delivering nine successive 0.5 s , 50 pA hyperpolarizing current steps with cells held at -65 mV . All cells of lateral EC, recorded from both horizontal and coronal sections, lacked a strong sag potential, making it more difficult to distinguish between cell types. However, the physiology of layer II lateral EC cells was similar (especially in coronal sections), but the morphology of every cell is not known. Therefore, it is possible that all morphological cell types are included in the lateral EC dataset. However, the fills that we did obtain showed that cells in lateral EC were fan cells according to Tahvildari and Alonso (2005).

To assess the resonant properties of medial and lateral EC cells, the chirp function in MATLAB (Natick, MA Version 7.9, 2009) was used to create an impedance amplitude profile (ZAP) stimulus (Erchova et al., 2004). The ZAP consisted of a 20-second sinusoid with linearly increasing frequency (0 to 20 Hz). The peak-to-peak amplitude of the ZAP stimulus ranged from 40 to 120 pA and was adjusted so as to maintain subthreshold membrane potential dynamics across the range of membrane potentials (-55 to -70 mV: medial EC, n=65 and lateral EC horizontal, n=21; -55 to -80 mV: medial EC, n=17; and -60 to -90 mV: medial EC, n=7 and lateral EC coronal, n=43) where resonant frequencies were measured. Therefore, the smaller 40 pA ZAP stimulus was used at depolarized values (-55 to -60 mV), while the larger amplitude stimuli were used at more hyperpolarized potentials. This procedure accomplished two things. First, it ensured that spiking was not elicited and second, it allowed for sufficiently large voltage responses to clearly measure the resonant frequency at all membrane potentials. Additional experiments showed that there were no significant differences in resonant frequency measured with a full range of different ZAP amplitudes.

2.2.3 Cell anatomical locations

The relative anatomical (D/V or rostral-to-caudal, R/C) location of each cell was determined by keeping track of the depth of each slice. Brains were sliced from either the dorsal or ventral surface (horizontal slices) or from the caudal surface (coronal slices). At the start of slicing, an initial slice with the vibratome was made that was between 2 and 3 mm from the surface of the brain. The relative distance of each slice was then calculated by keeping track of the number of slices taken (400 μm each) and adding that

to the depth of the initial cut. Each slice was placed in a labeled holding chamber, designed to keep slices separate from one another. In horizontal sections, medial EC recordings were made between 2.8 and 7.8 mm from the dorsal surface, while recordings in lateral EC were taken between 4.5 and 7.8 mm. In coronal sections, recordings were made in lateral EC between 2.2 and 4.6 mm from the caudal surface of the brain. In order to measure the distance from each cell and either the caudo-medial tip (horizontal sections) or the rhinal sulcus (coronal sections), we used the coordinates of the micromanipulator of both locations. All distances reported were calculated by finding the length of the hypotenuse between the cell and appropriate anatomical landmark. In horizontal slices we recorded from cells ranging from 0.5 to 2.6 mm from the most caudo-medial aspect of the slice. We tended to stay closer to the caudo-medial tip of the slice in ventral slices as a substantial portion of lateral EC is included at these depths. In more dorsal slices we recorded from cells up to 2.5 mm because lateral EC is limited at these D/V locations. In coronal slices all cells were located ventral to the rhinal sulcus and ranged from 0.386 to 1.925 mm from the center of the rhinal sulcus. Initially, biocytin staining was done to ensure cell type and anatomical location within the slice. This staining method has been described previously (Giocomo and Hasselmo, 2009). About 16% of all cells (11/65 medial EC, 4/21 lateral EC-horizontal, and 10/43 lateral EC-coronal) were processed for biocytin fills.

We also mapped recording sites along the D/V axis of medial EC and the M/L axis of lateral EC. To do this, brains were sliced at 200 μm , fixed in 4% formaldehyde for 2 hours, washed in 0.1 M phosphate buffer solution, and Nissl stained. Using the

measurements above, we measured the hypotenuse length of right triangles from appropriate landmarks of representative horizontal and coronal slices along the D/V and rostral-caudal (R/C) axis, respectively. Measuring the R/C position of a slice as well as the D/V (i.e. the distance from the center of the rhinal sulcus) position of a cell within a slice provides an accurate measure of a cell's position along the M/L axis of lateral EC. Therefore, throughout this paper, the use of D/V in reference to lateral EC is meant as a measurement within a single slice representing the distance of a cell from the center of the rhinal sulcus.

2.2.4 Data analysis

The sag potential amplitude was calculated using MATLAB by subtracting the steady-state potential from the most negative voltage of the sag amplitude. This was done with a 95% confidence interval for all hyperpolarizing current steps in medial and lateral EC cells.

Resonant frequencies were calculated following the techniques from Erchova (Erchova et al., 2004) using a RLC model and MATLAB curve fitting routines. A characteristic resonant response of the cell to the ZAP input waveform was observed as a peak in the excursions of the membrane potential waveform (maximum range of the envelope), which occurs at the time in the data when the instantaneous frequency of the ZAP signal was near the cell's resonant frequency. Taking the impedance ($Z(f)$) of the cell as the ratio of the magnitude of the Fourier transform of the output (membrane potential) to the magnitude of the Fourier transform of the input (ZAP plus dc injection),

there was usually a peak in the impedance curve somewhere in the ZAP frequency range (0 to 20 Hz) at different levels of mean membrane potential.

The impedance response can be accurately modeled with a passive circuit model (RLC) as described by Erchova et al. (2004). Applying their model in the MATLAB `lsqcurvefit` routine, we obtained the resonance frequency (F_r) as that frequency in the range 0.5 to 16 Hz at which the RLC model fit is maximal. The quality ratio (Q) is taken as the ratio of the corresponding maximum impedance to the RLC model value at zero frequency.

2.2.5 Biophysical simulation methods

We tested whether the relationship of resonance frequency to mean membrane potential observed in the *in vitro* data from medial entorhinal cortex stellate cells could derive from the voltage dependence of the kinetics of the ion channels theorized to support the resonance. We performed biophysical simulations in MATLAB (version 7.9, 2009) to analyze channel behavior under the stimulus protocol and to analyze how biophysical properties affect the dependence of resonance frequency on membrane potential. A single compartmental model of a stellate cell was constructed. Similar to previous models (Fransén et al., 2004; Heys et al., 2010), the system contains currents previously proposed to underlie sMPOs these being the hyperpolarization-activated cation current, I_h , and persistent sodium current, I_{NaP} . These mechanisms have also been analyzed in other models (White et al., 1995; Dickson et al., 2000). For fast spiking simulations we included Hodgkin-Huxley currents I_{Na} (fast sodium channel) and I_K (delayed rectifier) with parameters from a model of a CA3 pyramidal neuron (Traub et

al., 1991). All currents were modeled using the Hodgkin-Huxley formalism in an equivalent circuit representation of membrane potential dynamics as follows:

$$C_m \frac{dV_m}{dt} = \sum_i g_i(V_m)(V_m - E_i) + I_{noise} + I_{app} + I_L \quad (\text{eq. 2.1})$$

In this first-order dynamical system, V_m is the membrane potential variable and C_m is the membrane capacitance constant (1 mF/cm²). The term in the right-hand side summation includes the currents listed above, each with reversal potentials E_i and with voltage-dependent conductance gating variables g_i incorporating the corresponding channel kinetics. Also included in the summation is leakage current I_L which has constant conductance. Noise current I_{noise} is introduced using a voltage-independent, normally distributed, conductance noise. The remaining term I_{app} represents the injected current for testing resonance at different membrane potentials. In our simulations, the injected current is the sum of the impedance amplitude profile (ZAP) described above for testing the resonance peak and a baseline direct current level, which has a negative sign to hyperpolarize and a positive sign to depolarize the cell for testing the resonance at different mean membrane potentials.

In general, the voltage-dependent gating variables g_i are proportional to the product of the corresponding channel activation and inactivation probabilities,

$g_i(V) = G_i m_i(V) h_i(V)$ (eq. 2.2) where G_i is the maximum conductance density for the channel; and, m_i and h_i are the probability of channel activation or inactivation,

respectively, each following (by integration) a variable long term value at a variable rate,

$\frac{dp}{dt} = \tau_p^{-1}(p_\infty - p)$ (eq. 2.3) where p_∞ is the voltage-dependent long term (steady-state)

value of activation or inactivation, and τ_p is the corresponding, voltage-dependent, integration time constant. In our system, only fast sodium current I_{Na} was modeled with continuous functions for both activation and inactivation probabilities. In addition, the fast sodium activation probability was moderated in its contribution to I_{Na} by squaring (Traub et al. 1991).

The kinetics of the persistent sodium current were modeled according to Fransén et al. (2004) for activation, and according to (Magistretti and Alonso, 1999) for inactivation. The fast time scale of activation permitted simplification by setting the activation directly to its steady-state value for the current membrane potential at each time step. The I_h is modeled with fast and slow activation time constants (Fransén et al., 2004). The MATLAB curve fitting tool was used to fit the time constant and the steady state activation functions to experimental voltage clamp data for both dorsal and ventral stellate cells (Giocomo and Hasselmo, 2008a).

The differential equations in the above system were integrated using a MATLAB ODE solver (*ode15s* was selected for beneficial speed/accuracy trade-off compared with *ode45* or the Crank-Nicolson method). The time step used for analysis of the solutions was 0.1 msec. For all simulations, the results presented were preceded by a 3 second equilibration interval following which, given continued fixed current input, the mean membrane potential would change less than $\sim 5\%$ per second.

2.2.6 Conductance gating models

The voltage dependence of the gating parameters for each active conductance were modeled as listed below in Table 1. Voltages are in millivolts, time in milliseconds,

and constant values calculated for 37 °C. The maximum conductance values G_i (mS/cm²) for different currents had the following values: Fast h current: 0.13; Slow h current: 0.079; NaP: 0.065; leakage current: 0.07; Fast spiking: Na: 3.8, K: 10.7. The reversal potentials E_i (mV) for different currents had the following values: hyperpolarization activated non-specific cation channel (I_h): -20; persistent sodium and fast sodium channels (I_{NaP} , I_{Na}): 87; delayed rectifier channel (I_K): -83; Leakage channel (I_L): -90, V_m at rest = -60 mV. These values were chosen to give physiologically relevant membrane resistance, sag response, resonance frequency, resonance strength, sMPO frequency and sMPO amplitude.

2.2.7 Resonance characterization of the model

A characteristic resonant response of the model to the ZAP input waveform was observed as a peak in the excursions of the simulated membrane potential waveform (maximum range of the envelope), which occurs at the time in the simulation when the instantaneous frequency of the ZAP signal was near the model's resonance frequency. The resonant frequency was calculated in the model using the same techniques used for calculating resonant frequency in the experimental data, as described in the data analysis section above. To show the relationship of the resonant frequency to biophysical parameters of the model, the magnitude and inverse time constant of I_h were also plotted for different membrane potentials.

2.3 Results

2.3.1 Anatomy and morphology of Layer II EC cells

Our focus in this study was to analyze the effect of differences in mean membrane potential on the resonant frequency of neurons in entorhinal cortex. The effect of membrane potential on resonant frequency was measured from neurons at different positions along the D/V and M/L axis in layer II of medial and lateral EC, respectively.

Figure 1 shows photographs of horizontal (Fig. 2.1A-D) and coronal (Fig. 2.1E-H) sections along the D/V and M/L axis of medial and lateral EC, respectively. Two magnifications are shown in order to show cell location within layer II of the slice as well as morphological detail. Cells of medial EC had radiating dendrites in all directions resembling the morphology of stellate cells (Alonso and Klink, 1993), while cells of lateral EC had dendrites extending horizontally across layer II and vertically into layer I, resembling the morphology of fan cells (Tahvildari and Alonso, 2005). To better describe the coverage of medial and lateral EC, figure 2.2 shows the estimated recording sites of medial (n=53 of 87) and lateral (n=43 of 43) EC cells from horizontal and coronal sections, respectively. Our recording sites tended to stay within 2 mm of the caudo-medial tip of the medial EC and within the dorsolateral band (close to the rhinal sulcus) of lateral EC.

2.3.2 Physiology of medial and lateral EC cells

Figure 2.3 shows recordings of membrane potential from neurons in medial and lateral EC. Insets show a closer look at subthreshold voltage traces. In both medial and

lateral EC, sMPOs appeared between clusters of action potentials (Fig. 2.3A, D, asterisk). Subsequent current steps to values beyond threshold increased the duration and the number of spikes within a cluster, generating a train of action potentials (Fig. 2.3A, arrowhead). Cluster firing was defined as in previous studies (Klink and Alonso, 1993; Fransén et al., 2004) as cells displaying clear groups of spikes, often doublets or triplets, in which spiking events were separated by periods of sMPOs. There was a large difference between the responses of medial and lateral EC cells to nine successive 50 pA hyperpolarizing step currents. All medial EC cells showed large sag potentials in response to hyperpolarizing current steps (see Fig. 2.3B for individual traces and Fig. 2.3C for the mean sag across the population), while cells of lateral EC showed much smaller sag potentials at all hyperpolarization levels (Fig. 2.3E and 2.3F). Cells in medial EC showed rebound depolarization and spiking (Fig. 3B, asterisk) after hyperpolarizing current injection.

2.3.3 Resonant frequency varies with anatomical location

After examining cellular responses to depolarizing and hyperpolarizing current steps, ZAP stimuli were delivered at various membrane potentials in order to measure the resonant frequencies of each cell. Consistent with previous studies, we found from these experiments that along the dorsal to ventral axis of medial EC, cells showed a gradient in the resonant frequencies near resting potential such that higher frequencies were found in more dorsal regions and lower frequencies in more ventral regions. Figures 2.4A-C and D-F depict recordings with holding potentials of -65 mV from three medial and three lateral EC cells, respectively. In the medial EC, the resonant frequency decreased as a

function of distance from the dorsal surface of the brain (A: 3.6 mm, 7.81 Hz; B: 5.0 mm, 6.16 Hz; and C: 6.7 mm, 3.97 Hz). However, in lateral EC, the resonant frequency was almost always under 2 Hz, regardless of the distance from the rhinal sulcus (coronal, D: 0.56 mm, 1.26 Hz; E: 0.92 mm, 0.88 Hz; and F: 1.81 mm, 0.76 Hz) or the dorsal surface of the brain (horizontal).

Since ZAPs were delivered at different membrane potentials, analyses of resonant frequency by D/V position were done in 2 mV voltage bins according to the cell's membrane potential in each recording. Figures 2.5A-E show plots of resonant frequency as a function of D/V position for five different voltage bins of medial EC cells as well as resultant r^2 values for linear fits to the data (A, -56.5 to -54.5 mV, $r^2 = 0.00908$; B, -60.5 to -58.5 mV, $r^2 = 0.595$; C, -62.5 to -60.5 mV, $r^2 = 0.299$; D, -64.5 to -62.5 mV, $r^2 = 0.353$; E, -70.5 to -68.5 mV, $r^2 = 0.0246$). At voltages near the resting membrane potential (Fig. 2.5B-D), the resonant frequency clearly decreased along the D/V axis in the medial EC. However, at membrane potentials away from rest, slopes flattened out, suggesting the relationship between resonant frequency and membrane potential is weaker at these voltages. Unlike medial EC cells, Figures 2.5F-O show that the lateral EC cells lacked resonant properties regardless of their anatomical position in both horizontal (F-J) and coronal (K-O) sections.

2.3.4 Resonant frequency varies with voltage

An important result from the ZAP analyses was the inverse linear relationship found between membrane potential and resonant frequency in all cells of the medial EC. Figures 2.6A-C show that as the membrane potential becomes more depolarized the

resonant frequency decreases, or stated another way, as the membrane potential becomes more hyperpolarized, the resonant frequency increases (A: -62 mV, 3.387 Hz; B: -67 mV, 4.792 Hz; and C: -72 mV, 6.042 Hz). The linear relationship between resonant frequency and membrane potential between -70 and -55 mV can be seen in the plots for three individual medial entorhinal neurons in dorsal medial regions in Figure 2.6G and in ventral medial regions in Figure 2.6H. The linear relationship in this membrane potential range was seen in every cell of the medial EC (see later figures). In contrast, in the lateral EC, almost all cells showed resonant frequencies of less than 2 Hz across all membrane potentials. Three examples of this are shown in figures 2.6D-F. Only a few cells in lateral EC showed resonant frequencies above 2 Hz, and those that did had frequencies that were always below 3 Hz. Examples of the resonant frequency at different membrane potentials in individual dorsal and ventral lateral EC neurons are shown in Figure 2.6I and 2.6J.

2.3.5 Biophysical simulations of resonance properties

We simulated the inverse linear relationship between membrane potential and resonant frequency by constructing a biophysical model of layer II medial EC stellate cells. We performed simulations with various holding currents in order to systematically test the effect of mean membrane potential on the resonant frequency. In Figures 2.7A-D, example voltage and impedance traces are shown for four mean membrane potentials, while Figure 2.7E shows the voltage dependence of the I_h channel activation, inverse time constant, and the resonant frequency. At more hyperpolarized membrane potentials, the I_h activation and inverse time constant are large, leading to higher resonant

frequencies. As the model cell becomes more depolarized, activation of I_h and its inverse time constant decrease, resulting in lower resonant frequencies. It is important to note that at membrane potentials between -55 to -70 mV the simulations gave an approximately linear relationship with a negative slope. This result is in agreement with what was found experimentally. At more hyperpolarized membrane potentials (-70 to -85 mV) tested in the biophysical model, the activation of I_h approaches its maximum, causing the resonant frequency to approach an asymptotic level.

2.3.6 Experimental controls

We then checked to see if this same phenomenon of approach to an asymptotic level occurred *in vitro*, by measuring the resonant frequency at more hyperpolarized levels (-55 to -80 mV, n=17) and (-60 to -90 mV, n=7) in layer II medial EC cells. The results of these experiments (Figures 2.8A-F, I) show that at membrane potentials below -70 mV, the resonant frequency approaches an asymptotic value, suggesting saturation to a maximum resonant frequency. Figure 2.8 also highlights some other important findings of this study. Controls recorded at different time points ten minutes apart show that the resonant frequency was very stable (Fig. 2.8A-B) and we found the resonant frequency does not show hysteresis (Fig. 2.8C-F). We measured the voltage dependence of resonance in four different ways. First, as was done for all other cells, the resonant frequency was measured from hyperpolarized to depolarized membrane potentials. This was usually done without returning the membrane potential to rest between individual holding potentials. However, in cells shown in Figures 2.8C-D, we stepped to rest before each step in the depolarized direction. We also reversed the voltage direction in which

we measured the resonant frequency, so as to start at -55 mV and end at -80 mV. Additionally, we measured the resonant frequency at randomly chosen voltages. In all cases (n=14 cells) the voltage direction did not appreciably alter the voltage dependence of the resonant frequency. To ensure our results were not influenced by the use of different amplitudes of the ZAP stimulus, we held medial EC cells (n=6) at three different potentials (-65, -70, and -75 mV) and measured the resonant frequency with 40, 80, 120, and 200 pA peak-to-peak amplitude ZAP stimuli at each potential. In all six cells we found that the resonant frequency was very similar at a given potential, regardless of the ZAP amplitude used. Examples from two cells are shown in Figures 2.8G-H.

2.3.7 Pharmacological blockade of HCN channels

The correlation between the presence of I_h and resonant properties prompted experiments where the I_h blocker, ZD7288, was applied to medial EC cells. These experiments abolished both the sag potential (not shown) and the resonant properties (Fig. 2.9A-C, n = 3) in medial EC cells. In addition, the firing properties of the medial EC cells became very similar to those in the lateral EC, and stopped showing firing of spikes in clusters.

2.3.8 Resonance slope along the dorsal-ventral axis of medial EC

We then pooled the medial EC data measuring the resonant frequency from -55 to -70 mV and from -55 to -80 mV. The finding of higher resonant frequencies in dorsal medial EC compared to ventral medial EC still held true (Fig. 2.10A-B). In addition,

across the population the dorsal cells showed more of an asymptotic approach to a maximum across membrane potentials compared to the ventral population. Lastly we investigated how the slope of resonance versus membrane potential (Hz/mV) changes for individual cells along the D/V axis of the medial EC. For all cells (n=87) we looked at the slope of resonant frequency versus membrane potential computed across the full range of membrane potentials from -80 to -55 mV (Fig. 2.10C) and a more limited range from -70 to -55 mV (Fig. 2.10D). In both analyses, the difference in slope of resonance frequency versus membrane potential showed an apparent negative trend along the D/V axis, but this trend did not reach statistical significance (Fig. 2.10C-D).

2.4 Discussion

2.4.1 Summary of findings

The physiological results presented here show a systematic difference in resonance frequency with mean membrane potential in neurons of the medial EC. This can be described as an increase in resonance frequency with hyperpolarization or a decrease in resonance frequency with depolarization. This change in resonance frequency with mean membrane potential appears to be linear in the range from -70 to -55 mV, and shows an asymptotic approach to a maximum frequency at more hyperpolarized levels. The change in resonance frequency was tested at anatomical positions along the D/V axis of medial EC. Consistent with previous studies (Giocomo et al., 2007; Giocomo and Hasselmo, 2008b; Giocomo and Hasselmo, 2008a; Giocomo and Hasselmo, 2009; Boehlen et al., 2010), the resonance frequency shows a gradient from

higher frequencies in dorsal neurons to lower frequencies in ventral neurons, but this gradient primarily appears at membrane potentials around resting potential. The gradient does not appear at more hyperpolarized membrane potentials, potentially due to the asymptotic approach to a limiting frequency at more hyperpolarized membrane potentials, as demonstrated in both the experimental data and in the biophysical simulation. The asymptotic approach to a limiting frequency was suggested by previous data showing similar resonance frequencies at -70 and -80 mV (Nolan et al., 2007).

A recent study reported that as animals mature, cells in the dorsal medial EC change their frequency preference two-fold, while the preference of ventral cells remains relatively unchanged (Boehlan et al., 2010). Because we used animals at ages (p17-21) where the network is still developing, cells in dorsal medial EC would be expected to have greater variability in their resonant frequencies compared to ventral cells. The combined factors of increased variability and the asymptotic approach to a limiting frequency could be reasons why the systematic decrease in resonance frequency along the D/V axis was obfuscated at membrane potentials away from rest. The age of the animals did not affect the linear relationship between membrane potential voltage and resonant frequency as every resonant cell showed this relationship regardless of the age of the animal.

2.4.2 Implications

The data also show a clear difference in resonance properties of medial versus lateral EC that further supports the proposal that intrinsic resonance properties of entorhinal neurons contribute to the spatial periodicity of grid cells, as the distribution of

resonance in medial but not lateral EC shown here is consistent with the appearance of grid cells in medial EC (Fyhn et al., 2004; Hafting et al., 2005; Hafting et al., 2008) and the relative absence of spatial information in the response of neurons in the lateral EC (Hargreaves et al., 2005; Yoganarasimha et al., 2010). Our data showing the relative absence of resonance properties in lateral EC is also consistent with the smaller amplitude of theta rhythm oscillations observed in lateral versus medial EC (Deshmukh et al., 2010) and previous observations on lesser membrane potential oscillations in lateral EC (Tahvildari and Alonso, 2005). It should be noted however, that given that the majority of our lateral EC data was recorded from the dorsolateral band, lateral EC cells in more intermediate and ventral positions could possibly possess resonance and oscillation properties. This could function as a possible mechanism to aid frequency dependent information flow between the medial EC and lateral EC. Anatomical studies have shown that synaptic contacts between medial and lateral EC are limited, but indeed present (Dolorfo and Amaral, 1998; Rowland et al., 2011).

The anatomical distribution of resonance properties is consistent with oscillatory interference models that link intrinsic frequencies and the generation of grid cells (Burgess et al., 2007; Hasselmo et al., 2007). Similarly, the important role of head direction input for grid cell generation in oscillatory interference models (Burgess et al., 2007; Hasselmo et al., 2007) and CANN models (Fuhs and Touretzky, 2006; McNaughton et al., 2006; Gaussier et al., 2007; Guanella et al., 2007; Burak and Fiete, 2009) is also consistent with the selective anatomical input from the dorsal presubiculum to the medial but not the lateral EC (Witter et al., 1989; Witter and Moser, 2006). The

dorsal presubiculum (postsubiculum) providing this input shows strong head direction response properties (Taube et al., 1990; Taube and Bassett, 2003; Brandon et al., 2012) as well as intrinsic properties that could assist in persistence of head direction coding (Yoshida and Hasselmo, 2009).

How does resonance underlie the spatial periodicity of grid cells? Early models focused on the fact that the same intrinsic properties that generate resonance also generate membrane potential oscillations, and used oscillatory interference between membrane potential oscillations within single neurons. But as described in the introduction, models using membrane potential oscillations have problems with the variance of sMPO periods (Giocomo and Hasselmo, 2008a; Welinder et al., 2008; Zilli et al., 2009), with the synchronization properties of sMPOs (Remme et al., 2009), and with the lack of linear changes in sMPO frequency with membrane potential (Yoshida et al., 2011), though it is possible that high density of I_h in distal dendrites allows more local interference interactions (Magee, 1998).

As an alternative, our data show that the resonance properties of neurons provide an intrinsic frequency that changes in a linear manner for membrane potentials between -70 and -55 mV. This resonance may contribute to local circuit oscillations involving interactions of populations of excitatory cells, or interactions of excitatory cells with inhibitory cells (Zilli and Hasselmo, 2010). Neurons responsive to running speed (Sharp, 1996; O'Keefe et al., 1998) and head direction (Taube et al., 1990; Taube and Bassett, 2003; Sargolini et al., 2006) might depolarize membrane potential and thereby shift the frequency of local circuit interactions that generate grid cell periodicity. Note that the

oscillatory interference models of grid cells work just as well with both a positive and a negative slope of frequency to velocity (Giocomo and Hasselmo, 2008a), as long as the difference in frequencies shows a linear relationship with running velocity. A linear relationship between resonance frequency and depolarization appears between -70 and -55 mV in the data presented here. This means that the difference in resonant frequency between neurons would change linearly with changes in membrane potential in this range. In fact, the nonlinear relationship of frequency to membrane potential found when extending to membrane potentials below -70 mV in the data presented here could be compensated by a nonlinear change in input with velocity (Zilli and Hasselmo, 2010).

The resonance properties of excitatory cells might interact with a theta rhythmic input to interneurons in the EC from the medial septum (Alonso and Kohler, 1984). This is consistent with the recent data showing that reduction of theta rhythm oscillations in the EC by pharmacological infusion of muscimol in the medial septum is associated with a loss of spatial periodicity in grid cells (Brandon et al., 2011; Koenig et al., 2011), but with maintenance of head direction responses (Brandon et al., 2011) and place cell responses (Koenig et al., 2011). Interactions of the resonance frequency with a network theta rhythm oscillation could also underlie the phenomenon of theta cycle skipping that appears in the many medial entorhinal neurons (Deshmukh et al., 2010), and is reduced during infusions of muscimol into the medial septum (Brandon et al., 2011).

The data do not show a significant difference in slope of resonance frequency to membrane potential at different D/V positions. A difference in slope would be interesting as differences in the properties of resonance frequency at different D/V

positions (Giocomo et al., 2007; Boehlen et al., 2010) could underlie the difference in both spacing and size of grid cell firing fields along the D/V axis. The change in spacing and size of grid cell firing fields observed in association with the novelty of environments (Barry et al., 2008; 2012) could arise from novelty-induced changes in acetylcholine levels in cortical structures (Acquas et al., 1996) that activate muscarinic receptors to change the resonance frequency of stellate cells in medial EC (Heys et al., 2010).

In the oscillatory interference models, the lack of resonance properties in lateral entorhinal neurons would result in a lack of spatial periodicity of these neuron responses. The oscillatory interference models provide a clear link between intrinsic properties of neurons and the functional grid cell firing properties, including properties of theta phase precession by grid cells (Burgess, 2008; Hafting et al., 2008) and the dependence of intrinsic frequency of grid cells on running speed and size of grid fields (Jeevajee et al., 2008). This link is less apparent in other models of grid cells, such as the attractor dynamic models that depend on patterns of synaptic connectivity rather than the intrinsic properties of neurons (Fuhs and Touretzky, 2006; McNaughton et al., 2006; Burak and Fiete, 2009). However, recent models combine attractor dynamics with intrinsic properties such as the medium AHP (Storm, 1989) to account for features of grid cells such as theta phase precession (Navratilova et al., 2012). Another type of model uses intrinsic properties to generate grid cell responses via self-organization of afferent input (Kropff and Treves, 2008).

The non-spatial properties of lateral entorhinal neurons has led to proposals that they play a role in the coding of objects or items to be associated with the spatial or

temporal context coded by medial EC (Hargreaves et al., 2005; Witter and Moser, 2006; Eichenbaum and Lipton, 2008). In this framework, a spatiotemporal trajectory may be encoded by interactions of the medial EC and hippocampus, and associations with events or items at specific spatiotemporal positions along the trajectory could involve interactions of neurons in the medial EC coding space and time with neurons in the lateral EC coding items and objects associated with specific events (Hasselmo, 2009).

2.5 Tables

Table 1. Model parameters

Table of Model Parameters	
Parameters	Citations
I_h fast activation	
dorsal:	
$\tau_m = 29.5 / (\exp[(V_m + 99) / (-15.4)] + \exp[(V_m + 25.1) / 9.64])$	Fransén et al. (2004), Giocomo & Hasselmo (2008a)
$m_\infty = 1 / (1 + \exp[(V_m + 68.1) / 7.14])$	Giocomo & Hasselmo (2008a)
ventral:	
$\tau_m = 327 / (\exp[(V_m + 40.1) / (13.6)] + \exp[(V_m + 70.2) / (-23.8)])$	Fransén et al. (2004), Giocomo & Hasselmo (2008a)
$m_\infty = 1 / (1 + \exp[(V_m + 68.1) / 5.46])$	Giocomo & Hasselmo (2008a)
I_h slow activation	
dorsal:	
$\tau_m = 357 / (\exp[(V_m + 30.6) / 6] + \exp[(V_m + 116) / (-41)])$	Fransén et al. (2004), Giocomo & Hasselmo (2008a)
$m_\infty = 1 / (1 + \exp[(V_m + 68.1) / 7.14])$	Giocomo & Hasselmo (2008a)
ventral:	
$\tau_m = 459 / (\exp[(V_m + 39.5) / 6.1] + \exp[(V_m + 90.6) / (-13.8)])$	Fransén et al. (2004), Giocomo & Hasselmo (2008a)
$m_\infty = 1 / (1 + \exp[(V_m + 66.1) / 5.46])$	Giocomo & Hasselmo (2008a)
I_{NaP} activation	
$m_\infty = 1 / (1 + \exp[(V_m + 48.7) / (-4.4)])$	Fransén et al. (2004)
I_{NaP} inactivation	
$\tau_h = 1 / (\alpha + \beta)$	Magistretti & Alonso (1999)
$\alpha = V_m V_m$	Magistretti & Alonso (1999)

$\beta = V_m$	Magistretti & Alonso (1999)
$h_\infty = 1/(1 + \exp[(V_m + 48.8)/9.98])$	Magistretti & Alonso (1999)
fast sodium I_{Na} activation	
$\tau_m = 1/(\alpha + \beta), m_\infty = \alpha\tau$	Traub et al. (1991)
$\alpha = V_r - V_r$	Traub et al. (1991)
$\beta = V_r - V_r$	Traub et al. (1991)
$V_r = V_m + 54$	Traub et al. (1991)
fast sodium I_{Na} inactivation	
$\tau_m = 1/(\alpha + \beta), m_\infty = \alpha\tau$	Traub et al. (1991)
$\alpha = 0.128 \exp[(V_r - 17)/(-18)]$	Traub et al. (1991)
$\beta = 4/(1 + \exp[(V_r - 40)/(-5)])$	Traub et al. (1991)
delayed rectifier I_K activation	
$\tau_m = 1/(\alpha + \beta), m_\infty = \alpha\tau$	Traub et al. (1991)
$\alpha = V_r - V_r$	Traub et al. (1991)
$\beta = 0.25 \exp[(V_r - 20)/(-40)]$	Traub et al. (1991)
$V_r = V_m + 54$	Traub et al. (1991)

2.6 Figures

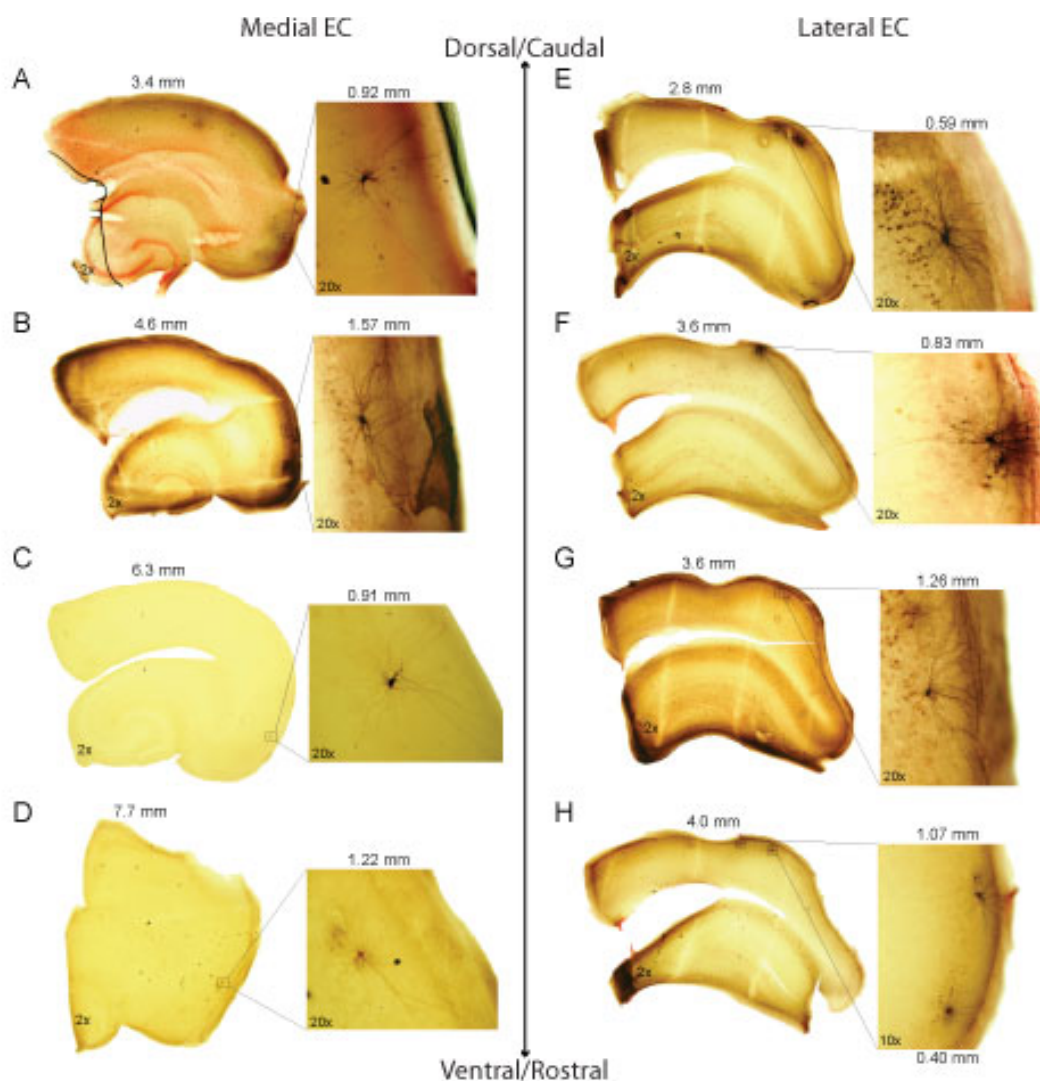


Figure 2.1 Anatomy and morphology in layer II cells of medial and lateral EC

(A-H) Panels in the left and right columns correspond to photomicrographs taken from medial EC in horizontal sections and lateral EC in coronal sections, respectively. In each panel, images on the left correspond to 2x magnification of the section in order to show the location of cells within each slice. Numbers correspond to the distance (mm) of each section from the dorsal (horizontal section, medial EC) or the caudal (coronal section, lateral EC) surface of the brain. Images on the right correspond to 20x (A-G) or 10x (H) magnification in order to show the detailed morphology of each cell. Numbers correspond to the distance (mm) of each cell from either the caudo-medial tip of the horizontal slice (medial EC) or the center of the rhinal sulcus of the coronal slice (lateral EC). (A-D) Cells of the medial EC show radiating dendrites in all directions indicative of stellate cells. (E-H) Cells of the lateral EC have dendrites that radiate horizontally across layer II and vertically into layer I, indicative of fan cells.

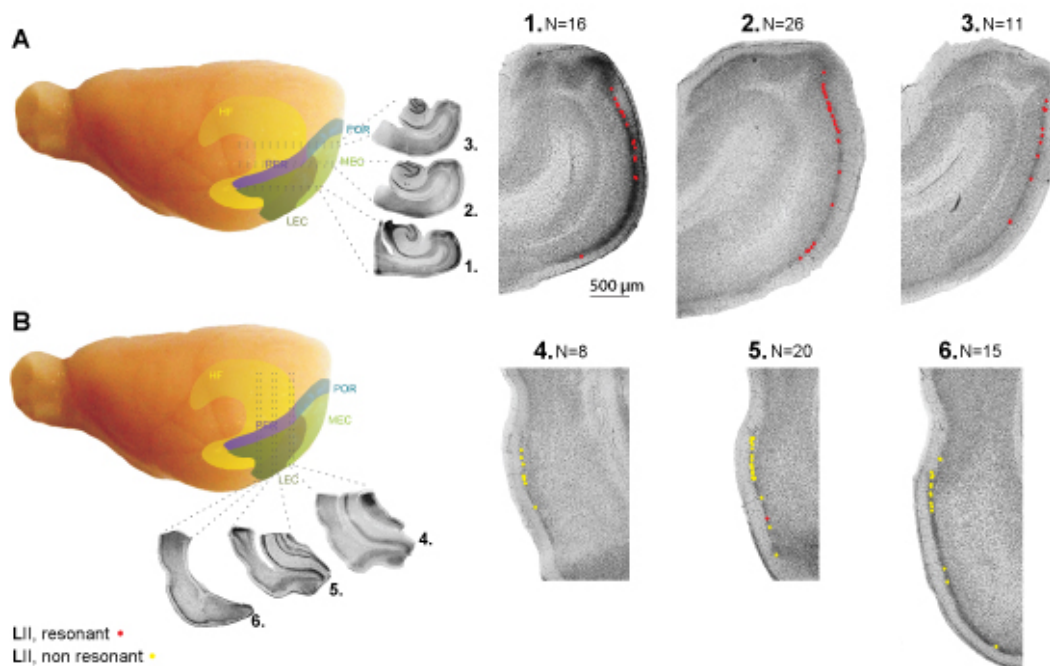


Figure 2.2 Slice orientation and anatomical location of recording sites in medial and lateral EC

(A-B) A whole brain schematic depicting relative positions of the hippocampal formation and surrounding parahippocampal regions, as well as horizontal and coronal slice orientations. (1-3 left) Photomicrographs of representative whole slices taken along the D/V axis of medial EC from ventral (1, n=16), intermediate (2, n=26) to dorsal (3, n=11) locations. (1-3 right) Higher power photomicrographs show the relative positions of recordings in medial EC layer II. Note: anatomical coordinates not available for every recorded cell (n=53 of 87). (4-6 left) Photomicrographs of representative whole slices taken along the M/L axis of lateral EC from caudal (4, n=8), intermediate (5, n=20), and rostral (6, n=15) locations. (4-6 right) Higher power photomicrographs show relative positions of recordings in lateral EC layer II (n=43 of 43). Red dots represent cells displaying resonance, and yellow dots represent non-resonant cells. Abbreviations: HF, hippocampal formation (yellow); POR, postrhinal cortex (blue); PER, perirhinal cortex (purple); MEC, medial entorhinal cortex (light green); and LEC, lateral entorhinal cortex (dark green). Figure adapted with permission from Canto and Witter, 2012a, b.

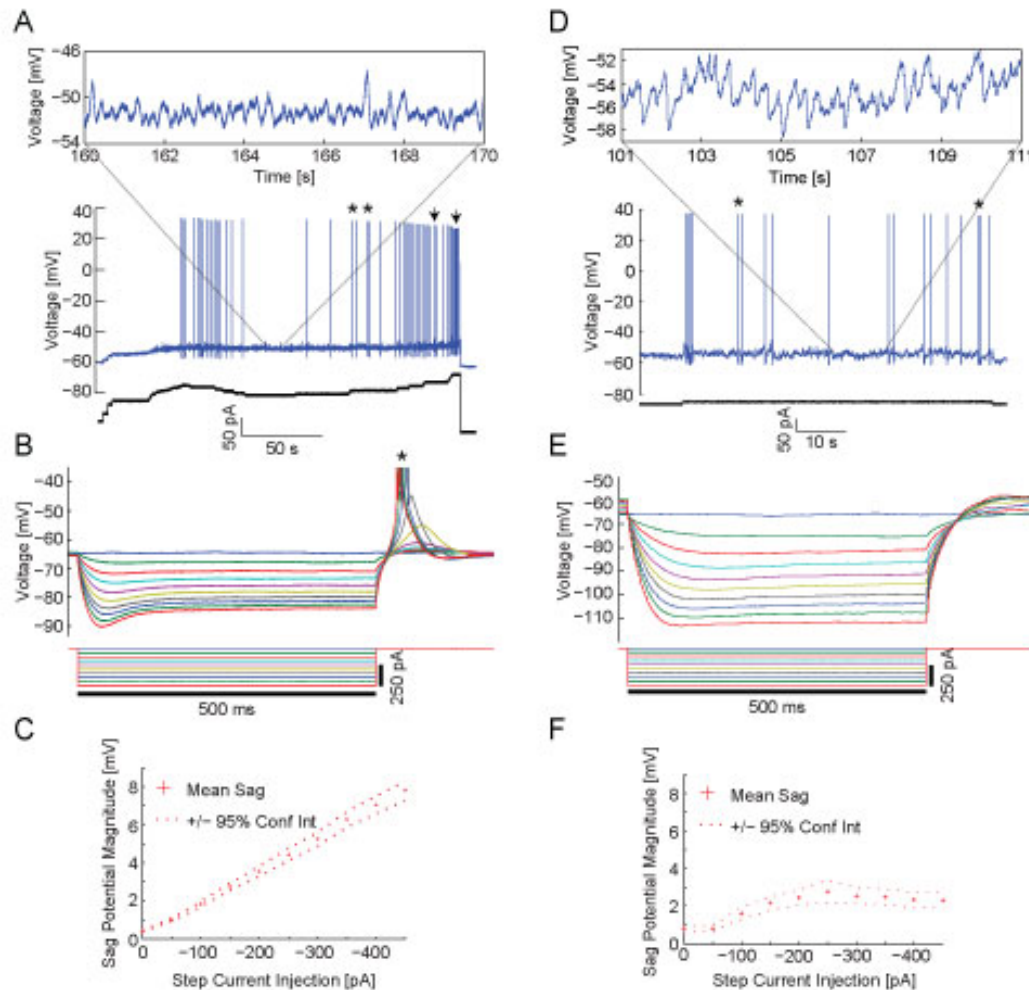


Figure 2.3 Physiological properties differ between cells of medial and lateral EC

(A-F) Panels in the left and right columns correspond to data from a single cell in medial EC and lateral EC (coronal), respectively. (A) As the holding current is gradually increased, medial EC cells display spike clustering near threshold (asterisks) that turns into trains of spikes (arrowheads) at more suprathreshold membrane potentials. In between clusters, medial EC cells display subthreshold oscillations (inset). (D) Overall, cells of the lateral EC (coronal and horizontal sections) were very excitable, requiring smaller input currents (bottom of panels A and D) to elicit spiking compared to cells of the medial EC. The inset shows the presence of oscillations in one example cell in lateral EC. (B, E) In response to nine successive -50 pA current steps, sag potentials, likely dependent on I_h , are displayed in cells of medial EC (B) but not lateral EC (E). Often, medial EC cells displayed rebound spikes following the release from the step current. (B) These rebound spikes (asterisk) are truncated to enhance visualization of the sag potentials. (C, F) Among all cells recorded, the mean sag potential across all hyperpolarizing steps was nearly 4-fold larger for medial EC cells (C, $n=65$) compared to lateral EC cells recorded from coronal sections (F, $n=43$).

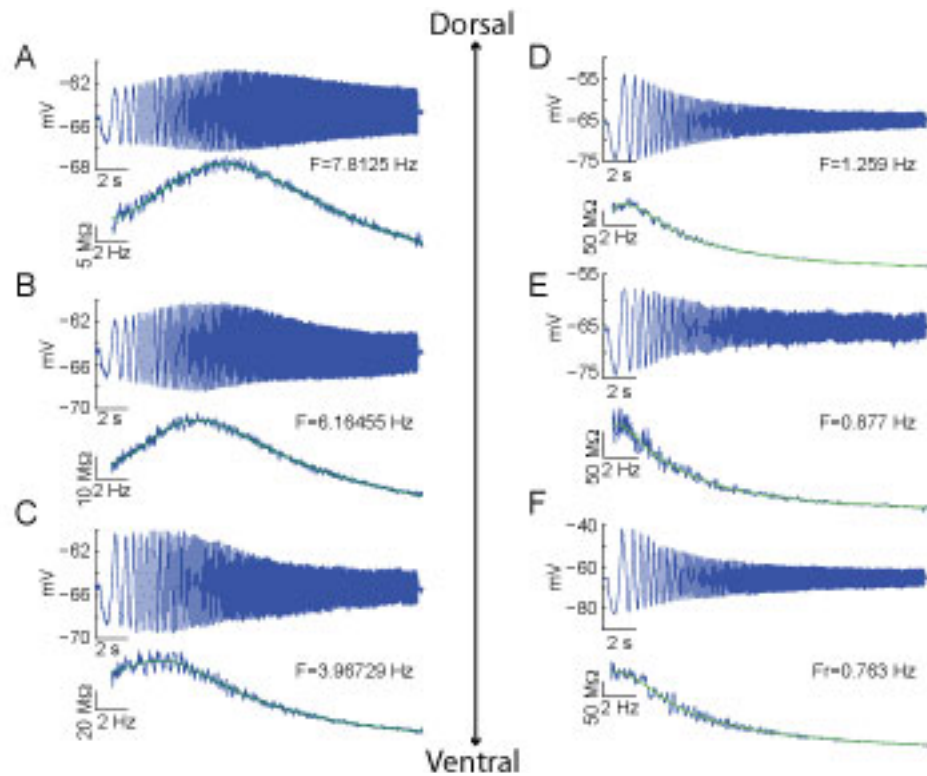


Figure 2.4 Resonant frequency decreases along the D/V axis of medial EC

(A-F) ZAP stimuli (not shown) were set to appropriate amplitudes that ensured subthreshold membrane potential dynamics. For each recording, the cell's membrane potential response is on top, and below is the cell's impedance as well as the impedance curve fit to estimate the cell's resonant frequency from the peak of the curve. In these figures, each cell was held with a holding current to a mean membrane potential of -65 mV. (A-C) Example recordings from medial EC cells at three different D/V depths (A 3.6 mm, B 5.0 mm, and C 6.7 mm from the dorsal surface). The resonant frequency decreases as a function of distance from the dorsal surface of the brain. (D-F) Example recordings from lateral EC cells (coronal sections) at three different D/V depths (D 0.555 mm, E 0.919 mm, and F 1.812 mm from the rhinal sulcus). Unlike medial EC, cells in lateral EC have resonant frequencies below 2 Hz, regardless of their M/L position.

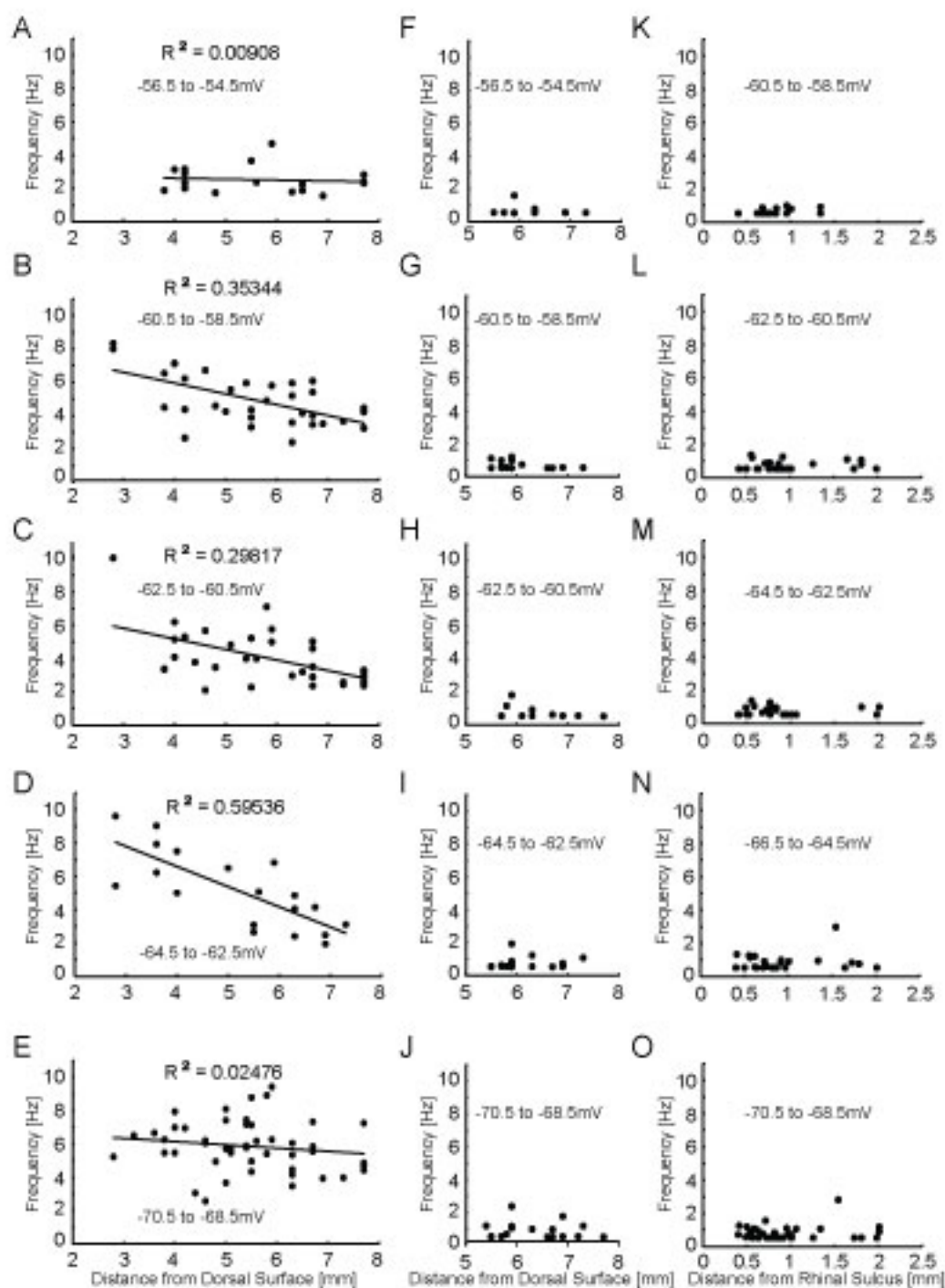


Figure 2.5 The medial EC population shows a clear decrease of the resonant frequency along the D/V axis at membrane potentials near resting potential

(A-J) Resonant frequencies, recorded from horizontal sections, are plotted as a function of D/V distance according to 2 mV membrane potential bins (A, F, -56.5 to -54.5 mV; B,

G, -60.5 to -58.5 mV; **C, H**, -62.5 to -60.5 mV; **D, I**, -64.5 to -62.5 mV; and **E, J**, -70.5 to -68.5 mV). (**A-E**). In the membrane potential bins near rest (**B-D**) the resonant frequency in medial EC cells decreased with increasing distance from the dorsal surface. However, at membrane potentials away from rest the slopes flattened out (**A, E**). (**F-J**) Independent of membrane potential and position along the dorsal to ventral axis, lateral EC cells rarely have resonant frequencies above 2 Hz. (**K-O**) Similar to recordings in horizontal sections, lateral EC cells recorded from coronal sections rarely have resonant frequencies above 2 Hz regardless of D/V position or membrane potential (**K**, -60.5 to -58.5 mV; **L**, -62.5 to -60.5 mV; **M**, -64.5 to -62.5 mV; **N**, -66.5 to -64.5 mV; **O**, 70.5 to -68.5 mV).

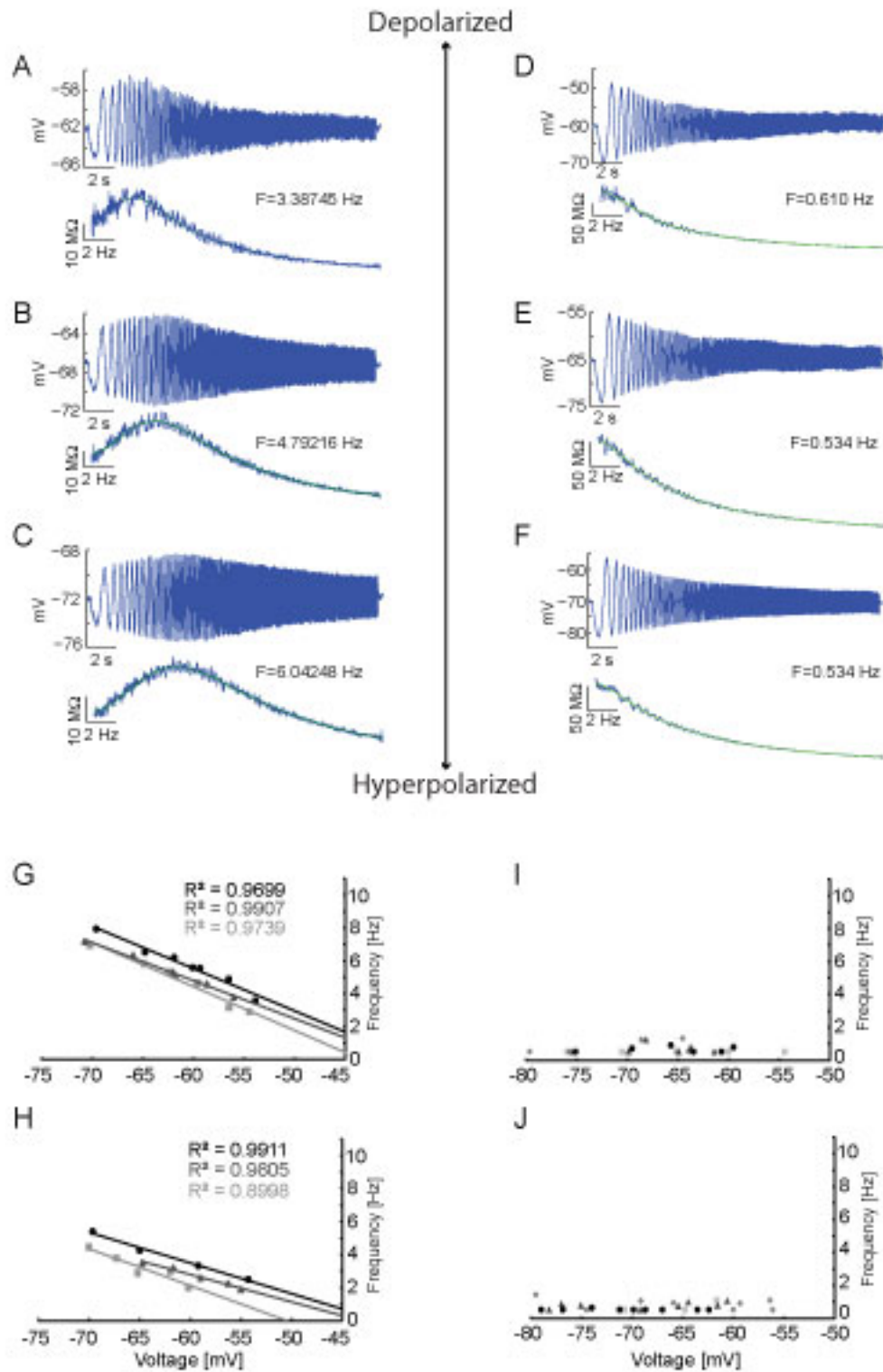


Figure 2.6 Resonant frequency decreases with membrane potential depolarization in medial EC

(A-F) ZAP stimuli were set to appropriate amplitudes that ensured subthreshold membrane potential dynamics. For each recording, the cell's membrane potential response is on top, and below is the cell's impedance as well as the impedance curve fit to estimate the cell's resonant frequency from the peak of the curve. (A-C) The membrane potential dependence of the resonant frequency is exemplified in three recordings from a single cell in medial EC, 3.8mm from the dorsal surface of the brain. At membrane potentials of -62 mV (A), -67 mV (B) and -72 mV (C) the resonant frequencies were 3.39 Hz, 4.79 Hz, and 6.04 Hz, respectively. (D-F) In contrast, three recordings from a lateral EC cell (coronal section), show that at -60 mV (D), -65 mV (E) and -70 mV (F), the resonant frequency is below 2 Hz. (G-H) Plots of resonant frequency versus membrane potential are shown for three individual cells in dorsal medial EC (G, circle, 4 mm; triangle, 3.8 mm; and square, 4.2 mm from dorsal surface) and ventral medial EC (H, circle, 5.8 mm; triangle, 6.5 mm; and square, 6.3 mm from dorsal surface). In cells of the medial EC (G, H), there is an inverse linear relationship between membrane potential and resonant frequency. (I, J) In contrast, lateral EC cells lack resonant properties in both dorsal (I, circle, 1.010 mm; triangle, 0.834 mm; square, 0.621 mm; and diamond, 0.415 mm from the rhinal sulcus) and ventral lateral EC (J, circle, 1.986 mm; triangle, 1.812 mm; square, 1.651 mm; and diamond, 1.344 mm from the rhinal sulcus). Cells in dorsal medial EC (G) have higher resonant frequencies than in ventral medial EC (H).

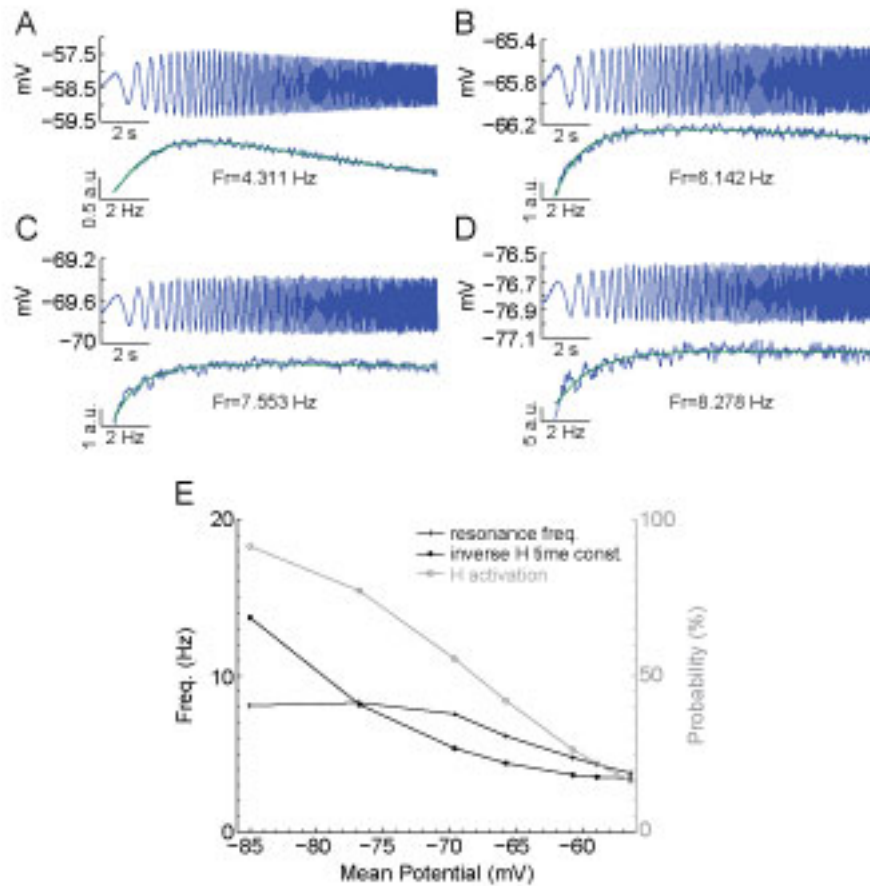


Figure 2.7 Biophysical model of medial EC cells displays relationship between increase in membrane potential and decrease in resonant frequency

(A-D) Simulated membrane potential trace (top), impedance, and impedance curve fits (bottom) at 4 different membrane potentials (A -58.5 mV, B -65.8 mV, C -69.6 mV, and D -76.8 mV). At depolarized membrane potentials close to threshold, the resonant frequency is decreased compared to the more hyperpolarized membrane potentials. (E) Summary plot of biophysical simulations show that as membrane potential is hyperpolarized, the resonant frequency increases linearly until saturation occurs with approach to an asymptotic frequency between -70 and -85 mV. The inverse H-current time constant and activation both increase as the membrane potential is hyperpolarized, contributing to the increase in frequency with hyperpolarization. Abbreviations: a.u., arbitrary units.

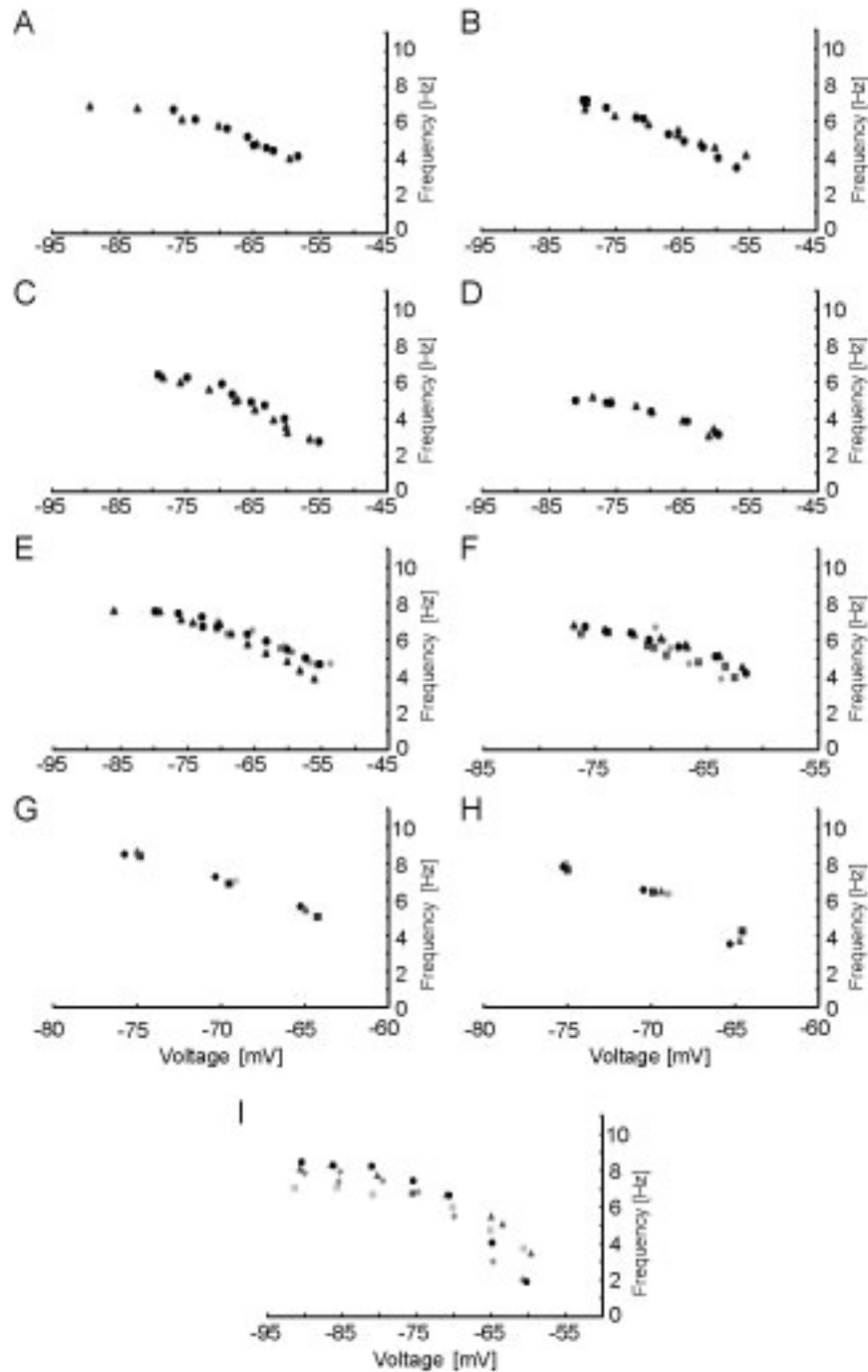


Figure 2.8 The resonant frequency in medial EC approaches an asymptotic value at membrane potentials below -70 mV, does not display hysteresis, and is not affected by the amplitude of the ZAP stimulus

(A-B) The resonant frequency shown at more hyperpolarized potentials (-80 to -55 mV, circles) in two different cells. After ten minutes resonance frequency was measured again (triangles) in order to test the stability of the resonant frequency. Both example

cells show no appreciable difference at different times, and both show an asymptotic approach to a maximum frequency. **(C-D)** The resonance frequency was measured from -80 to -55 mV (circles) and then re-measured with steps to rest before each step to a more depolarized potential (triangles). **(E-F)** The resonant frequency was initially measured sequentially from -55 to -80 mV (circles), and then the order of membrane potentials was switched to start at -80 and end at -55 mV (triangles). Next, random membrane potentials were chosen to measure the resonant frequency (squares). Finally the direction returned to that used initially, -55 to -80 mV (diamonds). In each case, cells did not exhibit hysteresis. All cells showed a linear relationship between the membrane potential and the resonant frequency between -55 and -70 mV that then approached an asymptote at more hyperpolarized membrane potentials. **(G-H)** The resonant frequency was measured at -65 mV, -70 mV, and -75 mV using 40 pA (diamonds), 80 pA (squares), 120 pA (triangles), and 200 pA (circles) peak-to-peak ZAP amplitude stimuli (n=6). Examples from single cells are shown **(G-H)**. In all cases the resonant frequency was very similar at a given potential for all ZAP amplitudes tested. **(I)** To highlight the asymptotic behavior of the resonant frequency four examples (n=7) are shown with membrane potentials ranging from -60 to about -90 mV. Cells were located at 3.8 mm (squares), 4.6 mm (triangles and diamonds), and 5.0 mm (circles) from the dorsal surface.

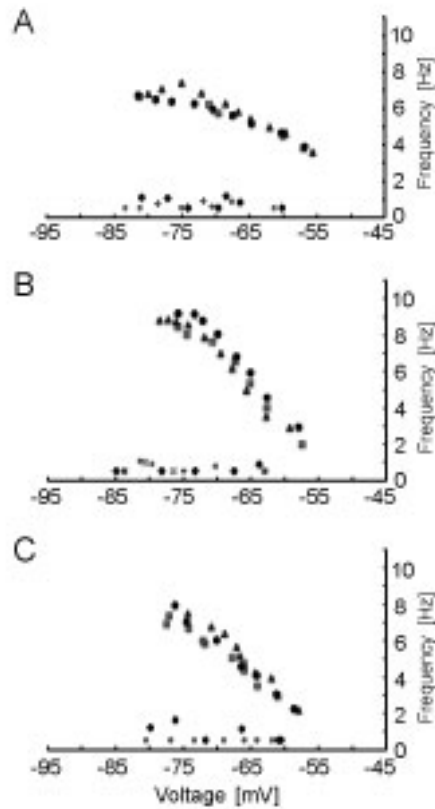


Figure 2.9 ZD7288 abolishes resonance properties in medial EC

(A-C) The resonant frequency was measured in three membrane potential directions (A, B: -55 to -80 mV, circles; -80 to -55 mV, triangles; random membrane potentials, squares and C: -80 to -55 mV, circles; -55 to -80 mV, triangles, and random membrane potentials, squares) before continuously washing 10 μ M ZD7288 into the bath. The resonant frequency was then measured after ten minutes in ZD7288 in both directions as before. Cell C was also tested using the ZAP stimulus at random mean membrane potentials. In all cases, the ZD7288 abolished the resonant frequency at all mean membrane potentials tested.

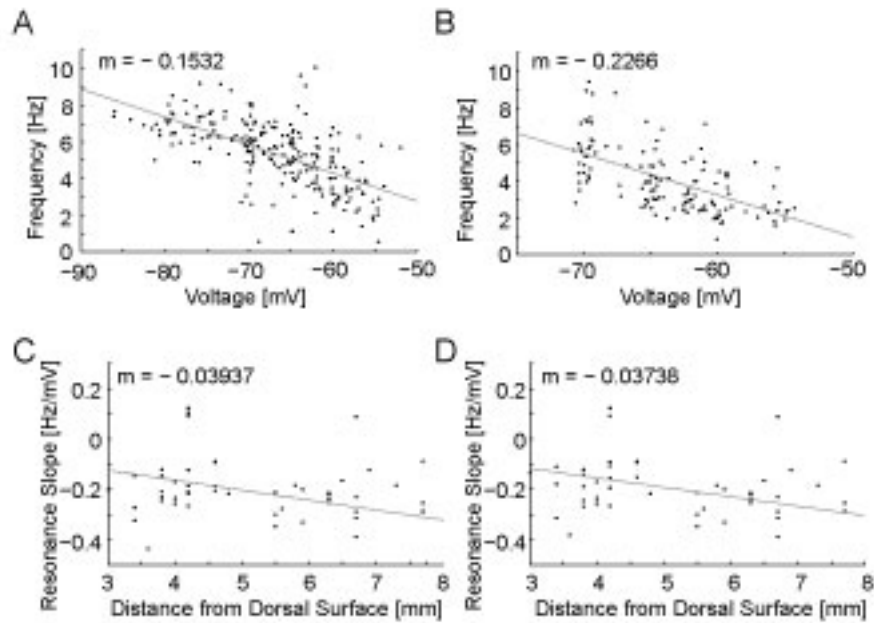


Figure 2.10 Population data showing resonant frequencies at all membrane potentials in dorsal medial EC compared to ventral EC

(A-B) Cells in the dorsal medial EC (A, $n=48$) show higher frequencies compared to ventral medial EC cells (B, $n=31$) and a clearer approach to an asymptotic frequency. (C-D) The slope of resonant frequency as a function of membrane potential is plotted for individual cells based on their distance from the dorsal surface. The slope of resonant frequencies against membrane potential was calculated for the full data from -55 to -80 mV (C) or for a smaller range from -55 to -70 mV (D) showing no significant difference along the D/V axis of the EC.

**CHAPTER 3: Rebound spiking in layer II medial entorhinal cortex stellate cells:
possible mechanism of grid cell function²**

²This work is in preparation for submission with authors Shay CF, Ferrante M, Chapman GW, Hasselmo ME.

3.1 Introduction

Layer II stellate cells of the medial EC display a number of well-studied cellular properties, including sMPOs (Alonso and Llinas, 1989; Klink and Alonso, 1993) and membrane potential resonance (Haas and White, 2002; Erchova et al., 2004; Giocomo et al., 2007, Shay, et al., 2012). Intrinsic properties of stellate cells show increases in period of oscillations along the D/V axis of medial EC (Giocomo et al., 2007; Giocomo and Hasselmo, 2008a,b; Boehlen et al., 2010) resembling the increasing gradient of grid cell firing field size and spacing (Hafting et al., 2005; Sargolini et al., 2006). Similarly the intrinsic spiking frequency of grid cells differs along the D/V axis and shows changes with running speed (Jeewajee et al., 2008). These data support the use of cellular properties to model grid cell behaviors in oscillatory interference models (Burgess et al., 2005, 2007, 2008; Blair et al., 2007, 2008; Hasselmo, 2008).

Data also support continuous attractor neural network (CANN) models, which create grid cell firing properties with recurrent inhibitory networks where movement of an activity bump is regulated by running velocity and head direction (Fuhs and Touretzky, 2006; McNaughton et al., 2006; Gaussier et al., 2007; Guanella et al., 2007; Burak and Fiete, 2009). CANN models hypothesize multiple networks or modules within medial EC. Support for modular processing within medial EC is provided by Burgalossi et al., (2011) who showed patches of cytochrome oxidase catalytic activity along the D/V axis. The incremental increase in grid cell field size and spacing along the D/V axis of medial EC provides additional support for medial EC modules (Stensola et al., 2012). Similar to the recurrent inhibitory network in CANN models, stellate cells of the medial

EC are embedded in an inhibitory network, share little to no direct synaptic connections with other stellate cells, but instead interact indirectly through inhibitory interneurons (Couey et al., 2013; Pastoll et al., 2013).

In vivo intracellular recording data suggest the most accurate account of experimental grid cell data is obtained with ‘hybrid’ models containing a combination of oscillatory interference and CANN mechanisms (Domnisoru et al., 2013; Schmidt-Heiber and Häusser, 2013). Both studies found stellate cells fired in spatially periodic patterns, suggesting they form a subset of the grid cell population found in unit recordings of the medial EC. Furthermore, both studies found membrane potential ramp depolarizations and theta oscillations during traversals of grid cell firing fields. While ramp depolarizations are indicative of sustained input (required in CANN models) theta oscillations are necessary for theta phase precession (achieved only in oscillatory interference models). A number of ‘hybrid’ models have now been published (Navratilova et al., 2012; Bush and Burgess, 2014; Hasselmo, 2013; Schmidt-Heiber and Häusser, 2013; Hasselmo and Shay, 2014).

One of these ‘hybrid’ grid cell models utilizes recurrent inhibitory network connectivity and resonance and rebound spiking properties of layer II medial EC stellate cells (Hasselmo and Shay, 2014). Rebound spikes occur in response to release from hyperpolarizing current pulses and are dependent on the presence of I_h (Alonso and Llinas, 1989; Klink and Alonso, 1993; Shay et al., 2012). The strong inhibitory innervation of stellate cells coupled with their intrinsic properties suggests a functional

role for rebound spiking. The main goal of this study was to test the viability of rebound spiking as a mechanism of grid cell function within the framework of these models.

To do this, hyperpolarizing inputs mimicking synaptic input were superimposed on a baseline sinusoidal current injection and delivered to layer II medial EC stellate cells. We analyzed the phases of hyperpolarizing inputs (relative to the baseline oscillation) that caused spikes as well as analyzing the output phases of spikes. Our results indicate that inhibitory inputs have a particular phase range that can induce spiking. In addition, output spiking occurs at a narrow phase range. The input phase preference was dependent on the presence of I_h and both input and output phases changed with oscillation frequency and magnitude of inhibitory input. When stellate cells were tuned to match rebound spiking properties found *in vitro* (Izhikevich, 2007) and placed in a network receiving inhibitory feedback and oscillatory input from medial septum (Hasselmo, 2013), spatial periodicity resembling grid cell firing was produced. These results support the hypothesis that rebound spiking could contribute to the generation of grid cells.

3.2 Materials and methods

3.2.1 Slice preparation

We investigated rebound spiking properties of stellate cells of layer II medial entorhinal cortex (EC). All experimental protocols were approved by the Institutional Animal Care and Use Committee of Boston University. Slice preparation and recording techniques were similar to those in Shay et al., 2012. Briefly, male and female Long-

Evans rat pups (postnatal days 17-21, Charles River, Wilmington, MA) were deeply anesthetized with 1-2 ml of isoflurane (Abbot Laboratories). After absence of tail and pedal reflex, brains were rapidly removed, submerged in ice-cold artificial cerebrospinal fluid (aCSF) containing (in mM) 125 NaCl, 2.0 CaCl₂, 2.5 KCl, 1.25 NaH₂PO₄, 25 NaHCO₃, 25 d-glucose, and 1.0 MgCl₂ (pH adjusted to 7.4 with 95% O₂-5% CO₂). Horizontal slices, 400- μ M thick, were made with a vibroslicer (Leica VT1000). Slices were immediately transferred to a holding chamber containing aCSF and incubated at 32°C for 30 minutes and were left at room temperature for 30 minutes before recordings began.

3.2.2 Electrophysiological recordings

Slices were placed in a recording chamber perfused with aCSF, constantly bubbled with 95% O₂-5% CO₂. In a subset of recordings (n=17), 2 mM kynurenic acid and 100 μ M picrotoxin were added to the recording solution to block glutamatergic and GABAergic synaptic transmission, respectively. All recordings were made between 35-37°C. Whole-cell pipettes were fabricated with borosilicate glass capillaries by means of a P-90 horizontal puller (Sutter Instruments). Pipettes were filled with an internal solution containing (in mM) 120 K-gluconate, 10 HEPES, 0.2 EGTA, 20 KCl, 2.0 MgCl₂, 4.0 Na₂ATP, 0.3 Na₃GTP, and 7 phosphocreatine-diTris (pH adjusted to 7.3 with KOH). In addition, 0.1% biocytin was included in the internal solution for purpose of labeling. Filled pipettes had resistances between 3-5 M Ω . Cells were visualized under an upright microscope (Olympus BX51I or Zeiss Axioskop 2) using a CMOS (complementary metal-oxide semiconductor) digital Rolera Bolt camera (QImaging,

Surrey, BC, Canada) or a near infrared charge-coupled device camera (JAI CV-M50IR). Tight seals ($>1\text{G}\Omega$) were formed and whole-cell access was achieved by brief negative pressure. Current clamp recordings were made with a Multi Clamp 700B amplifier (Axon Instruments). Built-in capacitance compensation and bridge balance circuitry was used to correct for and monitor series resistance throughout experiments. Recordings were sampled between 5-20 kHz using Clampex 10.0 (Axon Instruments).

Upon whole-cell access, cells were allowed to equilibrate for 2-5 minutes. Basic cellular properties were qualitatively measured in real time to test the presence of stellate cell electrophysiological signatures (Alonso and Llinas, 1989; Alonso and Klink, 1993; Dickson et al., 2000b) that were present in all cells recorded. Inclusion criteria included resting membrane potentials below -55 mV, input resistances below $120\text{M}\Omega$, a strong sag potential (sag ratio range=0.22-0.43, median sag ratio=0.37, calculated as in Heys and colleagues (2013), sMPOs, overshooting action potentials (above zero mV), cluster spiking, and series resistances $\leq 30\text{M}\Omega$. Cells displaying these properties were then used to investigate rebound spiking. In some cases, cells lacking these properties were investigated as a control (n=7). At resting membrane potential, 0.5 second square step currents ranging from -500 to 500 pA (25 pA increments) were delivered to cells in order to qualitatively visualize sag potentials and spiking behavior. All remaining *in vitro* stimuli were generated in MATLAB and exported for delivery by Clampex 10.0. To identify each cell's preferred input frequency, the Chirp function was used to create a 20 second sinusoidal input increasing linearly from 0 to 20 Hz, sampled at 20 kHz. The amplitude of the ZAP ranged between 10-100 pA in different cells to ensure subthreshold

responses at different holding potentials. The ZAP response was measured at different holding potentials (-70 mV to -55 mV), and the value (rounded to the nearest Hz) at -55 mV was taken as the primary frequency (see below for use of additional frequencies) of the sinusoid used to test rebound spiking. All rebound spiking protocols were run with cells held near spiking threshold.

The following sinusoidal inputs were all sampled at 5 kHz. First we measured spiking in the absence of rebound dynamics by delivering control “empty sinusoids” consisting of sinusoidal inputs with amplitudes of 50 pA and frequencies ranging from 1 to 12 Hz (1 Hz increments). For all other remaining protocols, synaptic inputs (inhibitory for rebound spiking, excitatory for control spiking) were superimposed on 50 pA sinusoids. Synaptic inputs (I_{syn}) were simulated using a double exponential of the form:

$$I_{syn} = e^{(-t/\tau_1)} - e^{(-t/\tau_2)} \quad (\text{eq. 3.1})$$

where τ_1 and τ_2 are the fast and slow time constants, respectively. For all protocols, $\tau_1 = 0.001$ ms and $\tau_2 = 0.005$ ms. Recording trials were 200 seconds long, containing seven, 20 second long epochs of sinusoid oscillations separated by 5 seconds of baseline current (DC) between each epoch, and 12.5 seconds of baseline DC current at the beginning and end of each trial. In standard protocols, the magnitude of the synaptic input was scaled to be twice the peak to peak amplitude of the sinusoidal input (100 pA) and synaptic inputs were placed such that each subsequent peak was $(17/16) \cdot 2 \cdot \pi$ radians after the previous input (resulting in cycling through a full range of possible phases with steps of $2 \cdot \pi / 16$). The standard protocol was run at the resonance frequency of a given cell as well as

frequencies ± 2 Hz from the resonance frequency. For normalized input protocols, we took the largest magnitude of current in the standard protocol (i.e. when inhibitory input occurred at the trough of the sinusoid) and scaled each hyperpolarizing input to that value. Therefore, regardless of phase, each input reached the same absolute current value in our normalized protocol (see Figure 3a2). “Randomized” input protocols were generated by placing the synaptic input of each baseline cycle on a random phase. Possible phases were limited to increments of $(2\pi/16)$, and were sampled such that there were an equal number of inputs at each phase. “Sparse” inputs were generated by placing stimulation replicating synaptic inputs on every other cycle of the baseline sinusoid. The synaptic input on every other sinusoid cycle was $(2\pi/16)$ radians later in phase than the previous input. “Magnitude” protocols, used synaptic inputs with amplitudes that were 1/2, 1/4, or 1/8 that of the standard input.

In a subset of cells ($n=6$), baseline recordings were performed followed by continuous bath perfusion of 10 μM ZD7288 (Tocris, Sigma). After ten minutes of drug wash, experiments were then repeated in order to assess the role of the h current in rebound spiking behavior. For all drug wash conditions, synaptic blockers (2 mM kynurenic acid, 100 μM picrotoxin) were used in both baseline and drug wash conditions.

3.2.3 Data analysis

Data for each run was exported from Clampex to MATLAB for analysis. Cells responded to ZAPs with the envelope of the amplitude of their membrane potential response reaching a peak where the input approached their resonant frequency. Resonant frequency was determined using techniques previously described (Erchova et al., 2004;

Shay et al., 2012) using MATLAB curve fitting routines. The impedance $[Z(f)]$ was taken as the ratio of the magnitude of the Fourier transform of the output (membrane voltage) to the magnitude of the Fourier transform of the input (ZAP and DC injection). The peak of the impedance curve, determined by MATLAB `lsqcurvefit` routine, was then taken as the resonance frequency. The reported voltage for each ZAP was determined as the average value before the chirp stimulus began.

Cell spiking responses to sinusoidal inputs were detected by sampling for periods of depolarized membrane potential with a peak height that reached positive values above 0 mV. The phase of a spike in reference to the baseline oscillation was determined based on the timing of the peak voltage of the spike. For all input signals except the empty sinusoid, preceding input phase was determined as the phase of synaptic input directly preceding the spike. In instances where more than one spike was elicited from a given input (i.e. in drug wash condition), only the first spike was included for analyses. The holding voltage for each epoch of a trial was determined as the mean voltage during the dead-space directly preceding the epoch, accounting for any drift in membrane potential between different sinusoid segments but not within segments. In order to determine the statistical properties of phase of spiking responses across the full data set, the mean resultant angle (MRA) and the mean resultant length (MRL) for inhibitory/excitatory current inputs and spiking output was determined for each cell and the population. The following equations were used to compute MRA and MRL respectively:

$$MRA = \arctan2(\text{imag}(\text{mean}(e^{i\theta})), \text{real}(\text{mean}(e^{i\theta}))) \quad (\text{eq. 3.2})$$

$$MRL = \text{abs}(\text{mean}(e^{i\theta})) \quad (\text{eq. 3.3})$$

where i is the imaginary constant, θ is an angular variable, $\arctan2$ is the four-quadrant arc tangent function, and $\text{imag}()$ and $\text{real}()$ represent the real and imaginary components of the complex exponential. All circular analyses and statistics were done using the CircStat toolbox (Berens, 2009) for MATLAB. Circular statistical tests included the parametric Watson Williams test for determining whether the mean directions of two or more groups are identical or not, and paired t -tests to determine significant differences between the MRL distributions of two groups.

3.2.4 Biophysical simulation methods

To demonstrate the role of rebound spiking in network dynamics, we tested single cell models of rebound spiking and incorporated these into network simulations. Single neuron models used the framework developed by Izhikevich (2007) with the following equations:

$$C\dot{v} = k(v - v_r)(v - v_t) - u + (I_b + I) \text{ if } v \geq v_{\text{peak}}, \text{ then, } v \leftarrow c, u \leftarrow u + d \text{ (eq. 3.4)}$$

$$\dot{u} = a\{b(v - v_r) - u\} \text{ (eq. 3.5)}$$

where v is the membrane potential, u is the current, I_b is the baseline holding current, I is the injected current, C is the membrane capacitance (pF), v_r is the resting membrane potential (mV), v_t is the threshold voltage, k is the fast activation current with a , the fast current and b , the slow current, v_{peak} is the maximum voltage of a spike, c is the reset voltage, and d is the reset current. Parameters were chosen to match previously published values (Izhikevich, 2007) used to replicate properties of stellate cell recordings in medial entorhinal cortex (Burton et al., 2008). For all simulations we used the following

parameter values: $I_b = 130$, $C = 200$, $v_r = -60$, $v_t = -45$, $k = 0.75$, $a = 0.01$, $b = 15$, $c = -50$, $d = 100$, and $v_{peak} = 100$. For single cell properties such as resonance frequency and sag potential, we injected (I , eq.3.4) the same ZAP and hyperpolarizing step currents as used in slice experiments. We also injected the same inhibitory synaptic inputs (I , eq. 3.4) used in slice experiments to investigate rebound spiking in the modeled cell. Data analysis of the output from single cell simulations was performed in the same manner as the analysis of *in vitro* recording data.

Finally, to analyze the potential role of the rebound spiking properties demonstrated in these experiments, we incorporated these rebound spiking properties into network simulations. Izhikevich neurons with the parameter values above were placed in a feedback inhibitory network and also received theta rhythmic sinusoidal input to model medial septum input (see Figure 3.8a,b). These network simulations demonstrate that rebound spiking could maintain network spiking activity and could allow systematic shifts in network spiking activity between different neurons that receive different phases of oscillatory input from medial septum (Hasselmo, 2013).

In this simulation of network properties, we simulated two independent populations of Izhikevich simulations of stellate cells with membrane potentials labelled with different subscripts v_{T1} and v_{T2} because they end up firing on opposite cycles of theta rhythm oscillations (T1 and T2). This firing on opposite cycles is consistent with data on theta cycle skipping in medial entorhinal cortex in which neurons fire on alternating cycles of network theta rhythm (Jeffery et al., 1995; Deshmukh et al., 2010; Brandon et al., 2013). The stellate cells each have their own internal dynamical variables u_{T1} and u_{T2}

that mediate rebound spiking. In addition, they interact with two sets of inhibitory interneurons i_{T1} and i_{T2} . In the model, the synaptic interaction with inhibitory interneurons is mediated by uniform connectivity strengths W_{is} for stellate input to interneurons and W_{si} for interneuron input to stellate cells. There are no direct synaptic connections between stellate cells in the model, consistent with physiological data from entorhinal cortex (Dhillon and Jones, 2000; Couey et al., 2013).

The network dynamics are described by the following equations:

$$dv_{T1}/dt = k(v_{T1} - v_r)(v_{T1} - v_t) - u_{T1} - W_{si}[i_{T2} > \eta] + I_{MS} \quad (eq. 3.6)$$

$$dv_{T1}/dt = a\{b(v_{T1} - v_r) - u_{T1}\} \quad (eq. 3.7)$$

$$dv_{T2}/dt = k(v_{T2} - v_r)(v_{T2} - v_t) - u_{T2} - W_{si}[i_{T1} > \eta] + I_{MS} \quad (eq. 3.8)$$

$$du_{T2}/dt = a\{b(v_{T2} - v_r) - u_{T2}\} \quad (eq. 3.9)$$

$$i_{T1} = \sum_{v_{T2}} W_{is}[v_{T2} > v_{peak}] - [i_{T1} > \eta] \quad (eq. 3.10)$$

$$(i_{T2} = \sum_{v_{T1}} W_{is}[v_{T1} > v_{peak}] - [i_{T2} > \eta]) \quad (eq. 3.11)$$

The membrane potential of each stellate cell is represented by v_{T1} for individual stellate cells in population $T1$, and v_{T2} in stellate population $T2$. The internal activation of the h-current in each stellate cell is simulated using the recovery variable u_{T1} in stellate cells in population $T1$ and u_{T2} in population $T2$. The stellate cells generate spiking output to interneurons at specific time steps (shown in square brackets), when $v > v_{peak}$ and v is reset to the value of parameter c , and u is reset to $u + d$.

The variable i represents the membrane potentials of interneurons, which also display discrete spiking output when they cross a threshold h . Spikes in the interneurons cause hyperpolarizing inhibitory feedback potentials in the same population of interneurons immediately after the spike. In addition, spikes in the interneurons cause

inhibitory synaptic potentials in the population of stellate cells with the opposite population index (e.g. i_{T1} inhibits v_{T2} and i_{T2} inhibits v_{T1}). The same uniform connection matrix W_{si} connects the inhibitory cells i_{T1} to all stellate cells in population v_{T2} , and connect the inhibitory cells i_{T2} to all stellate cells in population v_{T1} . All stellate cells in population v_{T1} send output to a single interneuron i_{T1} via matrix W_{is} that connects to the entire stellate cell population v_{T2} via the matrix W_{si} , and all stellate cells in population v_{T2} send output to a single interneuron i_{T2} via matrix W_{is} that connects to the entire stellate cell population v_{T1} via matrix W_{si} .

Each stellate cell also receives oscillatory input from the medial septum with different phases according to the equation: $I_{MS} = \mu \sin(2\pi ft + 2\pi(v_{T1}/n))$ (eq. 3.12), where f is the medial septal frequency, v_{T1} is the stellate cell index and “ n ” is the total number of stellate cells in the population. The same range of phases influence the stellate cells in population T2 as well. The initial activity in each simulation was activated by giving an initial hyperpolarizing input to specific stellate cells, causing a depolarizing rebound that generated a rebound spike that activated inhibitory interneurons and initiated further rebound spiking activity in the simulation.

3.3 Results

3.3.1 Confirmation of stellate cell type

The focus of this study was to analyze near threshold rebound spiking behavior elicited by sinusoidal inputs superimposed with inhibitory post-synaptic currents. The phases of hyperpolarizing inputs pulses that induced spikes and the output phases of these

spikes, relative to sinusoidal oscillations, were analyzed in 72 layer II stellate cells and 7 layer III non-stellate cells of the medial EC.

Figure 3.1a shows micrographs of a horizontal brain slice. Two magnifications show the cell's location within the medial EC superficial layers as well as morphological detail, revealing a large soma and dendrites radiating in all directions. These morphological characteristics are indicative of stellate cells (Alonso and Klink, 1993). Cells displayed a number of electrophysiological properties typical of stellate cells including sMPOs with amplitudes between 2-5 mV (Figure 3.1b1, inset), cluster spiking, defined by epochs of two or three successive spikes separated by sMPOs (Fig. 3.1b1, asterisks), subthreshold resonance frequencies in the theta range (3-8 Hz, Fig. 3.1d1), and a prominent sag potential in response to hyperpolarizing step currents coupled with rebound spiking upon release of the hyperpolarizing current (Fig. 3.1c, black trace). Upon application of 10 μ M ZD7288, a selective I_h blocker, the resting membrane potential gradually became hyperpolarized (Fig 3.1b2), and the cell ceased to show sMPOs (panels b3, inset), sag potential, rebound spiking (panel c, gray trace) and resonance (panel d2). Additionally, cluster spiking was replaced by a behavior described as cyclical transitions between low frequency firing and periods of inactivity (Fig. 3.1b3, note the scale of the time axis). In addition to the consistent observation of these basic electrophysiological properties, all 14 recovered cell fills (out of 72 recorded cells) had similar stellate-like morphologies. Furthermore we recorded 7 cells that lacked stellate-like electrophysiological properties and were able to recover cell fills in three of these cells. All three cells lacked stellate-like morphologies (data not shown). Similar to

previous articles (Alonso and Klink, 1993; Klink and Alonso, 1997), this supported the standard use of electrophysiological characteristics to classify cell types.

3.3.2 Phase specificity of rebound spiking

The basic rebound spiking effect observed in medial EC stellate cells is shown in Figure 3.2. Panels a1-a3 show an example of the standard input and spiking output at three different time scales. Figure 3.2 polar histograms show a quantitative analysis of the phases of hyperpolarizing input pulses inducing spikes and the output phases of spiking. Column b shows these analyses for the single epoch shown in a2, while column c shows analyses from all epochs of this representative cell. There are a number of important findings from these analyses. First, there is a limited range of hyperpolarizing input phases that caused spiking. Second, the phases of output spiking are narrow, despite the larger phase range of inhibitory synaptic inputs. Lastly, a comparison between phase histograms from a single epoch (b) and all epochs of this particular cell (c) demonstrates the consistency of the observed rebound spiking responses. To more easily visualize the phases at which hyperpolarizing inputs are able to induce spikes and at which phases spikes occurs (d) shows a population summary plot of these phase ranges relative to one cycle of the sinusoidal oscillation.

Our population data further demonstrate the consistency of phase effects and verify that these effects are due to intrinsic rebound spiking properties. Figure 3.3 presents current traces of the standard input, and control inputs consisting of the normalized, random, sparse, and excitatory synaptic inputs (a1-a5). Phase histograms depicting input phase (b1-b5), and output phase (c1-c5) analyses for the population of

cells recorded from each input type are to the right of each current trace. Our results indicate that stellate cells responded similarly to hyperpolarizing input pulses at different phases in different conditions (Fig. 3.3d-g). These similar responses to inhibitory input pulses indicate that rebound spiking behaviors were unaffected when synaptic inputs were constructed to have equal local minima at all input phases (a2), that the output spiking phases were not determined by the order of previous hyperpolarizing inputs (a3), nor were output spike phases determined by the timing of hyperpolarizing inputs on the preceding cycle (a4). However, in response to depolarizing inputs, the population of stellate cells had significantly lower input MRL (d), output MRL (e), and input MRA (f) compared to hyperpolarizing inputs (paired *t*-test, *, $p < 0.05$; ***, $p < 0.001$). This data suggest that stellate cells respond much differently to the phase of depolarizing inputs than to the phase of hyperpolarizing inputs. For excitatory inputs, the average input phase eliciting spikes occurs significantly earlier than for hyperpolarizing inputs (f), and the distribution of input phases that cause spiking is much wider compared to hyperpolarizing inputs (d). Furthermore, although the average spiking phase is similar (g), excitatory driven spiking occurs with a significantly broader phase distribution compared to inhibitory driven rebound spiking (e). Overall, our data suggest that rebound spiking was elicited within a smaller input phase window and that rebound spiking is produced in a more precise manner relative to oscillations than spikes produced by depolarizing input.

3.3.3 Oscillation frequency and phase analyses

Whereas data presented thus far have been shown for inputs containing sinusoid oscillations with a frequency close to the cell's depolarized resonance frequency, analyses from inputs with oscillations at +2 Hz and -2 Hz from cells' depolarized resonance frequencies are presented in figure 3.4. Both within cell and across cell analyses were done. Panels a-c show input phase and output phase for a representative cell with a depolarized resonance frequency of 5 Hz, whereas d-e show the same analyses for a representative cell with a depolarized resonance frequency of 3 Hz. The cells behaved similarly when inputs were delivered at their respective depolarized resonance frequency (compare b1-b2 with e1-e2) as well as when inputs were delivered at +2 Hz from their resonance frequency (compare a1-a2 with d1-d2). However, cells with resonance near 3 Hz receiving input oscillations at either 3 Hz or 5 Hz fired at later phases (higher MRA) compared to cells with a resonant frequency of 5 Hz (f, parametric Watson Williams test, ***, $p < 0.001$). This suggests that with a fixed frequency background oscillation, cells with lower resonant frequencies tend to fire at later phases compared to cells with higher resonant frequencies. However, preferred spiking phases for both cell populations converged at 7 Hz. The frequency dependence of rebound spiking phase is shown in our population data in Figure 3.4h-k. As the baseline oscillation frequency was increased beyond a cell's resonant frequency, the distribution of preferred inputs became significantly narrower (h, paired *t*-test, **, $p < 0.01$; ***, $p < 0.001$) and shifted to significantly earlier phases (j, parametric Watson Williams test, *, $p < 0.05$), while spiking phase shifted to significantly later phases (k, parametric Watson

Williams test, ***, $p < 0.001$). These data suggest that as the sinusoidal oscillation frequency increases relative to resonance frequency, the input phase window to produce a spike decreases in width and shifts to earlier phases, while the average output phase shifts to later phases. In addition, a higher intrinsic resonance frequency of a cell causes it to fire in response to earlier phases of input and generate output at earlier phases. Earlier phases of both input and output could influence the spacing of grid cell firing fields by causing more rapid transitions between firing fields as shown in Figure 3.8 below.

3.3.4 Magnitude of hyperpolarizing inputs and phase analyses

Figure 3.5 shows the effects on rebound spiking with changes in the magnitude of inhibitory synaptic inputs. Panels a1-a4 show hyperpolarizing inputs of full magnitude, half magnitude, quarter magnitude, and eighth magnitude, respectively. The resulting phase histograms for the cell population ($n=15$) are shown to the right of each current input in order of input phase (b1-b4) and output phase (c1-c4). As the magnitude of hyperpolarizing inputs was decreased, the input MRA slightly decreased (d, parametric Watson Williams test, 1/8 vs. 1/2 and 1/8 vs. 1, *, $p < 0.05$) while the MRA of spiking increased (e). In fact 1/8 and 1/4 magnitudes gave significantly larger output MRAs than 1/2 and full magnitude hyperpolarizing inputs (e, parametric Watson Williams test, $p < 0.001$). This data suggests that the strength of inhibition can change the rebound spiking phase in stellate cells, with stronger inhibition causing earlier spiking phase. This could allow larger inhibition magnitudes to cause faster transitions between firing fields of the sort shown in Figure 3.8 below.

3.3.5 Pharmacological blockade of HCN channels

We have shown, in Figure 3.1c, that pharmacological blockade of I_h abolishes rebound spiking to hyperpolarizing square current pulses. This finding prompted us to test whether blockade of I_h with 10 μ M ZD7288 would also alter the phase properties of rebound spiking in response to our sinusoidal inputs. Figure 3.6 shows the phases of the hyperpolarizing inputs inducing spikes (a1-c1) and output phases of spikes (a2-c2) for stellate cells (n=6) before (a1-a2) and after (b1-b2) drug application, as well as the non-stellate cell population (n=7, c1-c2). The summary bar graph in **d** shows the MRL of hyperpolarizing inputs significantly decreased following drug application (paired *t*-test, **, $p < 0.01$). Stellate cells in the baseline condition have significantly higher MRLs for hyperpolarizing input than non-stellates (paired *t*-test, *, $p < 0.05$) but following the drug condition, stellate cells did not significantly differ from non-stellate cells in the response to input phase. The phase specificity of spiking output is summarized by the bar graph in **e** and shows that the MRL of spiking in stellate cells under baseline conditions were significantly larger than non-stellates (paired *t*-test, **, $p < 0.01$), and was smaller but did not reach statistical significance after blocking I_h . That is, blockade of I_h reduced phase specificity of spiking output. Together these data suggest that I_h shapes the phase specificity in which hyperpolarizing inputs can elicit rebound spiking, but is likely to be only partially involved in regulating spiking output phase.

3.3.6 Single cell simulations of rebound spiking

Figure 3.7 shows simulated data from an Izhikevich (2007) neuron in which parameters were selected to produce behaviors similar to what we recorded *in vitro*.

Panel a1 shows a ZAP current input and the voltage output of a representative model cell showing resonance in the theta frequency band (4.425 Hz), while a2 shows the sag potential and post inhibitory rebound spikes (bottom) in response to hyperpolarizing square current steps (top). Similar to our experimental data, our simulated cells showed phase specificity to hyperpolarizing input and similar output spiking phases in response to the same sinusoidal inputs used *in vitro* (b-c). In response to increases in baseline oscillation frequency, the simulated cell shifted its output MRA to later phases (fig. 3.7 d2), similar to what we observed *in vitro* (Fig. 3.4 k). However, the MRA of the phase of hyperpolarizing inputs that caused spiking also shifted to later phases (Fig. 3.7 d1) for certain values, which was contrary to what was observed *in vitro* where hyperpolarizing input phases that caused spiking moved to earlier phases (Fig. 3.4 j). The reason for these differences is most likely due to the simplified parameter space of the Izhikevich cell model. Using a more detailed biophysical cell model may help to fully replicate the results observed *in vitro*. In response to decreases in the magnitude of hyperpolarizing inputs, our model cell behaved similarly to stellate cells; the MRA of hyperpolarizing inputs decreased (earlier phases elicited spikes, e1), while the MRA of spiking output increased (spiking output occurred at later phases, e2).

3.3.7 Network simulations of rebound spiking

The resonance and rebound spiking dynamics of simulated stellate cells shown above in Figure 3.7 are able to generate grid cell firing properties in a network model. The network connectivity is shown in Figure 3.8a, and depicts stellate cells receiving feed-forward oscillatory inputs from the medial septum, and feedback inhibition from

local interneurons. As described in the equations, the oscillatory input from the medial septum has different phases for different stellate cells, resulting in differential phase sensitivity to the timing of inhibitory synaptic input that influences the full population of stellate cells simultaneously. The result of different phases of medial septal input is that different neurons will spike in response to the same phase of hyperpolarizing synaptic input to the entire population. Only a subset of neurons will spike due to the timing of the hyperpolarizing input relative to the phase of medial septal input.

Note that this network lacks excitatory monosynaptic connections between stellate cells, and therefore stellate cells interact only via interneurons. Despite the presence of only inhibitory feedback between stellate cells, the network can maintain spiking activity in stellate cells as shown in Figure 3.8b. The network activity of a single cell pair without medial septum input is shown in Figure 3.8b. An inhibitory input causes a rebound spike in the first stellate cell (v_{T11}), which activates the first interneuron (i_{T11}) causing a rebound spike in the second stellate cell (v_{T21}). This rebound spike then generates a spike in the second interneuron (i_{T21}) and the cycle repeats itself. As shown here, the model generates spiking activity that occurs on alternate theta cycles in different stellate cells, accounting for theta cycle skipping observed *in vivo* (Brandon et al., 2013).

Constructing a network model consisting of multiple cell pairs and providing each with oscillatory medial septal inputs differing in phase, results in spiking output dependent on the difference between the time of the oscillation period and the speed of rebound spiking. This network behavior can be seen in Figure 3.8c. Periodic firing of individual stellate cells occurs at different times throughout the run due to the timing of

the feedback inhibitory input from interneurons going to all stellate cells in a population that only generates spiking when it interacts with a specific range of phases of oscillatory medial septum input to individual stellate cells.

For example, consider the stellate cell in the bottom row (v_{T11}). This cell starts out inactive because the hyperpolarizing input, due to spiking of the inhibitory interneuron, arrives at a time that does not cause a rebound spike. However, the input of this same interneuron to other stellate cells (e.g. v_{T14}) arrives at the correct phase relative to medial septum input and causes rebound spiking. Note that the time between the interneuron spike and a stellate cell rebound spike is slightly shorter than the wavelength of medial septum input. As each rebound spike occurs earlier in phase relative to medial septal input, it causes interneuron spiking at an earlier phase. Eventually, the phase of interneuron spiking comes early enough to fall within the range of input phases that evoke rebound spiking in v_{T11} , causing it to start spiking. The rebound of this cell is slightly faster than the period of the medial septal input, so each spike comes at a slightly earlier phase on each cycle of medial septal input, causing slightly earlier spiking of the interneuron until eventually the interneuron input comes too early in phase and falls out of the range of phases that induce rebound spiking in v_{T11} . This demonstrates how the rebound spiking properties of the cell could allow spiking in a delimited period of time due to both the limited range of input phases inducing rebound spikes and the timing of output spikes relative to the wavelength of medial septal input.

Looking at a portion of a single stellate cell's spiking output (3.8d) one can see how spiking phase precesses (3.8e) relative to network theta rhythm as the animal moves

through a firing field. Plotting spiking output along the spatial domain, periodic firing fields along the linear track are observed (3.8f) similar to grid cell firing as a rat runs on a linear track. As shown in Figure 3.5, the amplitude of inhibitory input determines the speed of rebound spiking. For weak inhibitory input, the speed of rebound spiking could match the period of medial septal input, allowing the firing to remain in one cell, whereas stronger inhibitory input could cause faster rebound spiking and a more rapid shift between cells in the population (Hasselmo, 2013). In this manner, if the running speed of the rat determines the magnitude of feedback inhibition, the velocity of the running could determine the rate of transition between neurons firing in different firing fields. The influence of running speed on transitions between neurons corresponds to a mechanism for integration of velocity into the individual neurons that fire. This would allow firing of grid cells that is driven by the running velocity of the rat, as in many models of grid cells (Burgess et al., 2007; Burgess, 2008; Hasselmo, 2008; Blair et al., 2008).

3.4 Discussion

3.4.1 Summary of findings

The physiological results presented here show a characterization of rebound spiking in response to realistic inhibitory post synaptic currents in stellate cells of the medial EC. Inhibitory synaptic inputs were superimposed on fixed frequency sinusoidal inputs in order to simulate an idealized theta rhythm observed *in vivo*. Our method reveals a specific range of phases of hyperpolarizing inputs that cause spiking and these output spikes occur at a restricted phase range. The phase specificity of inputs that elicit

spikes is dependent on the presence of I_h as blocking the I_h with 10 μ M ZD7288 abolished the phase specificity in response to hyperpolarizing input pulses. The ability of I_h to limit the input phases causing spikes is important, as this allows the periodic firing fields in the model presented here. The narrow phase range of output spiking is consistent with *in vivo* data in which spiking in layer II EC is limited to a narrow phase range of the theta oscillation (Quilichini et al., 2010). However, in contrast to the dependence of input phase on I_h , the consistent output spiking phase range we observed does not appear to be dependent on the I_h as spiking phases of cells were consistent in non-stellate cells as well as in stellate cells before and after drug application. This similarity is likely due to the output phase of spiking activity being regulated by the interaction of currents activated by depolarization with the peak of the sinusoid oscillation.

3.4.2 Relationship to previous *in vitro* data

A previous slice physiology study has shown that depending on the phase an inhibitory synaptic input is delivered during a 5 Hz oscillation, it is able to delay or advance the timing of repetitive spiking activity in CA1 pyramidal cells (Kwag and Paulsen, 2009). This spike time advancement is dependent on the I_h as it is abolished by ZD7288. While this study was not studying rebound spiking per se, there are important similarities to our study. Kwag and Paulsen were recording from cells containing I_h , they were holding these cells close to threshold, and they were delivering theta oscillations, as well as inhibitory inputs. Both studies found that I_h interacted with both the oscillations and inhibition to dynamically change, in our case the inhibitory input phase causing

spiking, and in their case the phase of repetitive spiking output induced by the sinusoidal input. Whether a similar phenomenon exists in medial EC stellate cells was out of the scope of our project, but is an intriguing question.

3.4.3 Relationship to *in vivo* recording data

In vivo extracellular recordings have shown post inhibitory rebound spiking in the medial entorhinal cortex in the anesthetized rat (Adhikari et al., 2012). In this study, rebound spiking occurred more readily during the theta rhythm, and all cells displaying rebound spiking during the theta state only (not the slow oscillation state) were located in layers II and III. Rebound spiking was more prevalent between pairs of interneurons (n=21 out of 46) compared to principal cells (n=5 out of 49). For interneurons to show rebound spiking it is likely that ionic currents, such as I_h , are present in these cells. A greater understanding of the intrinsic properties of medial entorhinal interneurons will be valuable for further interpretation of these results. The low percentage of principal cells displaying rebound spiking in that study could be due to the experimental conditions of anesthesia. Furthermore, it is not clear if stellate cells were recorded as the authors did not differentiate between stellate cells and pyramidal cells.

In vivo intracellular recordings in the medial EC have shown ramp depolarizations and sMPOs in stellate cells during traversals through grid firing fields (Domnisoru et al., 2013; Schmidt-Haiber and Häusser 2013). Although ramp depolarizations drive spiking (Domnisoru et al., 2013; Schmidt-Haiber and Häusser), spikes occur preferentially at the peaks of theta oscillations (Domnisoru et al., 2013). These data are consistent with our rebound spiking data. Stellate cells had to be sufficiently depolarized in order to display

rebound spiking and rebound spikes occurred near the peak of the theta oscillation. *In vivo* intracellular recordings of fast spiking putative interneurons show increased firing rates during running (Schmidt-Haiber and Häusser, 2013). Therefore it is possible that spiking activity from interneurons could interact with stellate cells to generate rebound spiking. When a stellate cell's membrane potential is shifted closer to threshold via depolarizing ramps, a cell's sMPOs could integrate inhibitory inputs causing rebound spikes. As we have shown, this rebound spiking mechanism can account for phase precession and can therefore support temporal codes similar to oscillatory interference models. Future *in vivo* work will be crucial to identifying what cell types contribute to the movement dependent sMPOs and ramp depolarizations as well as to whether or not interneurons can cause rebound spiking in medial EC stellate cells.

3.4.4 Relationship to the resonance frequency of different neurons

Our data show that differences in the resonance frequency of different neurons results in differences in the phase of rebound spiking for different sinusoidal input frequencies. For example, a neuron with a resonance frequency of 3 Hz will respond differently during a sinusoidal input at 5 Hz compared to a neuron with a resonance frequency of 5 Hz (Figure 3.4). The difference in rebound spiking phase for different resonance frequencies could contribute to the difference in spacing of grid cell firing observed for neurons recorded at different D/V positions of entorhinal cortex (Hafting et al., 2005; Stensola et al., 2012) based on the difference in resonance frequency observed in neurons in slice preparations at different D/V positions (Giocomo et al., 2007; Giocomo and Hasselmo, 2009; Boehlen et al., 2010).

In the computational model, the periodic firing behavior of stellate cells relies on the difference between the period of the theta oscillation and the timing of the induction of rebound spiking. The resulting constraint on neural activity due to this interaction is analogous to the beat pattern in oscillatory interference models (Burgess, 2008), in that it determines the grid cell firing field size and spacing, and determines the slope of theta phase precession observed *in vivo* (Hafting et al., 2008; Kjelstrup et al., 2008; Climer et al., 2013; Hasselmo, 2013). Our model therefore hypothesizes that small firing fields and spacing will result when a cell shows rebound spikes with shorter delays for a given input, while large firing fields and spacing will result from longer delays in rebound spiking. Our across cell frequency analysis (Fig. 3.4f-g) serves as a means to test this hypothesis. We found that for a given oscillation frequency cells with lower resonance frequencies spiked at later phases (longer delay) than cells with higher resonance frequencies. This longer delay with lower resonance frequency would result in wider spacing between wider firing fields in the model, consistent with wider fields in ventral EC (Hafting et al., 2005) where lower resonance frequencies are observed (Giocomo et al., 2007).

On a related note, HCN1 knockout mice show an expansion of grid cell firing fields and spacing along the D/V axis of mEC (Giocomo et al., 2011). These results have significance in the context of our findings. We have found that with complete blockade of I_h , hyperpolarizing inputs lose the ability to cause rebound spiking in a phase specific manner. The absence of the HCN1 subunit doesn't completely abolish I_h in stellate cells, but decreases the fast time constant, the sag potential, and the resonance frequency

(Giocomo and Hasselmo, 2009). Therefore, a possible explanation for the increases in grid cell firing fields and spacing observed in HCN1 knockout mice *in vivo* could be a slower speed (longer delay) of rebound spiking.

Our data show a convergence of the mean output spiking phase as the baseline oscillation increases to 7 Hz. Our previous study showed that as a stellate cell's membrane potential was hyperpolarized its resonance frequency asymptotically approached a maximum frequency of approximately 7 Hz (Shay et al., 2012). That both cell properties have a saturation point suggests a similar cellular mechanism. It is likely that I_h regulates the integration of the sinusoid and inhibitory input, and at a critical frequency I_h is no longer able to keep pace with the oscillation and therefore the resonance frequency and average spiking phase reach a maximum value.

3.4.5 Significance of magnitudes of hyperpolarization

We found that the phase of rebound spiking can also change systematically with magnitude of hyperpolarizing input pulses (Fig. 3.5). This provides a potential mechanism for representation of velocity, as the shortening of rebound spiking corresponds to a higher frequency of a velocity-controlled oscillator in an oscillatory interference model of grid cells (Burgess et al., 2007; Burgess, 2008; Hasselmo, 2008; Blair et al., 2008; Bush and Burgess, 2014). This property is required to allow trajectories with different running speeds to generate firing in spatially consistent locations. If the rat runs more rapidly through firing fields, then larger feedback inhibition could allow faster rebound spikes that would result in a faster transition of

spiking between different firing fields. Accordingly, medial EC PV interneurons show increased firing rates with increased running speed (Buetfering et al., 2014).

Our *in vitro* and modeling data show that as the magnitude of hyperpolarizing input pulses decreases, output spiking phase becomes later, suggesting that the number and or strength of inhibitory synapses onto a stellate cell can contribute to its spiking phase. In addition to allowing regulation dependent on velocity, this could also contribute to the D/V difference in spacing of grid cell firing fields. Dorsal stellate cells receive a greater number of and more widespread inhibitory contacts than ventral cells and the majority of this inhibition is from somatic targeting interneurons expressing PV (Beed et al., 2013). Our data and model indicate that the interaction between PV interneurons and stellate cells could contribute to the spacing of grid cell firing fields through rebound spiking properties.

3.4.6 Relationship of model to MSDB-medial EC anatomical connectivity

GABAergic neurons of the MSDB have been proposed to be at least partly responsible for generating theta (Stewart and Fox, 1990). The majority of MSDB inhibitory neurons express PV and selectively project to interneurons of the hippocampus (Freund and Antal, 1988; Freund, 1989). Anterograde and retrograde tracing studies (Alonso and Köhler, 1984) have shown the EC receives anatomically specific inputs from the MSDB; inputs to medial EC tend to come from the most medial portions of the MSDB, where the most dense MSDB PV cell population is located (Alonso et al., 1990; Kiss et al., 1990). Recently it has been shown that optogenetic stimulation of axons of GABAergic medial septal cells causes monosynaptic IPSPs in over 60% of medial EC

interneurons (Gonzalez-Sulser et al., 2014). The study distinguished interneuron subtypes through fast spiking and low-threshold spiking behaviors. However it is unclear how many different interneuron subtypes were targeted by medial septal GABAergic projections, and the connectivity of these interneurons with other medial EC cells is not known. Our model uses direct medial septal theta inputs to stellate cells as a simplification, but this is not intended to represent the primary influence of medial septum. Instead, this is meant to represent the effect of septal input synapsing on and reorganizing rhythmic activity of a population(s) of interneurons distinct from those receiving input from stellate cells shown in Figure 3.8. Furthermore, our model is able to work with the medial septal theta input synapsing onto either the stellate cells or the medial EC interneurons in Figure 3.8 (these simulations are not shown).

We have simulated theta skipping and grid cell firing behavior by selecting parameters of the Izhikevich neuron that match cellular properties found *in vitro*. Our model consists of stellate cells possessing resonance and rebound spiking properties embedded in an inhibitory network. When medial septal theta rhythmic input is delivered to stellate cells they generate grid cell firing activity. Loss of this medial septal subthreshold oscillatory input in the model results in the loss of spatially specific firing (Hasselmo, 2013). The network architecture used in this model therefore accounts for the loss of grid cell spatial periodicity shown experimentally with inactivation of the medial septum (Brandon et al., 2011; Koenig et al., 2011).

3.4.7 Significance to other grid cell models

The interaction of hyperpolarizing input pulses and sinusoidal input in our experimental data is analogous to the interaction of feedback inhibition and medial septum oscillatory input used in our model in which rebound spiking causes periodic firing of different entorhinal neurons. This interaction of the speed of rebound spiking with the period of medial septal input is analogous to the interaction of different oscillations used in the oscillatory interference model of grid cells (Burgess et al., 2007; Burgess, 2008; Hasselmo, 2008; Blair et al., 2008; Bush and Burgess, 2014). The oscillatory input at different phases arising from the medial septum could be generated by a mechanism such as the ring attractor network proposed in previous papers (Blair et al., 2007) that was proposed to involve neurons in a ring that sequentially activate each other at different phases. The ring attractor could provide a stable baseline frequency as in the simulation presented here. Alternately, the ring attractor could provide a medial septal input that changes frequency relative to a stable period of rebound spiking, allowing differential phase interactions dependent upon running speed. Cells of the medial septum show firing rates dependent on the animal's running speed (King et al., 1998) as well as cosine directional tuning of theta burst frequencies (Welday et al., 2011), suggesting that both running speed and direction coding are present in the medial septum. This provides another possible way of representing running velocity in a network model.

3.5 Figures

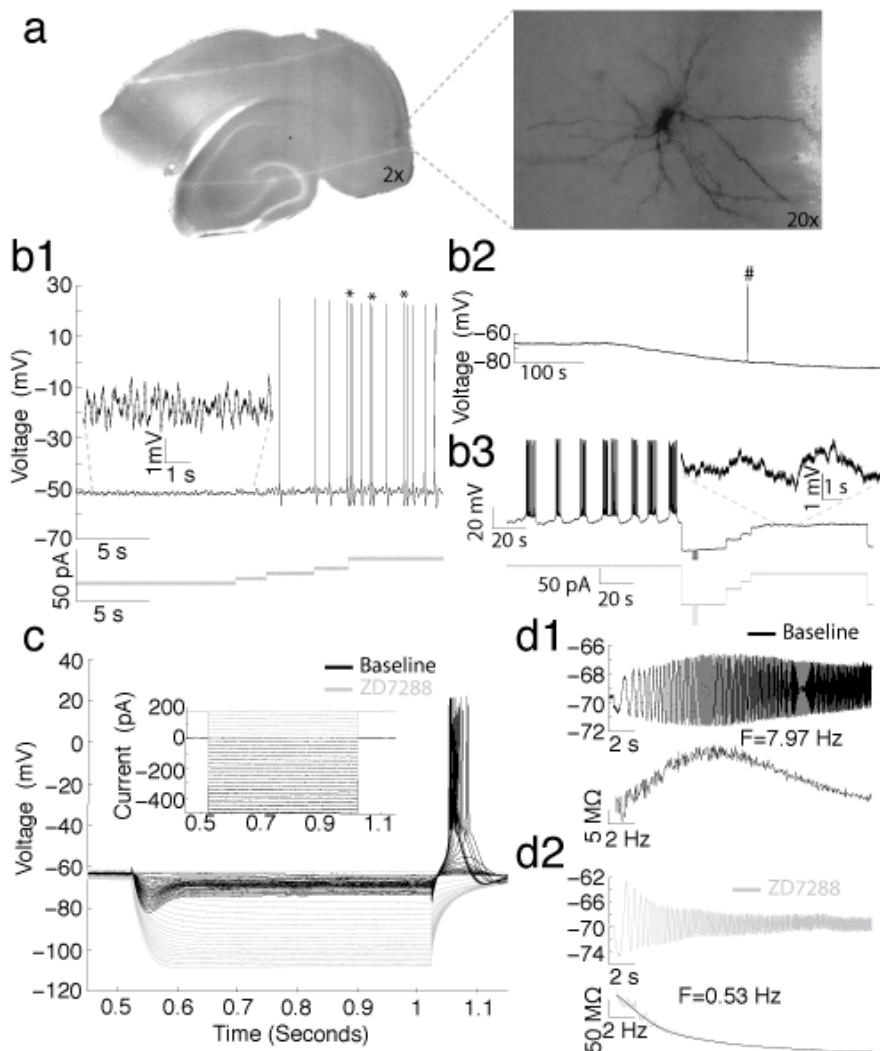


Figure 3.1 Intrinsic electrophysiological properties of stellate cells and loss of these properties with the h current blocker ZD7288

(a) Photomicrographs display a representative cell's anatomical location within the slice (left) as well as the typical stellate cell morphology (right). All data shown in **b-d** were recorded from this cell. (b1) This panel shows representative examples of electrophysiological properties of stellate cells including sMPOs (left) and spike clustering behavior (marked by asterisks on right). (b2) Bath application of ZD7288 consistently causes a gradual hyperpolarization in membrane potential (note holding potential is at 0 pA; #, spontaneous spike truncated). (b3) In ZD7288, spiking behavior shows cyclical transitions of low frequency spiking and inactivity after drug wash. The inset in **b3** shows that sMPOs are lost compared to inset in **b1**. (c) Voltage sag and rebound spiking are abolished by drug wash (compare black and gray responses). (d) Following drug application, resonant frequency changes, in this particular cell, from 7.97 Hz (**d1**, black) to 0.53 Hz (**d2**, gray).

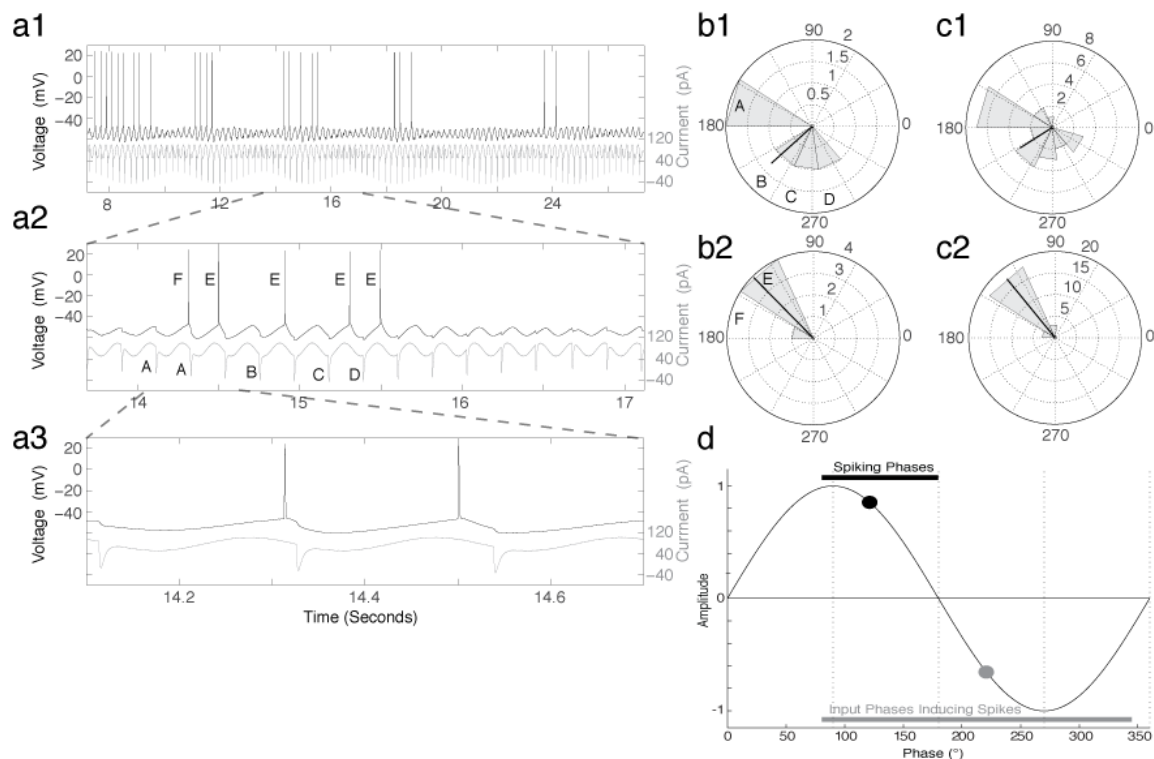


Figure 3.2 Stellate cells display rebound spiking in response to a limited range of phases of hyperpolarizing input pulses and with a limited range of output spiking phases

(a) An example stellate cell response (top, black) to the standard input (bottom, gray) is shown at three time scales (**a1**, **a2** and **a3**) to demonstrate rebound spiking behavior. (b) Rose plots correspond to the data in **a2** and show the phases, relative to the baseline oscillation, of hyperpolarizing input pulses that induce spiking (**b1**) and the phases of output spiking (**b2**). The black line in each rose plot is the MRA, and the length of the line is indicative of the MRL of the phase distribution. Uppercase letters in **b1** and **b2** correspond to those in **a2** and show what phase bin each hyperpolarizing input pulse (A-D) or output spike (E-F) falls into for each corresponding rose plot. **c**. Rose plots show the same input and output phase analyses as in **b1-b2** but correspond to all data collected in response to the standard input for this representative cell. (d) Population summary plot showing phases of the sinusoidal oscillation where hyperpolarizing inputs are able to induce spikes (gray) and phases where rebound spikes occur (black).

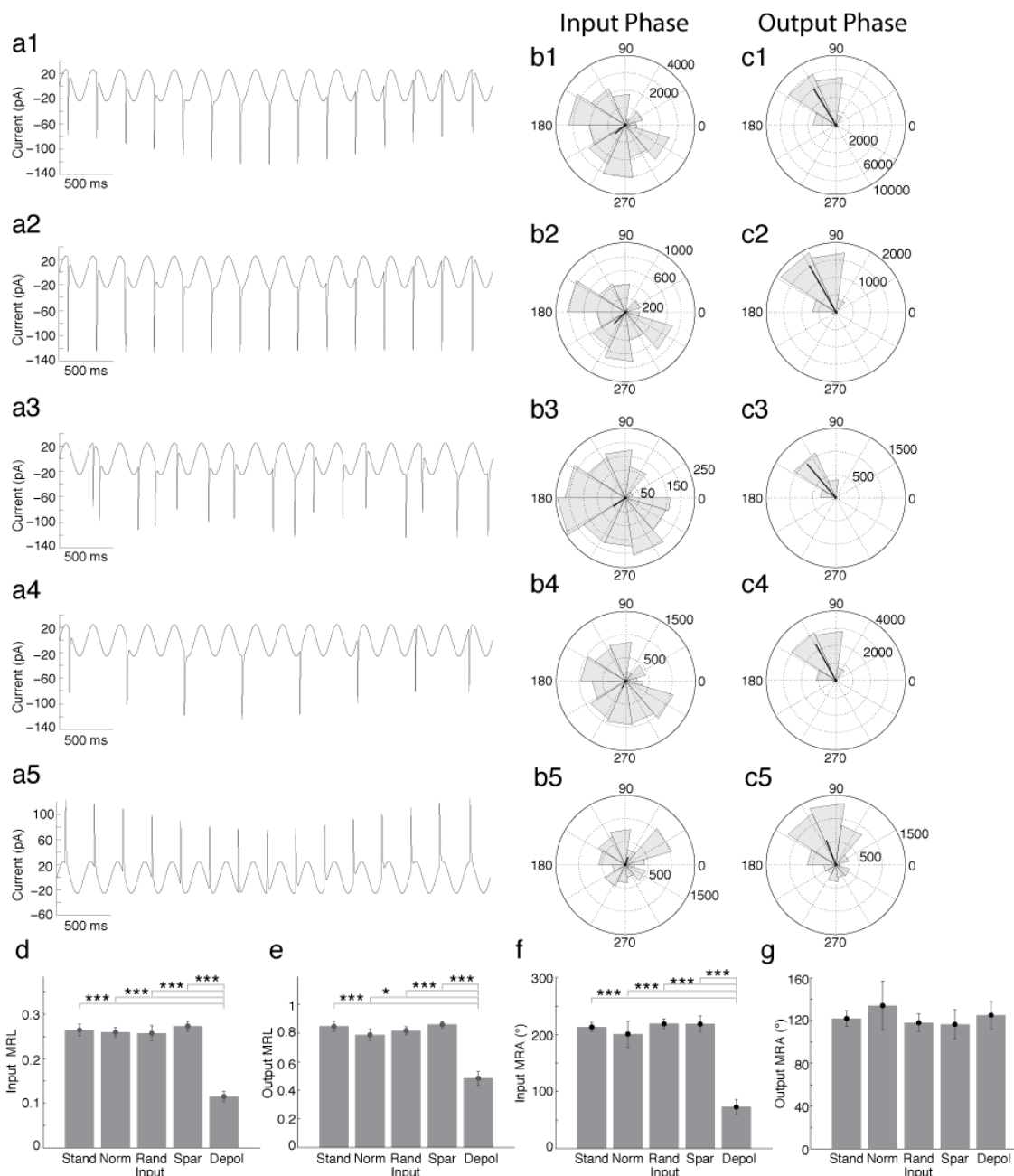


Figure 3.3 Hyperpolarizing and depolarizing input pulses have differential preferred input phases that induce spiking

(a) Control current inputs used are shown in the first column. These include (a1) standard, (a2) normalized, (a3) random, (a4) sparse, and (a5) depolarizing current inputs, respectively. (b-d) Rose plots show phase histograms for hyperpolarizing (a1-a4) or depolarizing (a5) input pulses that induce output spiking (b1-b5) and for the phase of spiking (c1-c5) for the entire population ($n=72$) of cells. Rose plots correspond to a

given input with matching numerical labels in each row. **(d-e)** Bar graphs show input **(d)** and output **(e)** MRLs do not differ between hyperpolarizing inputs, but are significantly larger than input and output MRLs in response to depolarizing inputs (paired *t*-test, *, $p < 0.05$; ***, $p < 0.001$). **(f-g)** Bar graphs show input MRAs **(f)** do not differ between hyperpolarizing input pulses, but are significantly larger than depolarizing inputs (paired *t*-test, ***, $p < 0.001$), while all output MRAs are similar **(g)**. Abbreviations in **d-g** are as follow: Stand=standard input, Norm=normalized input, Rand=random input, Spar=Sparse input, and Depol=depolarizing input.

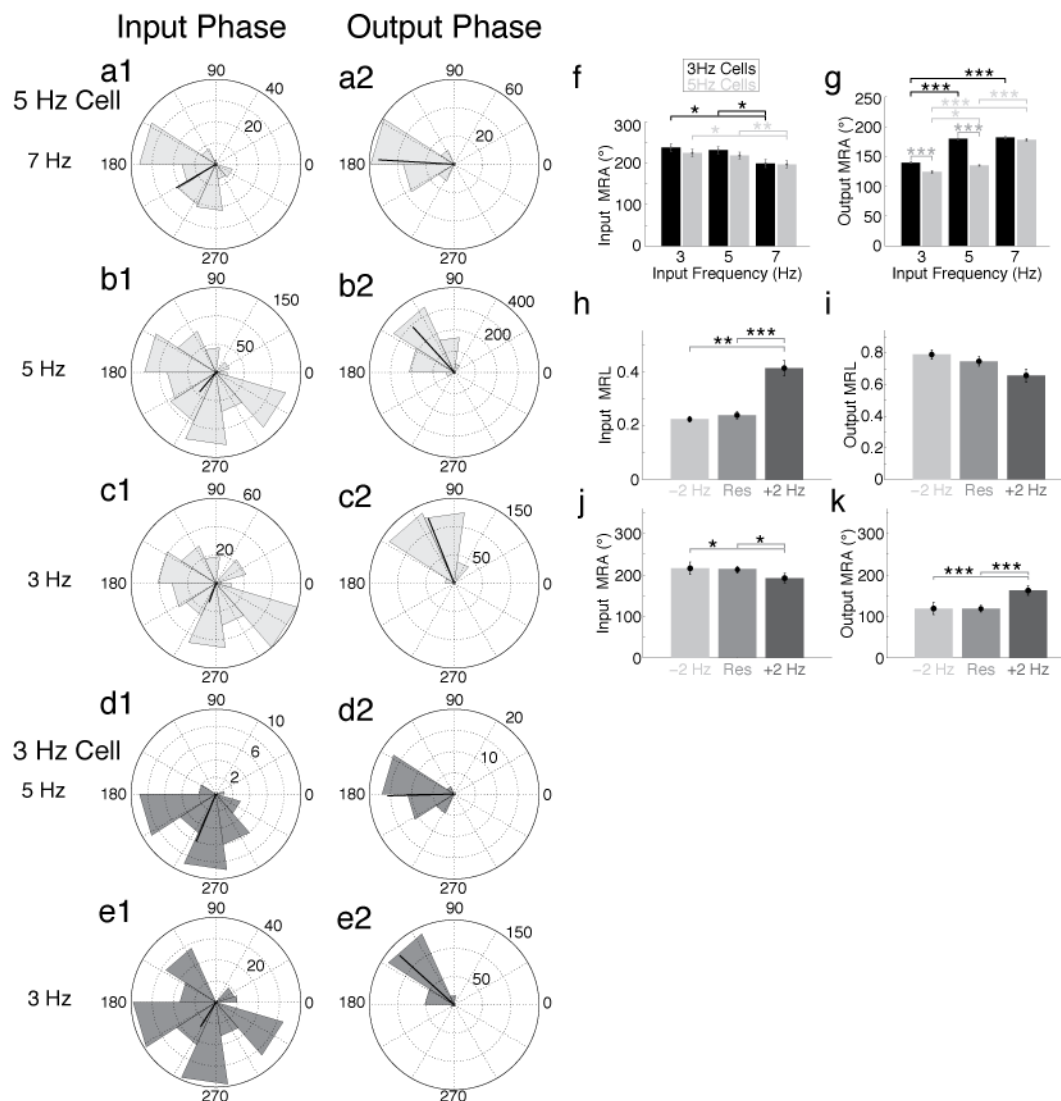


Figure 3.4 Preferred inhibitory input and spiking phases correlate with increased relative input frequency

(a-e) Rose plots display data from cells with a depolarized resonant frequency of 5 Hz (a-c, light gray) and 3 Hz (d, e, dark gray). Hyperpolarizing input pulse phase (a1, b1, c1, d1, e1) and output spiking phase (a2, b2, c2, d2, e2) analyses from standard inputs of 7 Hz (a1-a3), 5 Hz (b1-b3, d1-d3), and 3 Hz (c1-c3, e1-e3) are shown in each row. Note that cells behave similarly at their depolarized resonant frequencies (compare b1-b3 with e1-e3, respectively), as well as at +2 Hz from their depolarized resonant frequency (compare a1-a3 with d1-d3, respectively). (f-g) Summary bar graphs compare input MRA (f) and output MRA (g) for populations of cells with 3 Hz (black) and 5 Hz (gray) resonant frequencies. (f) There were no significant differences between the two populations of cells at all tested input frequencies. However within each population,

significant decreases (parametric Watson Williams test, *, $p < 0.05$; **, $p < 0.01$) in input MRA occurred between 3 Hz and 7 Hz as well as 5 Hz and 7 Hz input oscillations. **(g)** At 3 and 5 Hz baseline oscillation frequencies the 3 Hz resonant frequency cell population had significantly higher output MRA (parametric Watson Williams test, ***, $p < 0.001$), indicating a later average spiking phase, compared to the 5 Hz cell population. However, At 7 Hz there was no significant difference in output MRA. Within population analyses show significant increases in output MRA as oscillation frequency was increased for the 3 Hz (parametric Watson Williams test, 3 Hz vs. 5 Hz and 5 Hz vs. 7 Hz, ***, $p < 0.001$) and the 5 Hz population (parametric Watson Williams test, 3 Hz vs. 5 Hz, *, $p < 0.05$; 3 Hz vs. 7 Hz and 5 Hz vs. 7 Hz, ***, $p < 0.001$). **(h-i)** Population data of MRLs of inhibitory inputs and outputs. There are significant increases in MRL of spike inducing inputs **(h)** between inputs at a cell's resonant frequency and at +2 Hz the resonant frequency (paired, ***, $p < 0.001$), as well as -2 Hz the resonant frequency (paired *t*-test, **, $p < 0.01$). **(i)** The mean resultant length of output spiking displays an inverse trend with frequency but fails to reach statistical significance. **(j-k)** Population MRAs of inhibitory inputs causing spikes and output spiking as a function of relative input frequency. As the input frequency was increased beyond a cell's resonance frequency significantly earlier input phases were preferred **(j)**, parametric Watson Williams test, *, $p < 0.05$) and cells spiked at significantly later phases **(k)**, parametric Watson Williams test, ***, $p < 0.001$).

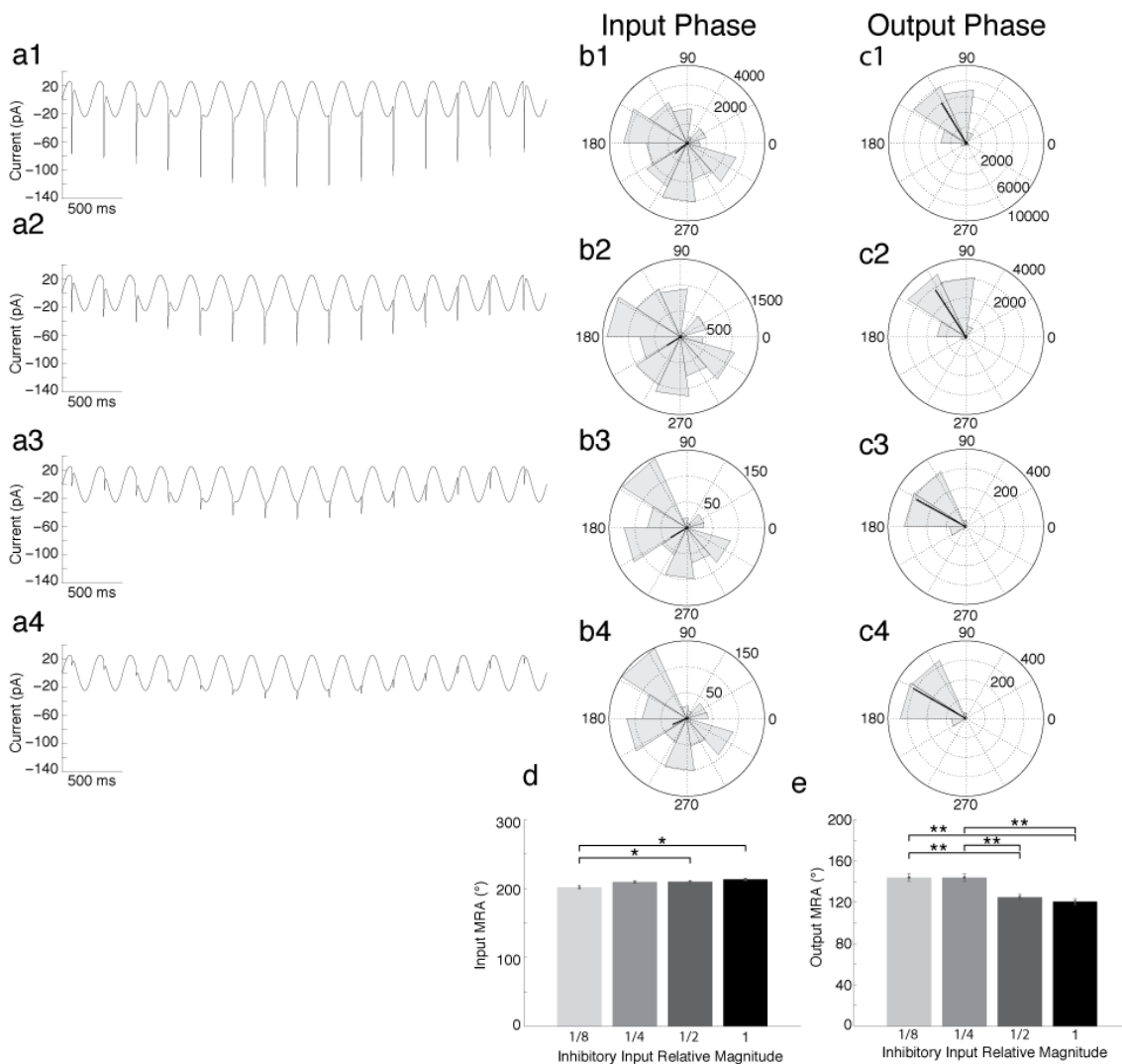


Figure 3.5 Decreasing magnitude of inhibitory synaptic input correlates with later spiking output phase

(a) Standard input currents are shown with decreases in the magnitude of hyperpolarizing synaptic input pulses from full magnitude (a1), to half magnitude (a2), quarter magnitude (a3), and eighth magnitude (a4). (b-c) Rose plots show population ($n=15$ cells) phase histograms for hyperpolarizing input pulses that induce spiking (b1-b4) and for output spiking phase (c1-c4). Rose plots correspond to a given magnitude input with matching numerical labels in each row. (d-e) Population bar graphs show that as the magnitude of inhibitory input decreases there is a small but significant decrease in input MRA between 1/8 and 1/2 as well as 1/8 and full magnitude inputs (d, parametric Watson Williams test, *, $p<0.05$), while the output (spiking) MRA is significantly larger (later phase) for 1/8 and 1/4, than for 1/2 and full magnitudes (e, parametric Watson Williams test, **, $p<0.01$).

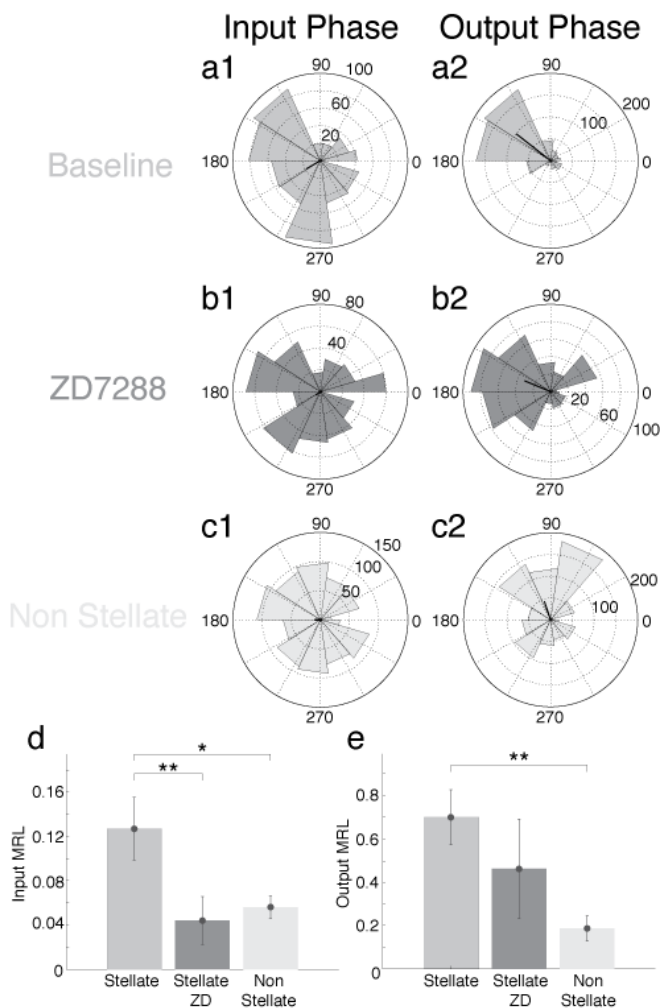


Figure 3.6 I_h is necessary for phase specificity of hyperpolarization induced rebound spiking

(a-c) Rose plots for standard inputs in stellate cells ($n=6$) before (a) and after (b) application of ZD7288 as well as in non-stellate cells ($n=7$, c). Rose plots display phase histograms for hyperpolarizing input pulses that induce spiking (a1, b1, c1) and for output spiking phase (a2, b2, c2). (d) Summary bar graph demonstrates that following H-current blockade, stellate cells lose the phase specificity for hyperpolarizing input, as indicated by a significant decrease in hyperpolarizing input MRL (paired t -test, **, $p<0.01$). Furthermore, this significant lack of input specificity is also present in non-stellate cells compared to baseline stellate cells (paired t -test, *, $p<0.05$). (e) Summary bar graph demonstrates that blocking the H-current in stellate cells decreases the specificity of output spiking phase, shown by a decrease in the MRL of output spiking phase, but this does not reach statistical significance. However compared to stellate cells, non-stellate cells display a significantly smaller MRL (paired t -test, **, $p<0.01$), and therefore, less phase specificity of output spiking.

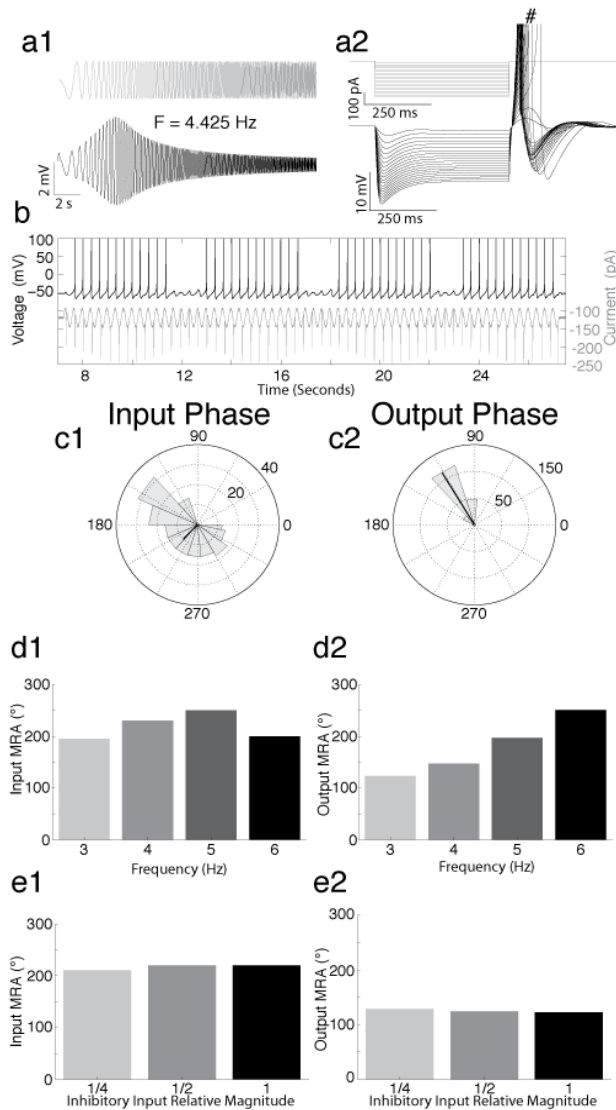


Figure 3.7 Izhikevich neuron possesses similar intrinsic and rebound spiking properties as stellate cells

(a) In response to a ZAP stimulus (a1, top) the model cell has a depolarized resonance frequency of 4.425 Hz. In response to hyperpolarizing square current steps (a2) the model cell displays a prominent sag potential and upon release of the current step, fires rebound spikes (a2, # denotes truncated spikes). (b) When the model cell receives hyperpolarizing synaptic input pulses superimposed on a sinusoid, the cell spikes to a subset of phases of hyperpolarizing input pulses. (c) Rose plots show the phase of hyperpolarizing input pulses inducing spikes (c1) and the phase of output spiking (c2). (d-e) Summary bar graphs show how increasing the baseline oscillation frequency (d) and the magnitude of inhibitory inputs (e) affect the input MRA (d1, e1) and output MRA (d2, e2).

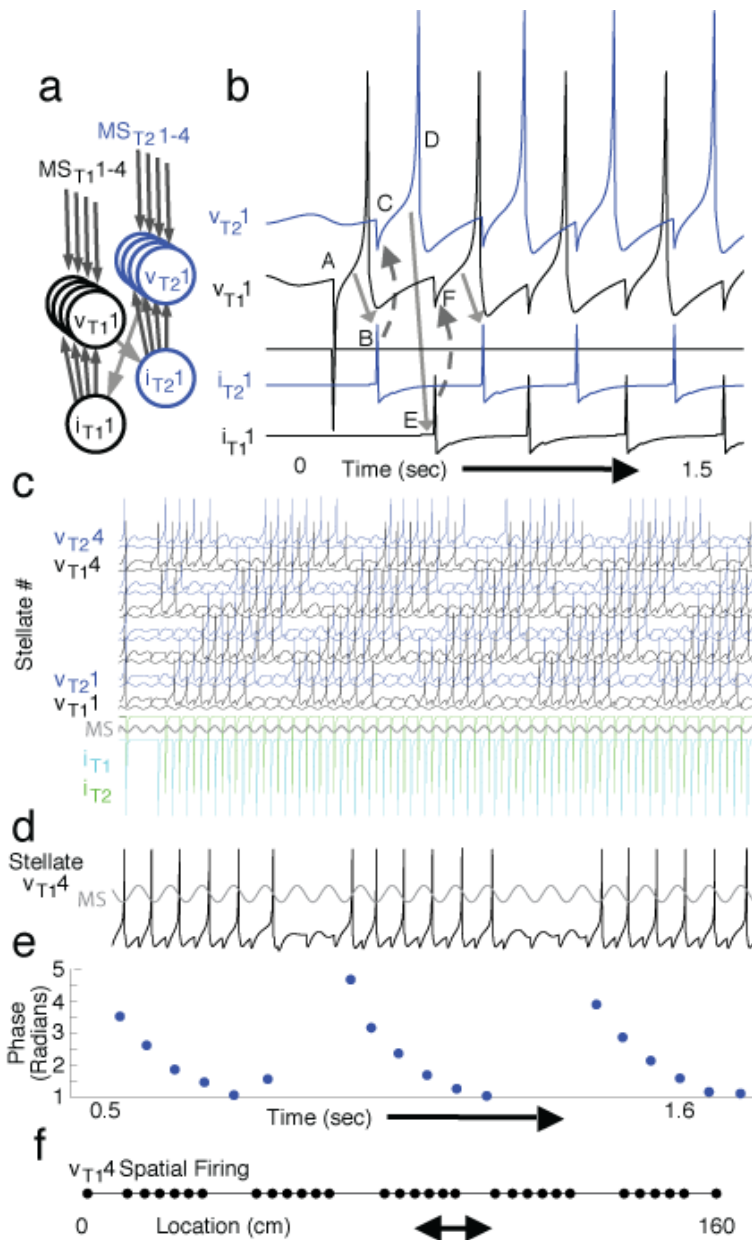


Figure 3.8 A model with stellate cells, possessing resonance and rebound spiking properties, embedded in an inhibitory network creates theta skipping and grid cell firing patterns on a linear track

(a) Our model uses medial septum (MS) input to stellate cells (v) that interact via interneurons (i) that cause feedback inhibition. (b) Inhibition causes rebound spiking (A) in a stellate cell (v_{T11}) on the first cycle of theta cycle skipping that activates an interneuron (B) which inhibits (C) another stellate cell (v_{T21}) causing a rebound spike (D) that activates another interneuron (E) that activates the first stellate cell (v_{T11} , F). This process is repeated, resulting in cyclical activity of stellate cells on alternating cycles. (c)

In this model, stellate cells get medial septum oscillatory input with different phases. Each cell's membrane potential is shown with a thick line, and below it the thin line shows medial septum oscillatory input. If rebound spiking (e.g. v_{T11}) is faster than the period of medial septum input, then feedback inhibition (i_{T21}) slowly shifts spiking to cells with earlier phases (e.g. v_{T22}). **(d-f)** Looking at a portion of a single cell's activity in relation to its medial septum oscillation **(d)** shows spiking shifts to earlier phases over time. This theta phase precession is depicted quantitatively in **e**. Plotting spiking in relation to the animal's location as it runs the linear track shows periodic spatial firing resembling grid cell activity **(f)**.

**CHAPTER 4: Cholinergic modulation of ADP and persistent spiking properties in
layer V medial entorhinal cortex**

4.1 Introduction

The structures of the parahippocampal region are critical for working memory functions including place and object/odor recognition as measured in delayed match to sample (DMS) and delayed non-match to sample (DNMS) tasks in rodents, monkeys and humans (Zola-Morgan et al., 1989a,b; Meunier et al., 1993; Gaffan and Murray, 1992; Otto and Eichenbaum, 1992; Suzuki et al., 1993; Eacott et al., 1994; Leonard et al., 1995; Suzuki et al., 1997; Yee and Rawlins, 1998; Stern et al., 2001; Squire et al., 2004). Individual cells of the primate and rodent EC show specific firing behaviors during DMS/DNMS tasks. ‘Delay’ cells respond to sample stimuli with increased firing rates that persist throughout the delay period and subsequent presentations of test stimuli (Suzuki et al., 1997; Young et al., 1997). In humans, parahippocampal regions including the EC show sustained fMRI activity during the delay period of working memory tasks (Schon et al., 2004, 2005). These studies also found correlations between cholinergic modulation and persistent activity of the parahippocampal regions and long-term encoding of novel information. These human data is consistent with primate and rodent data demonstrating cholinergic modulation is critical for performance in working memory tasks (Penetar and McDonough, 1983; Robbins et al., 1997; Koller et al., 2003; McGaughy et al., 2005; Turchi et al., 2005, reviewed in Hasselmo and Stern, 2006).

In vitro slice experiments have further demonstrated the critical role of acetylcholine in persistent spiking behaviors found throughout the parahippocampal region (Dickson and Alonso, 1997; Klink and Alonso, 1997b,c; Dickson et al., 2000a; Egorov et al., 2002; Tahvildari et al., 2007, 2008; Yoshida and Hasselmo, 2009; Navaroli

et al., 2012; Jochems et al., 2013; Knauer et al., 2013; Anderson and Strowbridge, 2014). In order to initiate persistent spiking the majority of *in vitro* studies have used relatively long depolarizing current stimuli (1-2 s), roughly matching durations of sample stimuli presented in DMS/DNMS tasks. However, current injections as short as 200 ms and eliciting as few as 5 action potentials can induce persistent spiking in the postsubiculum (Yoshida and Hasselmo, 2009), a brain region where head direction cells are located *in vivo* (Ranck, 1984; Taube et al., 1990; Sharp, 1996). Induction of persistent firing with short duration inputs is behaviorally relevant as an animal typically moves its head through a firing field much faster than 2s.

Persistent spiking in layer V has previously been investigated with long current injections (2s) where the frequency of firing is ‘graded’ by depolarizing or hyperpolarizing pulses (Egorov et al., 2002). Persistent spiking has been used to successfully simulate the spatial periodicity of grid cell firing fields (Hasselmo, 2008; Hasselmo and Brandon, 2008). In these models persistent spiking cells receive inputs from speed modulated head direction cells with preferred angles and send convergent outputs to a grid cell. Grid patterns are formed by the phasic interactions of persistent spiking activity. When persisting spiking cells fire in phase the grid cell is active; when persistent spiking cells’ activity is out of phase the grid cell does not fire. Here we first investigate whether short duration current injections (10-100 ms) are able to induce persistent spiking in layer V medial EC principal cells. Like head direction firing fields, movement through a grid field can occur much faster than 2s. Therefore it seems likely

that if persistent firing plays a role in grid cell function, shorter inputs would need to have the ability to induce persistent activity.

The mechanism underlying persistent spiking in layer V medial EC is a calcium-activated non-specific cation current (I_{CAN}) that is gated by transient receptor potential channels (Shalinsky et al., 2002; Fransén et al., 2006; Zhang et al., 2011). Activation of I_{CAN} promotes persistent spiking with the development of a slow ADP following action potential generation (Cole and Nicoll, 1984b; Andrade, 1991; Constanti and Bagetta, 1991; Caeser et al., 1993; Haj-Dahmane and Andrade, 1996, 1998; Klink and Alonso, 1997c). In the medial EC, *in vitro* studies have not thoroughly investigated current inputs that induce ADPs without persistent spiking. Therefore, a second goal of this study was to investigate the effects of short depolarizing pulses at membrane potentials that allow characterization of the ADP. Our results show that persistent spiking can be elicited by short duration current injections. Additionally the delay to the onset of persistent spiking decreased with increased input duration. As input duration and number of spikes elicited increased, ADP amplitudes increased, the ADP rise time decreased, and the ADP decay time increased. These data suggest ADP properties can shape persistent spiking behaviors in an input-specific manner.

4.2 Materials and Methods

4.2.1 Slice preparation

We investigated the effects of muscarinic receptor activation in deep layer principal cells of medial EC. All experimental protocols were approved by the Institutional Animal Care and Use Committee of Boston University. Slice preparation

and recording techniques were similar to those in Shay et al., 2012. Briefly, male and female Long-Evans rat pups (postnatal days 17-21, Charles River, Wilmington, MA) were deeply anesthetized with 1-2 ml of isoflurane (Abbot Laboratories). After absence of tail and pedal reflex, brains were rapidly removed, submerged in ice-cold artificial cerebrospinal fluid (aCSF) containing (in mM) 125 NaCl, 2.0 CaCl₂, 2.5 KCl, 1.25 NaH₂PO₄, 25 NaHCO₃, 25 d-glucose, and 1.0 MgCl₂ (pH adjusted to 7.4 with 95% O₂-5% CO₂). Horizontal slices, 400- μ M thick, were made with a vibroslicer (Leica VT1000). Slices were immediately transferred to a holding chamber containing aCSF and incubated at 32°C for 30 minutes and were left at room temperature for 30 minutes before recordings began.

4.2.2 Electrophysiological recordings

Slices were placed in a recording chamber perfused with aCSF, constantly bubbled with 95% O₂-5% CO₂. In all recordings 2 mM kynurenic acid and 100 μ M picrotoxin were added to the recording solution to block glutamatergic and GABAergic synaptic transmission, respectively. All recordings were made between 35-37°C. Whole-cell pipettes were fabricated with borosilicate glass capillaries by means of a P-90 horizontal puller (Sutter Instruments). Pipettes were filled with an internal solution containing (in mM) 120 K-gluconate, 10 HEPES, 0.2 EGTA, 20 KCl, 2.0 MgCl₂, 4.0 Na₂ATP, 0.3 Na₃GTP, and 7 phosphocreatine-diTris (pH adjusted to 7.3 with KOH). Filled pipettes had resistances between 3-5 M Ω . Cells were visualized under an upright microscope (Zeiss Axioskop 2) using a near infrared charge-coupled device camera (JAI CV-M50IR). Tight seals (>1G Ω) were formed and whole-cell access was achieved by

brief negative pressure. Current clamp recordings were made with a Multi Clamp 700B amplifier (Axon Instruments). Built-in capacitance compensation and bridge balance circuitry was used to correct for and monitor series resistance throughout experiments. Recordings were sampled between 10-20 kHz using Clampex 10.0 (Axon Instruments).

Cells were chosen for recording based upon their location within the slice and the presence of an apical dendrite oriented towards the superficial cell layers. All cells were located in layer V, adjacent to the lamina densa. Upon whole-cell access, cells were allowed to equilibrate for 2-5 minutes. Basic cellular properties were qualitatively measured in real time to test that the presence of principal cell electrophysiological signatures (Hamam et al., 2000) that were present in all cells recorded. Inclusion criteria included resting membrane potentials below -60 mV, input resistances above 120 M Ω , presence of a weak sag potential, sMPOs, and overshooting action potentials (above zero mV). The presence of these properties suggests recordings were made from putative layer V medial EC principal cells. For the remainder of the text we refer to these cells as layer V medial EC pyramidal cells.

Cells fulfilling our inclusion criteria were then used to investigate modulation of sag, resonance, as well as the emergence of ADP and persistent spiking properties induced by continuous bath application of 5 μ M CCh (Sigma Aldrich). In control and CCh conditions, cells were held at -70 mV and 0.5 second square step currents ranging from 0 to -350 pA were delivered to cells in order to qualitatively visualize sag potentials. To identify each cell's preferred resonance frequency, the Chirp function in MATLAB (Natick, MA) was used to create a 20 second sinusoidal input increasing linearly from 0

to 20 Hz, sampled at 20 kHz. The peak-to-peak amplitude of the ZAP ranged between 25-50 pA to ensure subthreshold responses. Inputs used to measure ADP and persistent spiking properties varied. Depolarizing current pulses of 2 s, 100 ms, 50 ms, and 10 ms were delivered to test the presence of persistent spiking. To measure the ADP only the 10-100 ms impulses were used. The current amplitude was between 35-150 pA for the 2s impulse, 140 or 350 pA for the 100 and 50 ms inputs, and 350 or 700 pA for the 10 ms inputs. Input amplitudes varied because in some instances it was necessary to increase the amplitude of the inputs to generate spikes. The current amplitude used for each duration was consistent for a given cell. The large current amplitudes necessary to induce spiking with short current durations is consistent with a previous study which used 1-2 nA to induce spiking with 0.5-1 ms inputs in layer V medial EC principal cells (Reboreda et al., 2007).

4.2.3 Data analysis

Data for each run were exported from Clampex to MATLAB for analysis. Sag ratios and time constants were determined as in Heys et al., (2013). Sag ratio and time constants were taken from runs where the steady-state voltage during hyperpolarizing current injection was ± 5 mV from -92.5 mV. The sag ratio was measured with the following equation:

$$SagRatio = \frac{V_{PeakHyper}}{V_{SteadyStateHyper}} \quad (\text{eq. 4.1})$$

with the exception of the bar graph in figure 4.1C3 which was designed to compare to Heys et al., (2012) shown in figure 4.1C2. In this case the sag ratio was taken as

$SagRatio = V_{PeakHyper} - V_{SteadyStateHyper}$ (eq. 4.2) and presented in millivolts. To determine the time constant of sags, cell voltages, starting at the minimum value of the sag voltage, were fit with the following equation: $V = A1e^{(-t/\tau_1)} + A2e^{(-t/\tau_2)}$ (eq. 4.3) where A1 and A2 are the amplitude of the fast (τ_1) and slow (τ_2) time constants of the sag, respectively. All sag time constants presented are τ_1 .

Resonant frequency was determined using techniques previously described (Erchova et al., 2004; Shay et al., 2012). The impedance $[Z(f)]$ was taken as the ratio of the magnitude of the Fourier transform of the output (membrane voltage) to the magnitude of the Fourier transform of the input (ZAP and DC injection). The peak of the impedance curve, determined by MATLAB `lsqcurvefit` routine, was then taken as the resonance frequency.

Spikes were defined as a transient cell voltage of greater than 0 mV, and were found using the `findpeaks` function in MATLAB. Spike detection was used to measure the delay to onset of persistent spiking which is defined as the time from the release of input to the time of spike detection.

ADPs were measured similar to previous approaches (Koene and Hasselmo, 2007). The cell voltage minimum immediately following the release of input current was located and all voltage points after this time were used for fitting. The voltage trace was fit with the following equation: $V = B1e^{(-t/\tau_{rise})} + B2e^{(-t/\tau_{decay})} + g$ (eq. 4.4), where B1 and B2 are the amplitude of the fast (τ_{rise}) and slow (τ_{decay}) time constants of the ADP and g is roughly equivalent to the post-input steady-state voltage. Voltage traces were fit to this equation using the fit toolbox of MATLAB. For further analyses, the

ADP magnitude was determined as the difference between the minimum voltage of the AHP and peak ADP voltage, rather than the B parameter (Hasuo et al., 1990). Statistical significance was determined using paired t-tests and linear least-squares regression analyses.

4.3 Results

4.3.1 Cholinergic modulation of sag and resonance properties

Our main focus in this study was to analyze the effect of short duration depolarizing input pulses on the generation of persistent spiking and the ADP during muscarinic acetylcholine receptor activation. The effects of muscarinic activation were measured in layer V medial EC pyramidal cells.

Previous work has shown cholinergic modulation of sag and resonance properties in layer II medial EC stellate cells (Heys et al., 2010). We tested whether application of 5 μ M CCh could also modulate sag and resonance properties in layer V pyramidal cells in medial EC. These results are shown in Figure 4.1. Population (n=12) analyses resulted in a significant decrease in the sag amplitude following CCh application (Fig. 4.1C, paired t-test; $p < 0.001$), but no significant change in the sag fast time constant (Fig. 4.1D). Resonance frequency was only modestly decreased in the population of cells (Fig. 4.1E, n=8), as even in baseline conditions cells behaved as low pass filters (Fig. 4.1B1). We compared the changes in sag amplitude in our data with Heys et al. (2010) and found a similar decreasing magnitude with CCh (Fig. 4.1C2-C3). While our analyses measured sag properties with layer V cells held at -70 mV and steady-state voltages between -88.5 and -97.5 mV, layer II stellate cells were held at -65 mV and steady-state voltages were

between -70 and -76 mV. The need to step to much more hyperpolarized steady-state voltages in layer V cells to reach equivalent sag amplitudes reported in layer II stellates is consistent with reports that layer V cells have a much weaker sag than layer II cells (Hamam et al., 2000).

4.3.2 Input duration affects persistent spiking

Figure 4.2 shows representative examples of persistent firing in two different pyramidal cells (A, B). We were able to elicit persistent spiking behavior from 2 s (Fig. 4.2A2, B1) 100 ms (Fig. 4.2A4), 50 ms (Fig. 4.2B2), and 10 ms (Fig. 4.2A5, B3) current injections. Under baseline conditions cells did not display persistent firing (Fig 4.2A1, A3). However, upon application of CCh, cells responded to depolarizing inputs with persistent spiking. It is important to note that persistent spiking was rarely initiated from holding potentials negative to -60 mV, consistent with other studies (Egorov et al., 2002, Yoshida and Hasselmo, 2009). Persistent spiking could not be turned off by long hyperpolarizing pulses (Fig. 4.2A2, B1) and graded persistent firing was not present in our experimental conditions. Whereas Egorov and colleagues (2002) performed sharp electrode recordings, the use of whole-cell recording configuration makes graded persistent firing difficult to obtain and affects the ability to terminate persistent spiking (personal communication, Dr. Motoharu Yoshida). These effects could be a consequence of cell washout, as intracellular cascades have been proposed to underlie graded persistent spiking (Fransén et al., 2006).

Cells often responded to current injections with a plateau potential in which sMPOs preceded persistent spiking behavior. Examples of this oscillatory response are

shown in Figures 4.2A5 and B2. An important finding of our persistent spiking analysis is that the duration of the plateau potential, or the delay to the onset of persistent spiking, was correlated with the duration of the depolarizing pulse. The population (n=18) analysis shows that as the pulse duration increased, the delay to the first spike significantly decreased across all input durations (Fig. 4.2C, see figure legend for significance values). The relationship between pulse duration and onset of spiking is also demonstrated in the representative cell examples (Fig. 4.2A4-A5; B2-B3).

4.3.3 Input duration affects ADP properties

Given our above findings, and the fact that persistent spiking is supported by the activation of a slow ADP (Cole and Nicoll, 1984b; Klink and Alonso, 1993c), we next investigated how different pulse durations affected the amplitude and time constants of the ADP. These results are shown in Figure 4.3. Panel A shows the averaged voltage traces (n=5 runs) from a representative cell in response to 100 ms (A1), 50 ms (A2) and 10 ms (A3) pulse durations delivered at -65 mV. The population analyses of ADP amplitude (B) show that the 100 and 50 ms pulse resulted in significantly larger ADP amplitudes compared to the 10 ms input (paired *t*-test, $p < 0.01$). Although ADP amplitudes induced by 50 and 100 ms pulses were not statistically different, there was a general trend of increasing amplitudes with increased pulse duration. The ADP decay time constant (Fig. 4.3D) tended to decrease (indicating a faster decay) with increasing pulse duration but this trend did not reach statistical significance. However the pulse duration did significantly affect the ADP rise time constant. The 100 ms input rise time constant (Fig. 4.3C) was significantly larger (indicating a slower rise) than the rise time

constant for both the 10 ms (paired *t*-test, $p < 0.001$) and 50 ms input (paired *t*-test, $p < 0.01$). These data suggest that the duration of input shapes aspects of the ADP, namely amplitude and rise time constant. Longer pulse duration causes larger amplitude ADP, with slower rise times but faster decay times.

4.3.4 Spike number affects ADP properties

Next we tested whether the changes in ADP amplitudes and time constants with increased pulse duration could be due to differences in the number of spikes generated during input pulses. Although the 10, 50 and 100 ms inputs gave increasingly larger spike numbers on average (data not shown), the exact number of spikes generated could not be controlled with continuous injection. To control the number of spikes we delivered current inputs containing 2, 3, or 5 pulses, where each pulse was 10 ms in duration and produced a single spike. The results of these experiments are shown in Figure 4.4. Figure 5.4A shows the average ($n=5$ runs) voltage response of a cell to inputs containing 5 pulses (A1), 3 pulses (A2) and 2 pulses (A3). The ADP amplitude increased as the number of spikes generated increased. This effect was consistent across the cell population ($n=6$, Fig. 4.4B). In addition, the ADP rise time constant and decay time constant also changed with pulse number. Inputs containing 5 pulses led to a significantly longer average population ($n=6$) rise time constant compared to 3-pulse (paired *t*-test, $p < 0.05$) and 2-pulse (paired *t*-test, $p < 0.01$) inputs (Fig. 4.4C), while inputs containing 5 pulses (paired *t*-test, $p < 0.05$) and 3 pulses (paired *t*-test, $p < 0.01$) led to a significantly shorter average population ($n=6$) decay time constant compared to 2-pulse

inputs (Fig. 4.4D). These data suggest the number of spikes generated during an excitatory input influence the amplitude, rise time constant, and decay time constant of the ADP, with more spikes causing a slower rise time and a faster decay time.

4.3.5 Voltage affects ADP properties

In addition to spike number, we measured ADP amplitude and time constants as a function of holding voltage. Figure 4.5 shows these results. Across the cell population the ADP amplitude significantly increased as cells were depolarized (Fig. 4.5A, $R^2=0.243$, $p<0.001$), the ADP rise time constant significantly increased with membrane depolarization (Fig. 4.5B, $R^2=0.230$, $p<0.001$), but there was no significant correlation between ADP decay time constant and voltage (Fig. 4.5C). When recordings were plotted in 5 mV bins according to a cell's holding potential, the ADP amplitude increased with pulse duration (Fig. 4.5D). Inputs eliciting 2, 3 and 5 spikes resulted in ADP amplitudes that generally increased with holding potential (Fig. 4.5E). However inputs generating 2 spikes increased only slightly with potential. These results suggest that along with the number of spikes elicited during an input, the membrane potential at which inputs are given plays a role in the generation of the ADP. We delivered subthreshold current pulses during the ADP to further investigate the voltage dependence of the ADP (data not shown). Cells responded with sharp voltage deflections that quickly decayed. Throughout this process the underlying ADP was clearly visible, suggesting spiking and subsequent I_{CAN} activation determined ADP properties.

4.4 Discussion

4.4.1 Summary of findings

The data presented here show that under mAChR activation, persistent spiking in layer V medial EC pyramidal cells can be elicited from depolarizing inputs with shorter durations (10, 50, and 100 ms) than previously described (Egorov et al., 2002). Our data suggest that the progressive decrease of the delay to the onset of persistent firing is likely due to changes in the ADP amplitude as input duration is increased. Increases in the ADP amplitude would promote earlier persistent spiking.

The change in time constants could counteract the effect of change in amplitude, because slower rise time constants would be expected to delay firing, but this change in time constant appears to be overcome by the greater amplitude to result in earlier persistent spiking. In contrast, the faster rise time constant with short pulse duration (10 ms) appears consistent with the fast ADP after individual spikes (Hamam et al., 2000; Navritolova et al., 2012) that could maintain persistent spiking at the frequencies observed here. Although we observed a non-significant decreasing trend between decay time constant and pulse duration, significance was reached when the number of spikes was controlled, suggesting the effect of continuous pulse duration could have been obfuscated by inconsistent numbers of action potentials generated during the 10, 50, and 100 ms duration stimuli, whereas a fixed number of spikes revealed the effect.

In some instances plateau potentials were accompanied by sMPOs that then triggered spiking activity. Muscarinic stimulation has been reported to activate I_{NaP} giving rise the rhythmic activity in CA1 pyramidal cells (Yamada-Hanff and Bean,

2013). Activation of I_{NaP} is voltage dependent with $V_{1/2} = -53 \pm 1$ mV, the approximate voltages where sMPOs and persistent spiking occurred in medial EC layer V cells. Similarly, persistent sodium channels are present in the medial EC where they are involved in oscillatory behavior and have as similar voltage-dependence as in CA1 (Alonso and Llinas, 1989; Magistretti and Alonso, 1999). Oscillatory behavior during the plateau potential may be due to a balance between I_{CAN} and I_{NaP} , with persistent activity occurring upon disruption of this balance. This interaction between I_{CAN} and I_{NaP} may also be why persistent spiking can rarely be induced at holding potentials below -60 mV. It may be necessary for the ADP to reach membrane potentials where I_{NaP} is sufficiently activated in order to initiate persistent spiking. The voltage dependence of the ADP observed in our data is likely due to increased calcium influx through activation of voltage-gated calcium channels. The fact that post-pulses did not affect the ADP is consistent with the idea that calcium entry due to spikes during current injections largely determines ADP properties. The fact that changes in intracellular calcium concentration through activation of voltage-gated calcium channels bi-directionally regulate I_{CAN} in layer II medial EC neurons (Magistretti et al., 2004) supports this interpretation.

We also show that following muscarinic activation the sag amplitude in layer V medial EC principal cells decreases. This decrease in sag amplitude was not accompanied with a decrease in the fast sag time constant as reported in layer II medial EC stellate cells (Heys et al., 2010). This could be due to differences in the expression of HCN subunits between the two layers, as the sag amplitude is much smaller in layer V cells compared to stellate cells (Hamam et al., 2000) and our layer V cells had much

lower resonance frequencies (2-3 Hz) than stellate cells (Hass and White, 2002; Erchova et al., 2004; Giocomo et al., 2007; Heys et al., 2010; Shay et al., 2012). Despite this difference we still observed decreases in resonance frequency, consistent with findings that the I_h amplitude and not time constant underlies cholinergic modulation of resonant frequency (Heys et al., 2012).

4.4.2 Implications

Simulations of the influence of I_{CAN} have been used to simulate cellular activity during performance in DMS tasks, including persistent activity during the delay period and spike enhancement to a matching stimulus (Fransén et al., 2002). Under conditions of high I_{CAN} activation (mediated by high calcium influx) the model is able to replicate persistent spiking during the delay period. This can be viewed as analogous to the long duration inputs used in our study, where calcium influx/ I_{CAN} activation would be the highest. Accordingly, longer duration inputs were those that had a very short delay to spiking and did not result in plateau potentials. In contrast, the model achieves match enhancement through low levels of I_{CAN} , causing sustained subthreshold depolarization via plateau potentials in response to the presentation of a ‘sample’ input. Upon the presentation of a second ‘matching’ input, the plateau potential supports increased firing rates compared to the initial ‘sample’ input. Similarly, the plateau potentials recorded in our data are a manner in which a cell’s response to an input can be modified based on its previous activity. Furthermore, the plateau potentials in our data were more common with the shorter inputs (which led to longer delays to spiking) and would therefore likely match the smaller calcium influx/ I_{CAN} activation used in the model.

Recent computational models have utilized resonance and rebound spiking properties of layer II medial EC stellate cells to produce grid cell spatial periodicity and theta phase precession (Hasselmo, 2013; Hasselmo and Shay, 2014). Given the lack of theta resonance and post inhibitory rebound spiking properties in layer V, an alternative mechanism for grid formation in this cell layer could be rebound spiking in response to excitation. Persistent spiking provides a mechanism for such excitation-induced rebound activity. The ability of short duration inputs to induce persistent spiking is important within the framework of these models as the short time courses more closely match the time course of inhibition necessary to generate phase specific spiking of individual cells. The input durations used here are also more behaviorally relevant to an animal actively navigating. The duration of excitatory inputs inducing persistent spiking could be a correlate for the magnitude of inhibition used to maintain grid fields and spacing with changes in running velocity in these models. The use of excitation-driven stimuli in deep layer medial EC is supported by functional connectivity studies showing layer V contains far more recurrent excitatory connections than layer II (Dhillon and Jones, 2000), while layer II stellates are embedded in a dense recurrent inhibitory microcircuit (Couey et al., 2013; Pastoll et al., 2013). In addition, spontaneous GABA-A IPSPs occur in layer II 4-5 times more often than layer V (Woodhall et al., 2005).

The medium AHP and ADP time constants in layer II medial EC stellate cells have been used to model theta phase precession and the gradient of grid cell field size and spacing along the D/V axis (Navratilova et al., 2012). The data presented here suggest that the cholinergic modulation of the ADP amplitude and time constants could alter the

slope of phase precession as well as the grid field size and spacing within the context of this model. Congruent with this, changes in grid field size have been noted in novel environments, a condition in which acetylcholine levels are increased (Acquas et al., 1996; Barry et al., 2008; 2012).

4.5 Figures

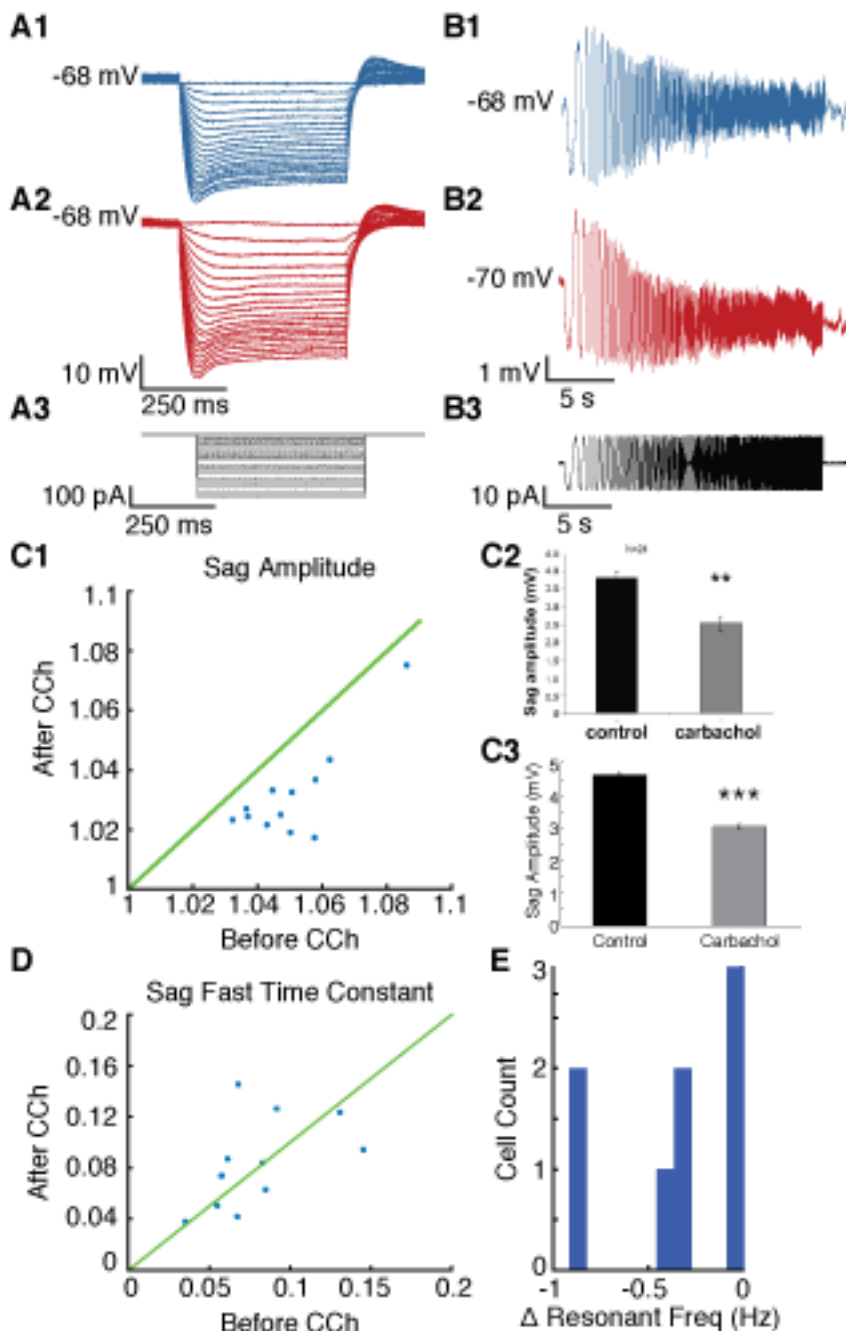


Figure 4.1 Cholinergic modulation of sag amplitude and resonance frequency

(A) Panel **A1** and **A2** show representative examples of the sag amplitude before and after application of 5 μ M CCh, respectively. Panel **A3** displays the hyperpolarizing current steps used to elicit sag. (B) Panel **B1** and **B2** show voltage responses to ZAP current

injections (**B3**) before and after application of CCh, respectively. Data for **A-B** are from the same cell. (**C-E**) Panels show the population effects of CCh on the sag amplitude (**C1**), the sag fast time constant (**D**) and resonance frequency (**E**). For comparison, the cholinergic decrease in sag amplitude in layer II stellate cells (**C2**, adapted from Heys et al., 2010) and here in putative layer V principal cells (**C3**) are shown. See Results for further description. Significance: paired *t*-test, **, $p < 0.01$; ***, $p < 0.001$.

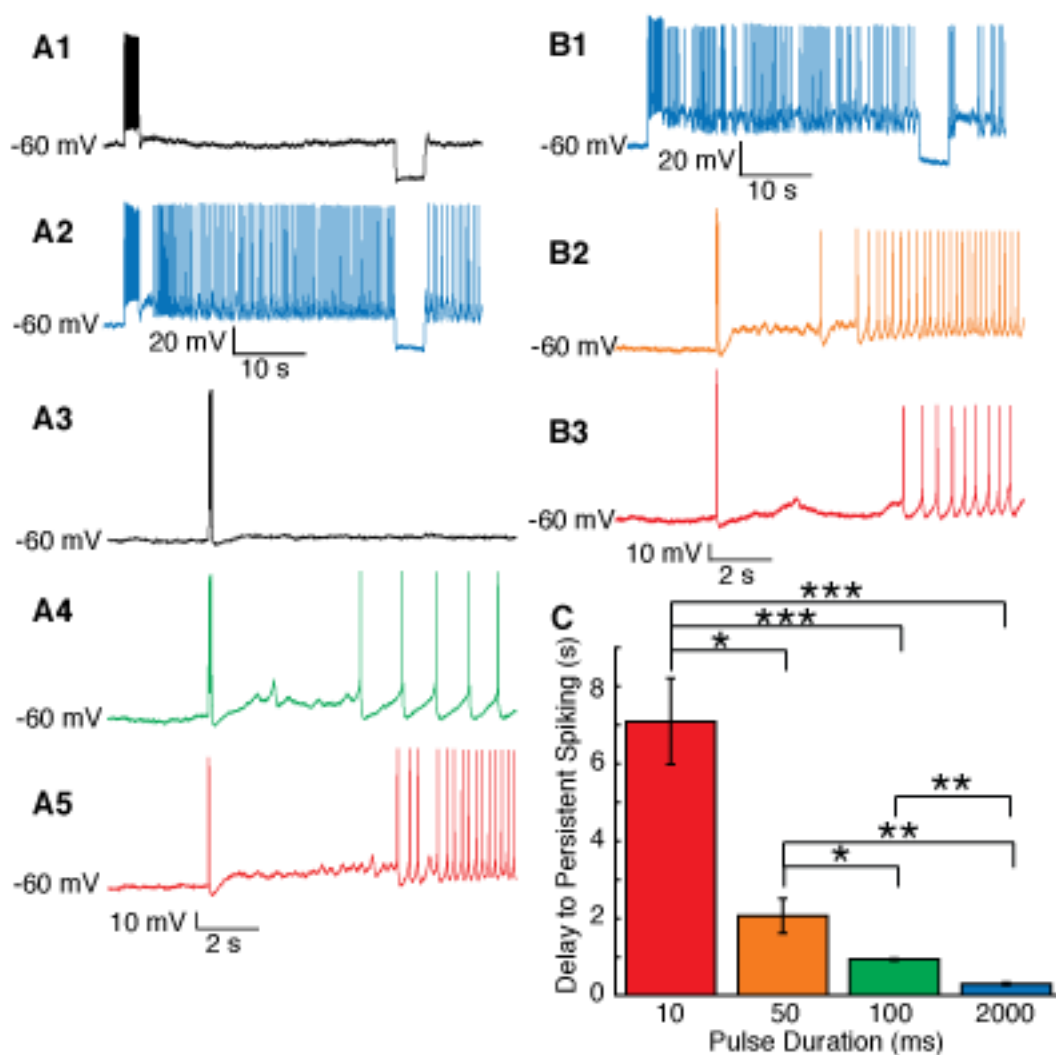


Figure 4.2 Pulse duration affects onset of persistent spiking

(A) Panels show representative examples from a single cell of persistent spiking in response to a 2 second (A1), 100 ms (A3) and 10 ms (A5) depolarizing pulse (not shown) in the presence of CCh. Panels A1 and A3 show responses in control conditions to a 2 s and 100 ms pulse, respectively. (B) Panels show additional examples of persistent spiking from a second cell in response to a 2 second (B1), 50 ms (B2), and 10 ms (B3) pulse duration. (C) Population data show the delay to persistent spiking increases as a function of pulse duration. As pulse duration decreases, the delay to the first spike of persistent spiking increases. Significance: paired *t*-test, ***, $p < 0.001$; **, $p < 0.01$; *, $p < 0.05$.

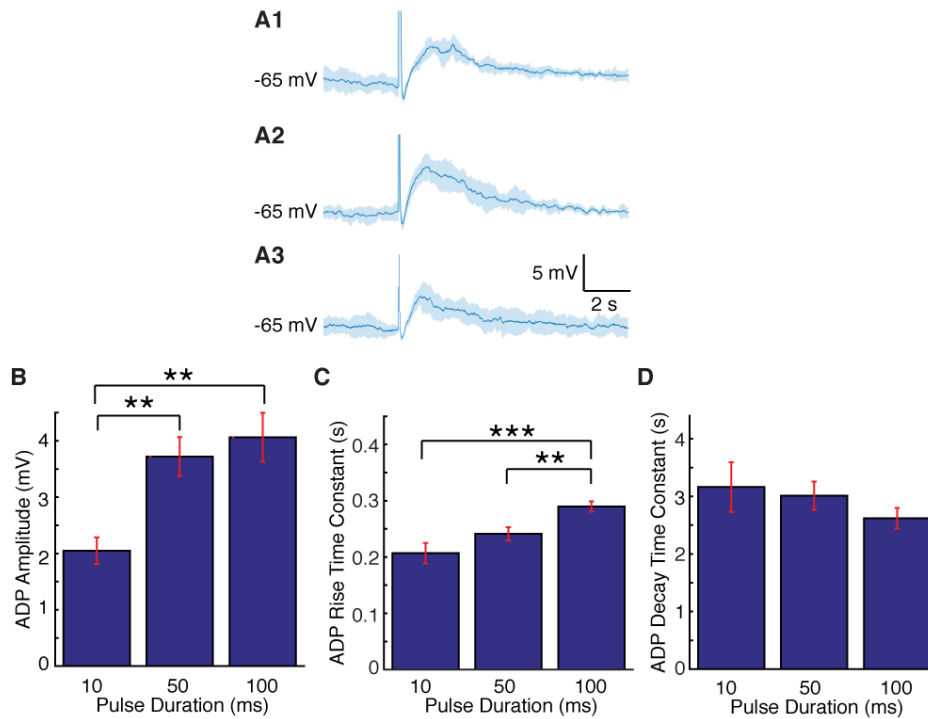


Figure 4.3 Pulse duration affects ADP amplitude and time constants

(A) Data from a single cell show averaged voltage traces for 100 ms (A1), 50 ms (A2), and 10 ms (A3) pulse durations. Note the prominent ADP following the generation of spikes. (B-D) Population bar plots show that the ADP amplitude increased with increasing pulse duration (B), the ADP rise time constant increased with increasing pulse duration (C), and while the ADP decay time constant decreased with increasing pulse duration, significance was not reached (D). Significance: paired *t*-test, ***, $p < 0.001$; **, $p < 0.01$.

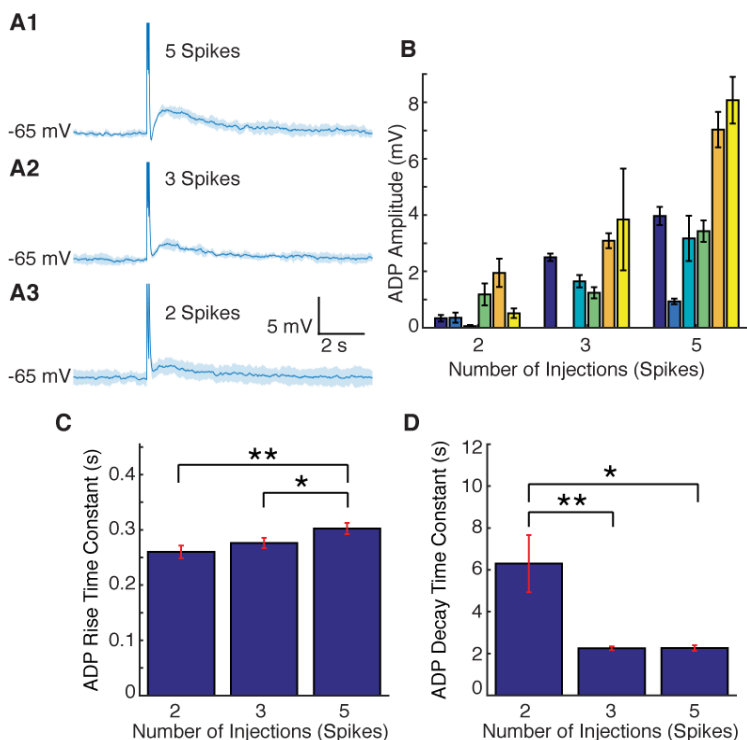


Figure 4.4 Pulse number affects ADP amplitude and time constants

(A) Panels show representative examples from a single cell of the averaged voltage response to inputs containing 5 (A1), 3 (A2), and 2 (A3) 10 ms current pulses. Each 10 ms pulse always generated a single spike, and therefore spike number could be controlled. Note the increasing ADP amplitudes. (B) Population data ($n=6$) show within each cell (denoted by different colors) and across the population, the amplitude of the ADP increased as the number of action potentials generated increased. (C-D) The ADP rise time constant increased with increasing pulse number (C) and the ADP decay time constant decreased with increasing pulse number (D). Significance: paired t -test, *, $p < 0.05$; **, $p < 0.01$.

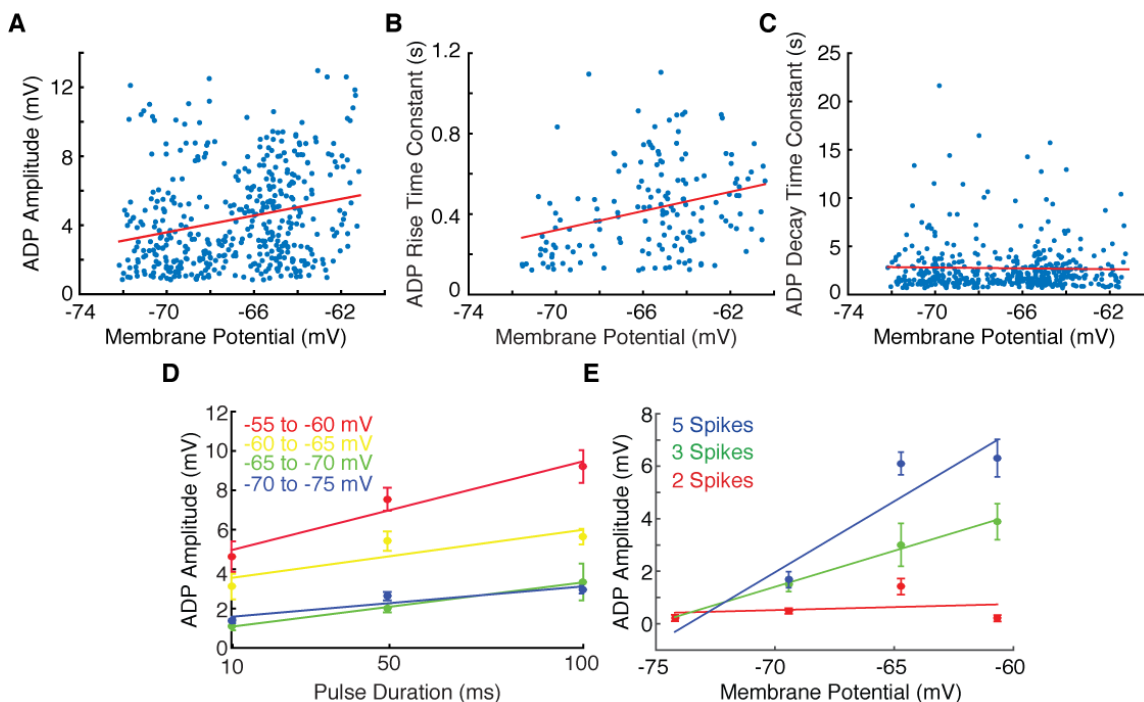


Figure 4.5 Voltage affects ADP amplitude and time constants

(A-C) Panels show population data for ADP amplitude, ADP rise time constant, and ADP decay time constant as functions of membrane potential. Linear regression analyses show the ADP amplitude (A) increased significantly with membrane depolarization ($R^2=0.243$, $p<0.001$), the rise time constant (B) significantly increased with membrane depolarization ($R^2=0.230$, $p<0.001$), but the ADP decay time (B) did not change significantly with membrane depolarization. (D) The ADP amplitude as a function of pulse duration is plotted in voltage bins (-55 to -60 mV, red, $R^2=0.7495$; -60 to -65 mV, yellow, $R^2=0.7517$; -65 to -70 mV, green, $R^2=0.9520$; -70 to -75 mV, blue, $R^2=0.9993$). For a given pulse duration, larger ADP amplitudes occurred with depolarization. This effect is less pronounced in more hyperpolarized potentials (green and blue) where the ADP is generally smaller. (E) The ADP amplitude as a function of membrane potential is plotted for 10 ms input pulses eliciting 5 (blue, $R^2=0.92$), 3 (green, $R^2=0.98$), and 2 (red, $R^2=0.22$) action potentials. As cells were held at more depolarized membrane potentials, ADP amplitudes increased for the 5, 3, and 2-pulse inputs.

CHAPTER 5: Discussion

5.1 Implications

The work presented in this thesis contributes to experimental and modeling studies working towards elucidating the neural mechanisms underlying spatial processing in the medial EC. The experiments described in chapter 2 were inspired by a subset of oscillatory interference models which use depolarizing inputs from head direction and speed-modulated cells to change oscillation frequencies (Burgess et al., 2007; Hasselmo et al., 2007). These models require a linear relationship between sMPO frequency and voltage to maintain consistent locations of grid firing fields across running speeds. However, experiments have demonstrated the frequency of sMPOs do not change linearly with membrane potential (Yoshida et al., 2011). Our data offer resonance as an alternative mechanism to oscillations, as resonance frequency linearly changed with membrane potential in layer II medial EC stellate cells. Resonance may contribute to local circuit oscillations involving interactions of populations of excitatory cells, or interactions of excitatory cells with inhibitory cells (Zilli and Hasselmo, 2010). Depolarizing inputs from head direction cells (Taube et al., 1990; Taube and Basset, 2003; Sargolini et al., 2006) and or speed-modulated cells (Sharp, 1996; O'Keefe et al., 1998; Wills et al., 2012) could shift the frequency of these local circuit interactions to generate grid cell firing fields.

The possible role of resonance in grid cell generation has been demonstrated by experiments studying the muscarinic cholinergic modulation of resonance and I_h properties in layer II medial EC stellate cells (Heys et al., 2010; Heys and Hasselmo,

2012). Activation of mAChRs decreases resonance frequencies and sag potentials of stellate cells (Heys et al., 2010). In oscillatory interference models, decreased frequencies increase the size and spacing of grid cell firing fields. Grid cell firing patterns expand in novel environments (Barry et al., 2008, Barry et al., 2012a), a condition in which cholinergic tone is increased (Acquas et al., 1996). Therefore decreases in resonance frequency induced by cholinergic modulation are proposed to underlie the expansion of grid cell firing field properties observed in novel environments (reviewed in Barry et al., 2012b). Voltage clamp studies suggest these cholinergic modulatory effects are likely mediated by a decrease in I_h activation (Heys and Hasselmo, 2012). This interpretation is consistent with findings in HCN1 knockout mice. *In vitro* studies have shown that knockout of HCN1 subunits decreases sag amplitudes and increases fast sag time constants, while flattening the D/V gradient of sMPO and resonance frequencies in stellate cells (Giocomo and Hasselmo, 2009). *In vivo* unit recordings have shown that the size and spacing of grid cell firing fields are increased in HCN1 knockout mice (Giocomo et al., 2011). Together the results of the above studies and our study provide evidence that I_h and cellular properties dependent on I_h influence grid cell firing properties.

Recent data recorded from the bat medial EC challenge the use of oscillatory interference mechanisms in the generation of grid cells. Bat LFP recordings lack continuous theta oscillatory activity despite the presence of grid cells (Yartsev et al., 2011) and *in vitro* experiments have shown that bat medial EC neurons lack theta resonance frequencies and have reduced sag ratios compared to rats (Heys et al., 2013a).

However, preliminary results from a follow-up study have shown resonance frequency increases and sag time constant decreases as a function of D/V position in bat EC neurons (Heys et al., 2013b). These gradients are opposite to those found in rats (Giocomo et al., 2007; Giocomo and Hasselmo, 2009; Boehlen et al., 2010). An interesting question is whether bats would show similar effects to rats with genetic knockout of HCN1 channels? Given that bats navigate very differently than rats, the inverse gradient of bat properties could reflect different inputs to EC, different EC microcircuitry, or different mechanisms underlying grid formation. Another possibility is that I_h and resonance may be part of a number of mechanisms used to generate grid cells. Intracellular recordings have demonstrated that combinations of aspects from both CANN models and oscillatory interference models best account for the membrane potential dynamics in grid cells (Domnisoru et al., 2013; Schmidt-Hieber and Häusser, 2013).

Chapter 3 extends the idea that cellular properties mediated by I_h can generate grid cells. Data demonstrated that resonance and rebound spiking properties of medial EC stellate cells are able to generate grid cell firing properties when placed in a recurrent inhibitory network receiving medial septal theta input. The network connectivity used in the rebound spiking model is supported by *in vivo* findings. Beutfering and colleagues (2014) have reported that multiple grid cells synapse onto a given medial EC PV interneuron. In the rebound spiking model, multiple stellate cells send feedforward excitation to an interneuron providing feedback inhibition to other stellate cells. Stellate cells in the rebound spiking model receive theta oscillatory input from the medial septum. This may seem contradictory to a recent study that reported GABAergic projections from

the medial septum target interneurons of medial EC (Gonzalez-Sulser et al., 2014) but the functional connectivity between these interneurons and stellate cells has not been demonstrated. The model of direct oscillatory input to stellate cells can be seen as representative of an indirect effect of medial septal input in causing rhythmic modulation of stellate cells from one set of interneurons that can then interact with feedback inhibition from another set of interneurons.

The relationship between resonance and rebound spiking has been demonstrated *in vivo* with the use of chirp-patterned optogenetic stimulation of pyramidal cells and PV interneurons of CA1 and neocortex (Stark et al., 2013). Pyramidal cells responded to direct optogenetic activation with firing at different frequencies covering the range (0-40 Hz) of the chirp stimulus. In contrast, optogenetic activation of PV interneurons caused rebound spikes that occurred specifically within theta-band frequencies. Similar to the shifts in output spiking phase observed in our rebound spiking data, the frequency of theta-band spiking resonance was modulated by the magnitude of inhibition. Stark and colleagues (2013) showed rebound spiking resonance was dependent on I_h , similar to our finding that I_h mediated the phase specificity of rebound spiking in medial EC stellate cells. It is an open question whether stellate cells would display similar resonance properties to *in vivo* chirp functions. However, it seems possible as stellate cells possess even stronger resonance properties compared to CA1 and neocortical pyramidal cells, including I_h , subthreshold resonance, and connectivity with PV interneurons (Alonso and Llinas, 1989; Erchova et al., 2004; Couey et al., 2013; Pastoll et al., 2013). If this were true, the magnitude of inhibition could function as a speed signal shifting the frequency

of spiking to contribute to grid cell formation. PV interneurons have differential connectivity with stellate cells along the D/V axis of medial EC. Dorsal stellate cells receive a greater number and more widespread inhibition than ventral cells (Beed et al., 2013). These inhibitory differences could contribute to the D/V gradient of grid field size and spacing by supporting different preferred firing frequencies in response to inhibition in dorsal versus ventral stellates. Future investigations of resonance and rebound spiking properties in medial EC of navigating animals could help answer these questions.

While resonance and rebound spiking properties of stellate cells can be used as mechanisms to model grid cells, what mechanisms could cells lacking these properties use to generate grids? Persistent spiking has been used to model grid cell periodicity (Hasselmo, 2008; Hasselmo and Brandon, 2008). The experiments in chapter 4 were inspired by these modeling studies. Our results confirmed short duration current inputs can elicit persistent spiking in layer V principal cells of medial EC. Short duration inputs may be more relevant for a navigating animal and more closely match the time an animal spends in a given head direction or grid cell firing field.

A possible interpretation of our data is that differential calcium influx and concomitant activation of I_{CAN} was responsible for correlations between spike number, ADP amplitude and the onset of persistent spiking. I_{CAN} activation has been used to model match enhancement and persistent activity observed in DMS/DNMS working memory tasks (Fransén et al., 2002). This model used low levels of I_{CAN} activation to obtain sustained depolarization during the delay period, which enabled increased firing rates to a matching stimulus, similar to *in vivo* unit recording data. In our *in vitro* data the

shortest inputs elicited a smaller number of spikes (low calcium influx) and could cause plateau potentials without spiking activity. Longer duration inputs, causing a larger number of spikes (high calcium influx), did not show long plateau potentials because they had shorter delays to persistent spiking, similar to high I_{CAN} activation levels used in the model to simulate persistent firing during the delay period.

Acetylcholine plays an important role in the encoding of new memories (reviewed in Hasselmo, 2006; Hasselmo and Stern, 2006). Nicotinic activation enhances afferent inputs to cortical structures (Gil et al., 1997; Gioanni et al., 1999; Radcliffe et al., 1999; Giocomo and Hasselmo, 2005), while muscarinic receptor activation suppresses recurrent excitatory feedback (Hasselmo and Bower, 1992; Hasselmo and Schnell, 1994; Hasselmo et al., 1995; Vogt and Regehr, 2001; Fernandez de Sevilla et al., 2002; Fernandez de Sevilla and Buno 2003; Kunitake et al., 2004). Muscarinic activated persistent spiking can then act to potentiate afferent inputs during encoding. Our data show the ADP underlying persistent spiking is shaped by the duration of inputs and the number of spikes elicited during an input, suggesting that the strength/duration of an input could influence encoding of new information. Lower levels of activation may be more susceptible to interference from previously learned information as the ADP is smaller and slower, leading to longer delays to persistent firing.

5.2 Future directions

A greater understanding of the medial EC microcircuit will be important for the development of future grid cell models. Recently a technique using implantation of

microprisms in mice has enabled 2-photon calcium imaging in relatively deep (300-400 μm) penetrations of medial EC during running on a virtual linear track (Heys et al., 2014). This optical approach enables simultaneous measurements of activity in hundreds of cells and provides resolution at the cellular level. Future developments in imaging are expected to allow deep tissue imaging (2-3 mm, Ford et al., 2012) which could provide a better understanding of deep layer grid cells and their interactions with other cells in the medial EC microcircuit.

Relatively little is known about medial EC interneurons. Classification of interneurons is complex and can be done using many different criteria including expression of neurochemicals and axonal targets onto principal cell spatial domains (Freund and Buzsáki, 1996; Ascoli et al., 2008; Rudy et al., 2011). Genetic expression of fluorescent proteins allows recording in select populations of cells. Tahvildari and colleagues (2012) have used such mice lines to investigate functional connectivity between stellate cells and interneurons expressing somatostatin, neuropeptide Y, vasoactive intestinal peptide, and ionotropic serotonin 3a receptors during up-and-down states. Future studies recording from distinct populations of interneurons could help answer the many questions regarding EC interneuron microcircuitry. For instance does the expression of certain neurochemical markers correlate with innervation of particular principal cell domains? What are the functional roles of different types of interneurons? What are the effects of cholinergic modulation in specific subtypes of EC interneurons?

Viral injection of channelrhodopsins is a powerful tool to precisely identify and control the activity of specific cell types *in vitro* and *in vivo*. Although technically

challenging, future studies pairing optogenetic techniques with *in vivo* intracellular recordings may be critical in determining the sources of CANN and oscillatory interference mechanisms posited to underlie grid cell formation (Domnisoru et al., 2013; Schmidt-Heiber and Hausser, 2013). The use of channelrhodopsins has recently demonstrated the functional anatomical connectivity between medial EC and the medial septum (Gonzalez-Sulser et al., 2014). The use of the pseudo rabies virus (Wall et al., 2010; Wickersham et al., 2010) will also be a valuable tool in the study of monosynaptic connections between brain regions and within the medial EC microcircuit.

BIBLIOGRAPHY

Acquas E, Wilson C, Fibiger HC (1996) Conditioned and unconditioned stimuli increase frontal cortical and hippocampal acetylcholine release: effects of novelty, habituation, and fear. *Journal of Neuroscience* 16:3089-3096.

Adhikari MH, Quilichini PP, Roy D, Jirsa V, Bernard C (2012) Brain state dependent postinhibitory rebound in entorhinal cortex interneurons. *Journal of Neuroscience* 32:6501-6510.

Alonso A, Klink R (1993) Differential electroresponsiveness of stellate and pyramidal-like cells of medial entorhinal cortex layer II. *Journal of Neurophysiology* 70:128-143.

Alonso A, Köhler C (1984) A study of the reciprocal connections between the septum and the entorhinal area using anterograde and retrograde axonal transport methods in the rat brain. *Journal of Comparative Neurology* 225:327-343.

Alonso A, Garcia-Austt E (1987) Neuronal sources of theta rhythm in the entorhinal cortex of the rat II: Phase relations between unit discharges and theta field potentials. *Journal of Comparative Neurology* 67:502-509.

Alonso A, Llinás RR (1989) Subthreshold Na⁺-dependent theta-like rhythmicity in stellate cells of entorhinal cortex layer II. *Nature* 342:175-177.

Alonso JR, Coveñas R, Lara J, Aijón J (1990) Distribution of parvalbumin immunoreactivity in the rat septal area. *Brain Research Bulletin* 24:41-48.

Amaral DG (1993) Emerging principles of intrinsic hippocampal organization. *Current Opinion in Neurobiology* 3:225-229.

Anderson RW, Strowbridge BW (2014) Regulation of persistent activity in hippocampal mossy cells by inhibitory synaptic potentials. *Learning and Memory* 21:263-271.

Andrade R (1991) Cell excitation enhances muscarinic cholinergic responses in rat association cortex. *Brain Research* 548:81-93.

Ascoli GA et al (2008) Petilla terminology: nomenclature of features of GABAergic interneurons of the cerebral cortex. *Nature Reviews Neuroscience* 9:557-568.

Barry C, Fleming SM, Jeewajee A, O'Keefe J, Burgess N (2008) Effect of novelty on grid cell firing. *Proceedings of the International Conference on Cognitive and Neural Systems* 12:35.

- Barry C, Ginzberg LL, O'Keefe J, Burgess N (2012a) Grid cell firing patterns signal environmental novelty by expansion. *Proceedings of the National Academy of Sciences of the United States of America* 109:17687-17692.
- Barry C, Hayman R, Burgess N, Jeffery K J (2007) Experience-dependent rescaling of entorhinal grids. *Nature Neuroscience* 10:682-4.
- Barry C, Heys JG, Hasselmo ME (2012b) Possible role of acetylcholine in regulating spatial novelty effects on theta rhythm and grid cells. *Frontiers in Neural Circuits* 6:5.
- Beckstead RM (1978) Afferent connections of the entorhinal area in the rat as demonstrated by retrograde cell-labeling with horseradish peroxidase. *Brain Research* 152:249-264.
- Beed P, Gundlfinger A, Schneiderbauer S, Song J, Böhm C, Burgalossi A, Brecht M, Vida I, Schmitz D (2013) Inhibitory gradient along the dorsoventral axis in the medial entorhinal cortex. *Neuron* 79:1197-1207.
- Benardo LS, Prince DA (1982) Ionic mechanisms of cholinergic excitation in mammalian hippocampal pyramidal cells. *Brain Research* 249:333-344.
- Berens P (2009) CircStat: a MATLAB toolbox for circular statistics. *Journal of Statistical Software* 31:1-21.
- Bjerknes TL, Langston RF, Krugue IU, Moser EI, Moser M-B (2014) Coherence among head direction cells before eye opening in rat pups. *Current Biology* 25:103-108.
- Blackstad TW, Brink K, Hem J, Jeune B (1970) Distribution of hippocampal mossy fibers in the rat. An experimental study with silver impregnation methods. *Journal of Comparative Neurology* 138:433-449.
- Blair HT, Gupta K, Zhang K (2008) Conversion of a phase- to a rate-coded position signal by a three-stage model of theta cells, grid cells, and place cells. *Hippocampus* 18:1239-1255.
- Blair HT, Wolday AC, Zhang K (2007) Scale-invariant memory representations emerge from moiré interference between grid fields that produce theta oscillations: a computational model. *Journal of Neuroscience* 27:3211-3229.
- Boccaro CN, Sargolini F, Thoresen VH, Solstad T, Witter MP, Moser EI, Moser M-B (2010) Grid cells in pre- and parasubiculum. *Nature Neuroscience* 13:987-994.

- Boehlen A, Heinemann U, Erchova I (2010) The range of intrinsic frequencies represented by medial entorhinal cortex stellate cells extends with age. *Journal of Neuroscience* 30:4585-4589.
- Brandon MP, Bogaard AR, Andrews CM, Hasselmo ME (2012) Head direction cells in the postsubiculum do not show replay of prior waking sequences during sleep. *Hippocampus*.
- Brandon MP, Bogaard AR, Libby CP, Connerney MA, Gupta K, Hasselmo ME (2011) Reduction of theta rhythm dissociates grid cell spatial periodicity from directional tuning. *Science* 332:595-599.
- Brandon MP, Bogaard AR, Schultheiss NW, Hasselmo ME (2013) Segregation of cortical head direction cell assemblies on alternating theta cycles. *Nature Neuroscience* 16:739-748.
- Brun VH, Solstad T, Kjelstrup KB, Fyhn M, Witter MP, Moser EI, Moser M-B (2008) Progressive increase in grid scale from dorsal to ventral medial entorhinal cortex. *Hippocampus* 18:1200-1212.
- Buetfering C, Allen K, Monyer H (2014) Parvalbumin interneurons provide grid cell-driven recurrent inhibition in the medial entorhinal cortex. *Nature Neuroscience* 17:710-718.
- Burak Y, Fiete IR (2009) Accurate path integration in continuous attractor network models of grid cells. *Public Library of Science Computational Biology* 5:e1000291.
- Burgalossi A, Herfst L, Von Heimendahl M, Förste H, Haskic K, Schmidt M, Brecht M (2011) Microcircuits of functionally identified neurons in the rat medial entorhinal cortex. *Neuron* 70:773-786.
- Burgess N (2008) Grid cells and theta as oscillatory interference: theory and predictions. *Hippocampus* 18:1157-1174.
- Burgess N, Barry C, Jeffery KJ, O'Keefe J (2005) A grid and place cell model of path integration utilizing phase precession versus theta. *Computational Cognitive Neuroscience Meeting*, Washington, D.C.
- Burgess N, Barry C, O'Keefe J (2007) An oscillatory interference model of grid cell firing. *Hippocampus* 17:801-812.
- Burton BG, Economo MN, Lee GJ, White JA (2008) Development of theta rhythmicity in entorhinal stellate cells of the juvenile rat. *Journal of Neurophysiology* 100:3144-3157.

- Burwell RD, Amaral DG (1998a) Perirhinal and postrhinal cortices of the rat: interconnectivity and connections with the entorhinal cortex. *Journal of Comparative Neurology* 391:293-321.
- Burwell RD, Amaral DG (1998b) Cortical afferents of the perirhinal, postrhinal, and entorhinal cortices of the rat. *Journal of Comparative Neurology* 398:179-205.
- Burwell RD, Witter MP (2002) Basic anatomy of the parahippocampal region in monkeys and rats. *Parahippocampal Region*. Oxford Press.
- Bush D, Burgess N (2014) A hybrid oscillatory interference/continuous attractor network model of grid cell firing. *Journal of Neuroscience* 34:5065-5079.
- Buzsáki G (2002) Theta oscillations in the hippocampus. *Neuron* 33:325-340.
- Buzsáki G, Leung LW, Vanderwolf CH (1983) Cellular bases of hippocampal EEG in the behaving rat. *Brain Research* 287:139-171.
- Caballero-Bleda M, Witter MP (1993) Regional and laminar organization of projections from the presubiculum and parasubiculum to the entorhinal cortex: an anterograde tracing study in the rat. *Journal of Comparative Neurology* 328:115-129.
- Caeser M, Brown DA, Gähwiler BH, Knöpfel T (1993) Characterization of a calcium-dependent current generating a slow afterdepolarization of CA3 pyramidal cells in rat hippocampal slice cultures. *European Journal of Neuroscience* 5:560-569.
- Canto CB, Witter MP (2012a) Cellular properties of principal neurons in the rat entorhinal cortex. II. The medial entorhinal cortex. *Hippocampus* 22:1277-1299.
- Canto CB, Witter MP (2012b) Cellular properties of principal neurons in the rat entorhinal cortex. I. The lateral entorhinal cortex. *Hippocampus* 22:1256-1276.
- Canto CB, Wouterlood FG, Witter MP (2008) What does the anatomical organization of the entorhinal cortex tell us? *Neural Plasticity* 2008:381243.
- Climer JR, Newman EL, Hasselmo ME (2013) Phase coding by grid cells in unconstrained environments: two-dimensional phase precession. *European Journal of Neuroscience* 38:2526-2541.
- Cole AE, Nicoll RA (1984a) The pharmacology of cholinergic excitatory responses in hippocampal pyramidal cells. *Brain Research* 305:283-290.

Cole AE, Nicoll RA (1984b) Characterization of a slow cholinergic postsynaptic potential recorded in vitro from rat hippocampal pyramidal cells. *Journal of Physiology* 352:173-188.

Colom L V, Castaneda MT, Reyna T, Hernandez S, Garrido-Sanabria E (2005) Characterization of medial septal glutamatergic neurons and their projection to the hippocampus. *Synapse* 58:151-164.

Constanti A, Bagetta G (1991) Muscarinic receptor activation induces a prolonged post-stimulus afterdepolarization with a conductance decrease in guinea-pig olfactory cortex neurones in vitro. *Neuroscience Letters* 131:27-32.

Couey JJ, Witoelar A, Zhang S, Zheng K, Ye J, Dunn B, Czajkowski R, Moser M-B, Moser EI, Roudi Y, Witter MP (2013) Recurrent inhibitory circuitry as a mechanism for grid formation. *Nature Neuroscience* 16:318-324.

Deshmukh SS, Yoganasimha D, Voicu H, Knierim JJ (2010) Theta modulation in the medial and the lateral entorhinal cortices. *Journal of Neurophysiology* 104:994-1006.

Dhillon A, Jones RS (2000) Laminar differences in recurrent excitatory transmission in the rat entorhinal cortex in vitro. *Neuroscience* 99:413-422.

Dickson CT, Alonso A (1997) Muscarinic induction of synchronous population activity in the entorhinal cortex. *Journal of Neuroscience* 17:6729-6744.

Dickson CT, Magistretti J, Shalinsky M, Hamam B, Alonso a (2000a) Oscillatory activity in entorhinal neurons and circuits. Mechanisms and function. *Annals of the New York Academy of Sciences* 911:127-150.

Dickson CT, Magistretti J, Shalinsky MH, Fransén E, Hasselmo ME, Alonso A (2000b) Properties and role of I(h) in the pacing of subthreshold oscillations in entorhinal cortex layer II neurons. *Journal of Neurophysiology* 83:2562-2579.

Dickson CT, Mena AR, Alonso A (1997) Electroresponsiveness of medial entorhinal cortex layer III neurons in vitro. *Neuroscience* 81:937-950.

Dodson PD, Pastoll H, Nolan MF (2011) Dorsal-ventral organization of theta-like activity intrinsic to entorhinal stellate neurons is mediated by differences in stochastic current fluctuations. *Journal of Physiology* 589:2993-3008.

Dolorfo CL, Amaral DG (1998) Entorhinal cortex of the rat: organization of intrinsic connections. *Journal of Comparative Neurology* 398:49-82.

Domnisoru C, Kinkhabwala AA, Tank DW (2013) Membrane potential dynamics of grid cells. *Nature* 495:199-204.

Eacott MJ, Gaffan D, Murray EA (1994) Preserved recognition memory for small sets, and impaired stimulus identification for large sets, following rhinal cortex ablations in monkeys. *European Journal of Neuroscience* 6:1466-1478.

Egorov A V, Hamam BN, Fransén E, Hasselmo ME, Alonso AA (2002) Graded persistent activity in entorhinal cortex neurons. *Nature* 420:173-178.

Eichenbaum H, Lipton PA (2008) Towards a functional organization of the medial temporal lobe memory system: role of the parahippocampal and medial entorhinal cortical areas. *Hippocampus* 18:1314-1324.

Erchova I, Kreck G, Heinemann U, Herz AVM (2004) Dynamics of rat entorhinal cortex layer II and III cells: characteristics of membrane potential resonance at rest predict oscillation properties near threshold. *Journal of Physiology* 560:89-110.

Fernandez de Sevilla D, Buno W (2003) Presynaptic inhibition of Schaffer collateral synapses by stimulation of hippocampal cholinergic afferent fibres. *European Journal of Neuroscience* 17:555-558.

Fernandez de Sevilla D, Cabezas C, De Prada AN, Sanchez-Jimenez A, Buno W (2002) Selective muscarinic regulation of functional glutamatergic Schaffer collateral synapses in rat CA1 pyramidal neurons. *Journal of Physiology* 545:51-63.

Ford TN, Chu KK, Mertz J (2012) Phase-gradient microscopy in thick tissue with oblique back-illumination. *Nature Methods* 9:1195-1197.

Fransén E, Alonso AA, Hasselmo ME (2002) Simulations of the role of the muscarinic-activated calcium-sensitive nonspecific cation current INCM in entorhinal neuronal activity during delayed matching tasks. *Journal of Neuroscience* 22:1081-1097.

Fransén E, Alonso AA, Dickson CT, Magistretti J, Hasselmo ME (2004) Ionic mechanisms in the generation of subthreshold oscillations and action potential clustering in entorhinal layer II stellate neurons. *Hippocampus* 14:368-384.

Fransén E, Tahvildari B, Egorov A V, Hasselmo ME, Alonso AA (2006) Mechanism of graded persistent cellular activity of entorhinal cortex layer v neurons. *Neuron* 49:735-746.

Freund TF (1989) GABAergic septohippocampal neurons contain parvalbumin. *Brain Research* 478:375-381.

- Freund TF, Antal M (1988) GABA-containing neurons in the septum control inhibitory interneurons in the hippocampus. *Nature* 336:170-173.
- Freund TF, Buzsáki G (1996) Interneurons of the hippocampus. *Hippocampus* 6:347-470.
- Fuhs MC, Touretzky DS (2006) A spin glass model of path integration in rat medial entorhinal cortex. *Journal of Neuroscience* 26:4266-4276.
- Fujita Y, Sato T (1964) Intracellular records from hippocampal pyramidal cells in rabbit during theta rhythm activity. *Journal of Neurophysiology* 27:1011-1025.
- Funahashi S, Bruce CJ, Goldman-Rakic PS (1989) Mnemonic coding of visual space in the monkey's dorsolateral prefrontal cortex. *Journal of Neurophysiology* 61:331-349.
- Fuster JM, Jervey JP (1982) Neuronal firing in the inferotemporal cortex of the monkey in a visual memory task. *Journal of Neuroscience* 2:361-375.
- Fyhn M, Molden S, Witter MP, Moser EI, Moser MB (2004) Spatial representation in the entorhinal cortex. *Science* 305:1258-1264.
- Gaffan D, Murray EA (1992) Monkeys (*Macaca fascicularis*) with rhinal cortex ablations succeed in object discrimination learning despite 24-hr intertrial intervals and fail at matching to sample despite double sample presentations. *Behavioral Neuroscience* 106:30-38.
- Garden DL, Dodson PD, O'Donnell C, White MD, Nolan MF (2008) Tuning of synaptic integration in the medial entorhinal cortex to the organization of grid cell firing fields. *Neuron* 60:875-889.
- Gaussier P, Banquet JP, Sargolini F, Giovannangeli C, Save E, Poucet B (2007) A model of grid cells involving extra hippocampal path integration, and the hippocampal loop. *Journal of Integrative Neuroscience* 6:447-476.
- Gil Z, Connors BW, Amitai Y (1997) Differential regulation of neocortical synapses by neuromodulators and activity. *Neuron* 19:679-686.
- Gioanni Y, Rougeot C, Clarke PB, Lepouse C, Thierry AM, Vidal C (1999) Nicotinic receptors in the rat prefrontal cortex: increase in glutamate release and facilitation of mediodorsal thalamo-cortical transmission. *European Journal of Neuroscience* 11:18-30.
- Giocomo LM, Hasselmo ME (2005) Nicotinic modulation of glutamatergic synaptic transmission in region CA3 of the hippocampus. *European Journal of Neuroscience* 22:1349-1356.

Giocomo LM, Hasselmo ME (2008a) Computation by oscillations: implications of experimental data for theoretical models of grid cells. *Hippocampus* 18:1186-1199.

Giocomo LM, Hasselmo ME (2008b) Time constants of h current in layer II stellate cells differ along the dorsal to ventral axis of medial entorhinal cortex. *Journal of Neuroscience* 28:9414-9425.

Giocomo LM, Hasselmo ME (2009) Knock-out of HCN1 subunit flattens dorsal-ventral frequency gradient of medial entorhinal neurons in adult mice. *Journal of Neuroscience* 29:7625-7630.

Giocomo LM, Hussaini SA, Zheng F, Kandel ER, Moser M-B, Moser EI (2011) Grid cells use HCN1 channels for spatial scaling. *Cell* 147:1159-1170.

Giocomo LM, Stensola T, Bonnevie T, Van Cauter T, Moser M-B, Moser EI (2014) Topography of head direction cells in medial entorhinal cortex. *Current Biology* 24:252-262.

Giocomo LM, Zilli EA, Fransén E, Hasselmo ME (2007) Temporal frequency of subthreshold oscillations scales with entorhinal grid cell field spacing. *Science* 315:1719-1722.

Gloveli T, Schmitz D, Empson RM, Dugladze T, Heinemann U (1997) Morphological and electrophysiological characterization of layer III cells of the medial entorhinal cortex of the rat. *Neuroscience* 77:629-648.

Gonzalez-Sulser A, Parthier D, Candela A, McClure C, Pastoll H, Garden D, Surmeli G, Nolan MF (2014) GABAergic projections from the medial septum selectively inhibit interneurons in the medial entorhinal cortex. *Journal of Neuroscience* 34:16739-16743.

Guanella A, Kiper D, Verschure P (2007) A model of grid cells based on a twisted torus topology. *International Journal of Neural Systems* 17:231-240.

Haas JS, White JA (2002) Frequency selectivity of layer II stellate cells in the medial entorhinal cortex. *Journal of Neurophysiology* 88:2422-2429.

Hafting T, Fyhn M, Bonnevie T, Moser M-B, Moser EI (2008) Hippocampus-independent phase precession in entorhinal grid cells. *Nature* 453:1248-1252.

Hafting T, Fyhn M, Molden S, Moser MB, Moser EI (2005) Microstructure of a spatial map in the entorhinal cortex. *Nature* 436:801-806.

Haj-Dahmane S, Andrade R (1996) Muscarinic activation of a voltage-dependent cation nonselective current in rat association cortex. *Journal of Neuroscience* 16:3848-3861.

- Haj-Dahmane S, Andrade R (1998) Ionic mechanism of the slow afterdepolarization induced by muscarinic receptor activation in rat prefrontal cortex. *Journal of Neurophysiology* 80:1197-1210.
- Hajszan T, Alreja M, Leranth C (2004) Intrinsic vesicular glutamate transporter 2-immunoreactive input to septohippocampal parvalbumin-containing neurons: novel glutamatergic local circuit cells. *Hippocampus* 14:499-509.
- Hamam BN, Amaral DG, Alonso AA (2002) Morphological and electrophysiological characteristics of layer V neurons of the rat lateral entorhinal cortex. *Journal of Comparative Neurology* 451:45-61.
- Hamam BN, Kennedy TE, Alonso A, Amaral DG (2000) Morphological and electrophysiological characteristics of layer V neurons of the rat medial entorhinal cortex. *Journal of Comparative Neurology* 418:457-472.
- Hargreaves EL, Rao G, Lee I, Knierim JJ (2005) Major dissociation between medial and lateral entorhinal input to dorsal hippocampus. *Science* 308:1792-1794.
- Hasselmo ME (2006) The role of acetylcholine in learning and memory. *Current Opinion in Neurobiology* 16:710-715.
- Hasselmo ME (2008) Grid cell mechanisms and function: contributions of entorhinal persistent spiking and phase resetting. *Hippocampus* 18:1213-1229.
- Hasselmo ME (2009) A model of episodic memory: mental time travel along encoded trajectories using grid cells. *Neurobiology of Learning and Memory* 92:559-573.
- Hasselmo ME (2013) Neuronal rebound spiking, resonance frequency and theta cycle skipping may contribute to grid cell firing in medial entorhinal cortex. *Philosophical Transactions of the Royal Society of London. Series B, Biological Sciences* 369(1635):20120523.
- Hasselmo ME, Bodelón C, Wyble BP (2002) A proposed function for hippocampal theta rhythm: separate phases of encoding and retrieval enhance reversal of prior learning. *Neural Computation* 14:793-817.
- Hasselmo ME, Bower JM (1992) Cholinergic suppression specific to intrinsic not afferent fiber synapses in rat piriform (olfactory) cortex. *Journal of Neurophysiology* 67:1222-1229.

Hasselmo ME, Brandon MP (2008) Linking cellular mechanisms to behavior: entorhinal persistent spiking and membrane potential oscillations may underlie path integration, grid cell firing, and episodic memory. *Neural Plasticity* 2008:658323.

Hasselmo ME, Giocomo LM, Zilli EA (2007) Grid Cell Firing May Arise From Interference of Theta Frequency Membrane Potential Oscillations in Single Neurons. *Hippocampus* 17:1252-1271.

Hasselmo ME, Schnell E (1994) Laminar selectivity of the cholinergic suppression of synaptic transmission in rat hippocampal region CA1: computational modeling and brain slice physiology. *Journal of Neuroscience* 14:3898-3914.

Hasselmo ME, Schnell E, Barkai E (1995) Dynamics of learning and recall at excitatory recurrent synapses and cholinergic modulation in rat hippocampal region CA3. *Journal of Neuroscience* 15:5249-5262.

Hasselmo ME, Shay CF (2014) Grid cell firing patterns may arise from feedback interaction between intrinsic rebound spiking and transverse traveling waves with multiple heading angles. *Frontiers in Systems Neuroscience* 8:201.

Hasselmo ME, Stern CE (2006) Mechanisms underlying working memory for novel information. *Trends in Cognitive Sciences* 10:487-493.

Hasuo H, Phelan KD, Twery MJ, Gallagher JP (1990) A calcium-dependent slow afterdepolarization recorded in rat dorsolateral septal nucleus neurons in vitro. *Journal of Neurophysiology* 64:1838-1846.

Heys JG, Giocomo LM, Hasselmo ME (2010) Cholinergic modulation of the resonance properties of stellate cells in layer II of medial entorhinal cortex. *Journal of Neurophysiology* 104:258-270.

Heys JG, Hasselmo ME (2012) Neuromodulation of $I(h)$ in layer II medial entorhinal cortex stellate cells: a voltage-clamp study. *Journal of Neuroscience* 32:9066-9072.

Heys JG, MacLeod KM, Moss CF, Hasselmo ME (2013a) Bat and rat neurons differ in theta-frequency resonance despite similar coding of space. *Science* 340:363-367.

Heys JG, Macleod KM, Shay CF, Witter MP, Moss CF, Hasselmo ME (2013b) Neurons in bat entorhinal cortex show an inverse gradient of resonance frequency compared to neurons in rat entorhinal cortex. *Society for Neuroscience Abstract* 39:615.21.

Heys JG, Rangarajan KV, Dombeck DA (2014) The functional micro-organization of grid cells revealed by cellular-resolution imaging. *Neuron* 84:1079-1090.

- Hutcheon B, Yarom Y (2000) Resonance, oscillation and the intrinsic frequency preferences of neurons. *Trends in Neurosciences* 23:216-222.
- Ishizuka N, Weber J, Amaral DG (1990) Organization of intrahippocampal projections originating from CA3 pyramidal cells in the rat. *Journal of Comparative Neurology* 295:580-623.
- Izhikevich EM (2007) *Dynamical systems in neuroscience: The geometry of excitability and bursting*. Cambridge, MA: MIT Press.
- Jeewajee a, Barry C, O'Keefe J, Burgess N (2008) Grid cells and theta as oscillatory interference: electrophysiological data from freely moving rats. *Hippocampus* 18:1175-1185.
- Jeffery KJ, Donnett JG, O'Keefe J (1995) Medial septal control of theta-correlated unit firing in the entorhinal cortex of awake rats. *Neuroreport* 6:2166-2170.
- Jochems A, Reboresda A, Hasselmo ME, Yoshida M (2013) Cholinergic receptor activation supports persistent firing in layer III neurons in the medial entorhinal cortex. *Behavioural Brain Research* 254:108-115.
- Jung MW, Wiener SI, McNaughton BL (1994) Comparison of spatial firing characteristics of units in dorsal and ventral hippocampus of the rat. *Journal of Neuroscience* 14:7347-7356.
- Kamondi A, Aschady L, Wing X-J, Buzsáki G (1998) Theta oscillations in somata and dendrites of hippocampal pyramidal cells in vivo: Activity-dependent phase-precession of action potentials. *Hippocampus* 8:244-261.
- Kerr KM, Agster KL, Furtak SC, Burwell RD (2007) *Functional Neuroanatomy of the Parahippocampal Region : The Lateral and Medial Entorhinal Areas*. *Hippocampus* 17:697-708.
- King C, Recce M, O'Keefe J (1998) The rhythmicity of cells of the medial septum/diagonal band of Broca in the awake freely moving rat: relationships with behaviour and hippocampal theta. *European Journal of Neuroscience* 10:464-477.
- Kiss J, Patel AJ, Baimbridge KG, Freund TF (1990) Topographical localization of neurons containing parvalbumin and choline acetyltransferase in the medial septum-diagonal band region of the rat. *Neuroscience* 36:61-72.
- Kjelstrup KB, Solstad T, Brun VH, Hafting T, Leutgeb S, Witter MP, Moser EI, Moser MB (2008) Finite scale of spatial representation in the hippocampus. *Science* 321:140-143.

- Klausberger T, Magill PJ, Márton LF, Roberts JDB, Cobden PM, Buzsáki G, Somogyi P (2003) Brain-state- and cell-type-specific firing of hippocampal interneurons in vivo. *Nature* 421:844-848.
- Klink R, Alonso A (1993) Ionic mechanisms for the subthreshold oscillations and differential electroresponsiveness of medial entorhinal cortex layer II neurons. *Journal of Neurophysiology* 70:144-157.
- Klink R, Alonso A (1997a) Morphological characteristics of layer II projection neurons in the rat medial entorhinal cortex. *Hippocampus* 7:571-583.
- Klink R, Alonso A (1997b) Muscarinic modulation of the oscillatory and repetitive firing properties of entorhinal cortex layer II neurons. *Journal of Neurophysiology* 77:1813-1828.
- Klink R, Alonso A (1997c) Ionic mechanisms of muscarinic depolarization in entorhinal cortex layer II neurons. *Journal of Neurophysiology* 77:1829-1843.
- Knauer B, Jochems A, Valero-Aracama MJ, Yoshida M (2013) Long-lasting intrinsic persistent firing in rat CA1 pyramidal cells: a possible mechanism for active maintenance of memory. *Hippocampus* 23:820-831.
- Koene RA, Hasselmo ME (2007) First-in-first-out item replacement in a model of short-term memory based on persistent spiking. *Cerebral Cortex* 17:1766-1781.
- Koenig J, Linder AN, Leutgeb JK, Leutgeb S (2011) The spatial periodicity of grid cells is not sustained during reduced theta oscillations. *Science* 332:592-595.
- Koller G, Satzger W, Adam M, Wagner M, Kathmann N, Soyka M, Engel R (2003) Effects of scopolamine on matching to sample paradigm and related tests in human subjects. *Neuropsychobiology* 48:87-94.
- Krnjević K, Pumain R, Renaud L (1971) The mechanism of excitation by acetylcholine in the cerebral cortex. *Journal of Physiology* 215:247-268.
- Kropff E, Treves A (2008) The emergence of grid cells: Intelligent design or just adaptation? *Hippocampus* 18:1256-1269.
- Kunitake A, Kunitake T, Stewart M (2004) Differential modulation by carbachol of four separate excitatory afferent systems to the rat subiculum in vitro. *Hippocampus* 14:986-999.

- Kwag J, Paulsen O (2009) Bidirectional control of spike timing by GABA(A) receptor-mediated inhibition during theta oscillation in CA1 pyramidal neurons. *Neuroreport* 20:1209-1213.
- Leonard BW, Amaral DG, Squire LR, Zola-Morgan S (1995) Transient memory impairment in monkeys with bilateral lesions of the entorhinal cortex. *Journal of Neuroscience* 15:5637-5659.
- Lever C, Jeewajee A, Burton S, O'Keefe J, Burgess N (2009) Hippocampal theta frequency, novelty, and behavior. *Hippocampus*.
- Lisman JE, Idiart MA (1995) Storage of 7 ± 2 short-term memories in oscillatory subcycles. *Science* 267:1512-1515.
- Magee JC (1998) Dendritic hyperpolarization-activated currents modify the integrative properties of hippocampal CA1 pyramidal neurons. *Journal of Neuroscience* 18:7613-7624.
- Magistretti J, Alonso A (1999) Slow voltage-dependent inactivation of a sustained sodium current in stellate cells of rat entorhinal cortex layer II. *Annals of the New York Academy of Sciences* 868:84-87.
- Magistretti J, Ma L, Shalinsky MH, Lin W, Klink R, Alonso A (2004) Spike patterning by Ca^{2+} -dependent regulation of a muscarinic cation current in entorhinal cortex layer II neurons. *Journal of Neurophysiology* 92:1644-1657.
- Manns ID, Mainville L, Jones BE (2001) Evidence for glutamate, in addition to acetylcholine and GABA, neurotransmitter synthesis in basal forebrain neurons projecting to the entorhinal cortex. *Neuroscience* 107:249-263.
- McCormick DA, Prince DA (1985) Two types of muscarinic response to acetylcholine in mammalian cortical neurons. *Proceedings of the National Academy of Sciences of the United States of America* 82:6344-6348.
- McCormick DA, Prince DA (1986) Mechanisms of action of acetylcholine in the guinea-pig cerebral cortex in vitro. *Journal of Physiology* 375:169-194.
- McGaughy J, Koene RA, Eichenbaum H, Hasselmo ME (2005) Cholinergic deafferentation of the entorhinal cortex in rats impairs encoding of novel but not familiar stimuli in a delayed nonmatch-to-sample task. *Journal of Neuroscience* 25:10273-10281.
- McNaughton BL, Battaglia FP, Jensen O, Moser EI, Moser M-B (2006) Path integration and the neural basis of the "cognitive map". *Nature Reviews Neuroscience* 7:663-678.

- Meunier M, Bachevalier J, Mishkin M, Murray EA (1993) Effects on visual recognition of combined and separate ablations of the entorhinal and perirhinal cortex in rhesus monkeys. *Journal of Neuroscience* 13:5418-5432.
- Mhatre H, Gorchetchnikov A, Grossberg S (2012) Grid cell hexagonal patterns formed by fast self-organized learning within entorhinal cortex. *Hippocampus* 22:320-334.
- Mitchell SJ, Ranck JB (1980) Generation of theta rhythm in medial entorhinal cortex of freely moving rats. *Brain Research* 189:49-66.
- Moser EI, Moser M-B (2008) A metric for space. *Hippocampus* 18:1142-1156.
- Naber PA, Lopes da Silva FH, Witter MP (2001) Reciprocal connections between the entorhinal cortex and hippocampal fields CA1 and the subiculum are in register with the projections from CA1 to the subiculum. *Hippocampus* 11:99-104.
- Navaroli VL, Zhao Y, Boguszewski P, Brown TH (2012) Muscarinic receptor activation enables persistent firing in pyramidal neurons from superficial layers of dorsal perirhinal cortex. *Hippocampus* 22:1392-1404.
- Navratilova Z, Giocomo LM, Fellous J-M, Hasselmo ME, McNaughton BL (2012) Phase precession and variable spatial scaling in a periodic attractor map model of medial entorhinal grid cells with realistic after-spike dynamics. *Hippocampus* 22:772-789.
- Nolan MF, Dudman JT, Dodson PD, Santoro B (2007) HCN1 channels control resting and active integrative properties of stellate cells from layer II of the entorhinal cortex. *Journal of Neuroscience* 27:12440-12451.
- Otto T, Eichenbaum H (1992) Complementary roles of the orbital prefrontal cortex and the perirhinal-entorhinal cortices in an odor-guided delayed-nonmatching-to-sample task. *Behavioral Neuroscience* 106:762-775.
- O'Keefe J, Burgess N (2005) Dual phase and rate coding in hippocampal place cells: theoretical significance and relationship to entorhinal grid cells. *Hippocampus* 15:853-866.
- O'Keefe J, Burgess N, Donnett JG, Jeffery KJ, Maguire EA (1998) Place cells, navigational accuracy, and the human hippocampus. *Philosophical Transactions of the Royal Society of London Series B, Biological Sciences* 353:1333-1340.
- O'Keefe J, Dostrovsky J (1971) The hippocampus as a spatial map. Preliminary evidence from unit activity in the freely-moving rat. *Brain Research* 34:171-175.

O'Keefe J, Recce ML (1993) Phase relationship between hippocampal place units and the EEG theta rhythm. *Hippocampus* 3:317-330.

Pastoll H, Solanka L, Van Rossum MCW, Nolan MF (2013) Feedback inhibition enables θ -nested γ oscillations and grid firing fields. *Neuron* 77:141-154.

Penetar DM, McDonough JH (1983) Effects of cholinergic drugs on delayed match-to-sample performance of rhesus monkeys. *Pharmacology, biochemistry, and behavior* 19:963-967.

Petsche H, Stumpf C, Gogolak G (1962) The significance of the rabbit's septum as a relay station between the midbrain and the hippocampus. I. The control of hippocampus arousal activity by the septum cells. *Electroencephalography and Clinical Neurophysiology* 14:202-211.

Poch C, Fuentemilla L, Barnes GR, Düzel E (2011) Hippocampal theta-phase modulation of replay correlates with configural-relational short-term memory performance. *Journal of Neuroscience* 31:7038-7042.

Puil E, Gimbarzevsky B, Miura RM (1986) Quantification of membrane properties of trigeminal root ganglion neurons in guinea pigs. *Journal of Neurophysiology* 55:995-1016.

Quilichini P, Sirota A, Buzsaki G (2010) Intrinsic circuit organization and theta-gamma oscillation dynamics in the entorhinal cortex of the rat. *Journal of Neuroscience* 30:11128-11142.

Radcliffe KA, Fisher JL, Gray R, Dani JA (1999) Nicotinic modulation of glutamate and GABA synaptic transmission of hippocampal neurons. *Annals of the New York Academy of Sciences* 30:591-610.

Ramon y Cajal S (1901a-1902) Estudios sobre la corteza cerebral humana. *Trabajos del Instituto Cajal de Investigaciones Biologicas* 1:1-227.

Ranck JB (1973) Studies on single neurons in dorsal hippocampal formation and septum in unrestrained rats. I. Behavioral correlates and firing repertoires. *Experimental Neurology* 41:461-531.

Ranck JBJ (1984) Head-direction cells in the deep cell layers of dorsal presubiculum in freely moving rats. *Society for Neuroscience Abstract* 10:599.

Reboreda A, Raouf R, Alonso A, Séguéla P (2007) Development of cholinergic modulation and graded persistent activity in layer v of medial entorhinal cortex. *Journal of Neurophysiology* 97:3937-3947.

Remme MW, Lengyel M, Gutkin BS (2009) The role of ongoing dendritic oscillations in single-neuron dynamics. *Public Library of Science Computational Biology* 5:e1000493.

Remme MW, Lengyel M, Gutkin BS (2010) Democracy-independence trade-off in oscillating dendrites and its implications for grid cells. *Neuron* 66:429-437.

Robbins TW, Semple J, Kumar R, Truman MI, Shorter J, Ferraro A, Fox B, McKay G, Matthews K (1997) Effects of scopolamine on delayed-matching-to-sample and paired associates tests of visual memory and learning in human subjects: comparison with diazepam and implications for dementia. *Psychopharmacology (Berlin)* 134:95-106.

Rowland DC, Weible A, Wickersham I, Wu H, Seung H, Mayford MR, Witter MP, Kentros CG (2011) Quantitative mapping of monosynaptic inputs to entorhinal layer II neurons via transgenically-targeted rabies virus suggests a strong direct projection from hippocampal area CA2. *Society for Neuroscience Abstract* 37:513.03.

Rudy B, Fishell G, Lee S, Hjerling-Leffler J (2011) Three groups of interneurons account for nearly 100% of neocortical GABAergic neurons. *Developmental Neurobiology* 71:45-61.

Rutishauser U, Ross IB, Mamelak AN, Schuman EM (2010) Human memory strength is predicted by theta-frequency phase-locking of single neurons. *Nature* 464:903-907.

Sargolini F, Fyhn M, Hafting T, McNaughton BL, Witter MP, Moser MB, Moser EI (2006) Conjunctive representation of position, direction, and velocity in entorhinal cortex. *Science* 312:758-762.

Schmidt-Hieber C, Häusser M (2013) Cellular mechanisms of spatial navigation in the medial entorhinal cortex. *Nature Neuroscience* 16:325-331.

Schmitz D, Gloveli T, Behr J, Dugladze T, Heinemann U (1998) Subthreshold membrane potential oscillations in neurons of deep layers of the entorhinal cortex. *Neuroscience* 85:999-1004.

Schon K, Atri A, Hasselmo ME, Tricarico MD, LoPresti ML, Stern CE (2005) Scopolamine reduces persistent activity related to long-term encoding in the parahippocampal gyrus during delayed matching in humans. *Journal of Neuroscience* 25:9112-9123.

Schon K, Hasselmo ME, Lopresti ML, Tricarico MD, Stern CE (2004) Persistence of parahippocampal representation in the absence of stimulus input enhances long-term encoding: a functional magnetic resonance imaging study of subsequent memory after a delayed match-to-sample task. *Journal of Neuroscience* 24:11088-11097.

Scoville WB, Milner B (1957) Loss of recent memory after bilateral hippocampal lesions. 1957. *Journal of neurology, neurosurgery, and psychiatry* 20:11-21.

Shalinsky MH, Magistretti J, Ma L, Alonso AA (2002) Muscarinic activation of a cation current and associated current noise in entorhinal-cortex layer-II neurons. *Journal of Neurophysiology* 88:1197-1211.

Sharp PE (1996) Multiple spatial/behavioral correlates for cells in the rat postsubiculum: multiple regression analysis and comparison to other hippocampal areas. *Cerebral Cortex* 6:238-259.

Shay CF, Boardman IS, Hasselmo ME (2010) Comparison of resonance and subthreshold membrane potential oscillation properties in whole cell patch recordings in slices of rat medial and lateral entorhinal cortex. *Society for Neuroscience Abstract* 36:101.23.

Shay CF, Boardman IS, James NM, Hasselmo ME (2012) Voltage dependence of subthreshold resonance frequency in layer II of medial entorhinal cortex. *Hippocampus* 22:1733-1749.

Solstad T, Boccara CN, Kropff E, Moser MB, Moser EI (2008) Representation of geometric borders in the entorhinal cortex. *Science* 322:1865-1868.

Squire LR, Stark CEL, Clark RE (2004) The medial temporal lobe. *Annual Review of Neuroscience* 27:279-306.

Stark E, Eichler R, Roux L, Fujisawa S, Rotstein HG, Buzsáki G (2013) Inhibition-induced theta resonance in cortical circuits. *Neuron* 80:1263-1276.

Steffenach H-A, Witter M, Moser M-B, Moser EI (2005) Spatial memory in the rat requires the dorsolateral band of the entorhinal cortex. *Neuron* 45:301-313.

Stensola H, Stensola T, Solstad T, Frøland K, Moser M-B, Moser EI (2012) The entorhinal grid map is discretized. *Nature* 492:72-78.

Stern CE, Sherman SJ, Kirchoff BA, Hasselmo ME (2001) Medial temporal and prefrontal contributions to working memory tasks with novel and familiar stimuli. *Hippocampus* 11:337-346.

Steward O (1976) Topographic organization of the projections from the entorhinal area to the hippocampal formation of the rat. *Journal of Comparative Neurology* 167:285-314.

Stewart M, Fox SE (1990) Do septal neurons pace the hippocampal theta rhythm? *Trends in Neuroscience* 13:163-168.

- Storm JF (1989) An after-hyperpolarization of medium duration in rat hippocampal pyramidal cells. *Journal of Physiology* 409:171-190.
- Suzuki WA, Miller EK, Desimone R (1997) Object and place memory in the macaque entorhinal cortex. *Journal of Neurophysiology* 78:1062-1081.
- Suzuki WA, Zola-Morgan S, Squire LR, Amaral DG (1993) Lesions of the perirhinal and parahippocampal cortices in the monkey produce long-lasting memory impairment in the visual and tactual modalities. *Journal of Neuroscience* 13:2430-2451.
- Swanson LW, Wyss JM, Cowan WM (1978) An autoradiographic study of the organization of intrahippocampal association pathways in the rat. *Journal of Comparative Neurology* 181:681-716.
- Tahvildari B, Alonso A (2005) Morphological and electrophysiological properties of lateral entorhinal cortex layers II and III principal neurons. *Journal of Comparative Neurology* 491:123-140.
- Tahvildari B, Alonso A a, Bourque CW (2008) Ionic basis of ON and OFF persistent activity in layer III lateral entorhinal cortical principal neurons. *Journal of Neurophysiology* 99:2006-2011.
- Tahvildari B, Fransén E, Alonso AA, Hasselmo ME (2007) Switching between “On” and “Off” states of persistent activity in lateral entorhinal layer III neurons. *Hippocampus* 17:257-263.
- Tahvildari B, Wölfel M, Duque A, McCormick DA (2012) Selective functional interactions between excitatory and inhibitory cortical neurons and differential contribution to persistent activity of the slow oscillation. *Journal of Neuroscience* 32:12165-12179.
- Taube JS, Bassett JP (2003) Persistent neural activity in head direction cells. *Cerebral Cortex* 13:1162-1172.
- Taube JS, Muller RU, Ranck Jr JB (1990) Head-direction cells recorded from the postsubiculum in freely moving rats. I. Description and quantitative analysis. *Journal of Neuroscience* 10:420-435.
- Tesche CD, Karhu J (2000) Theta oscillations index human hippocampal activation during a working memory task. *Proceedings of the National Academy of Sciences of the United States of America* 97:919-924.

- Toth K, Borhegyi Z, Freund TF (1993) Postsynaptic targets of GABAergic hippocampal neurons in the medial septum diagonal band of Broca complex. *Journal of Neuroscience* 13:3712-3724.
- Traub RD, Wong RK, Miles R, Michelson H (1991) A model of a CA3 hippocampal pyramidal neuron incorporating voltage-clamp data on intrinsic conductances. *Journal of Neurophysiology* 66:635-650.
- Turchi J, Saunders RC, Mishkin M (2005) Effects of cholinergic deafferentation of the rhinal cortex on visual recognition memory in monkeys. *Proceedings of the National Academy of Sciences of the United States of America* 102:2158-2161.
- Van der Linden S, Lopes da Silva FH (1998) Comparison of the electrophysiology and morphology of layers III and II neurons of the rat medial entorhinal cortex in vitro. *European Journal of Neuroscience* 10:1479-1489.
- Van Groen T, Miettinen P, Kadish I (2003) The entorhinal cortex of the mouse: organization of the projection to the hippocampal formation. *Hippocampus* 13:133-149.
- Vanderwolf CH (1969) Hippocampal electrical activity and voluntary movement in the rat. *Electroencephalography and Clinical Neurophysiology* 26:407-418.
- Varga V, Hangya B, Kránitz K, Ludányi A, Zemankovics R, Katona I, Shigemoto R, Freund TF, Borhegyi Z (2008) The presence of pacemaker HCN channels identifies theta rhythmic GABAergic neurons in the medial septum. *Journal of Physiology* 586:3893-3915.
- Vogt BA, Miller MW (1983) Cortical connections between rat cingulate cortex and visual, motor, and postsubicular cortices. *Journal of Comparative Neurology* 216:192-210.
- Vogt KE, Regehr WG (2001) Cholinergic modulation of excitatory synaptic transmission in the CA3 area of the hippocampus. *Journal of Neuroscience* 21:75-83.
- Wall NR, Wickersham IR, Cetin A, De La Parra M, Callaway EM (2010) Monosynaptic circuit tracing in vivo through Cre-dependent targeting and complementation of modified rabies virus. *Proceedings of the National Academy of Sciences of the United States of America* 107:21848-21853.
- Welday AC, Shlifer IG, Bloom ML, Zhang K, Blair HT (2011) Cosine directional tuning of theta cell burst frequencies: evidence for spatial coding by oscillatory interference. *Journal of Neuroscience* 31:16157-16176.

- Welinder PE, Burak Y, Fiete IR (2008) Grid cells: the position code, neural network models of activity, and the problem of learning. *Hippocampus* 18:1283-1300.
- White JA, Budde T, Kay AR (1995) A bifurcation analysis of neuronal subthreshold oscillations. *Biophysical Journal* 69:1203-1217.
- Wickersham IR, Sullivan HA, Seung HS (2010) Production of glycoprotein-deleted rabies viruses for monosynaptic tracing and high-level gene expression in neurons. *Nature Protocols* 5:595-606.
- Wills TJ, Barry C, Cacucci F (2012) The abrupt development of adult-like grid cell firing in the medial entorhinal cortex. *Frontiers in Neural Circuits* 6:21.
- Winson J (1978) Loss of hippocampal theta rhythm results in spatial memory deficit in the rat. *Science* 201:160-163.
- Witter MP (1993) Organization of the entorhinal-hippocampal system: a review of current anatomical data. *Hippocampus* 3:33-44.
- Witter MP (2007) The perforant path: projections from the entorhinal cortex to the dentate gyrus. *Progress in Brain Research* 163:43-61.
- Witter MP, Amaral DG (1991) Entorhinal cortex of the monkey. 5. Projections to the dentate gyrus, hippocampus and subicular complex. *Journal of Comparative Neurology* 307:437-459.
- Witter MP, Griffioen AW, Jorritsma-Byham B, Krijnen JLM (1988) Entorhinal projections to the hippocampal CA1 region in the rat: an underestimated pathway. *Neuroscience Letters* 85:193-198.
- Witter MP, Groenewegen HJ, Lopes da Silva FH, Lohman AH (1989) Functional organization of the extrinsic and intrinsic circuitry of the parahippocampal region. *Progress in Neurobiology* 33:161-253.
- Witter MP, Moser EI (2006) Spatial representation and the architecture of the entorhinal cortex. *Trends in Neurosciences* 29:671-678.
- Woodhall GL, Bailey SJ, Thompson SE, Evans DIP, Jones RSG (2005) Fundamental differences in spontaneous synaptic inhibition between deep and superficial layers of the rat entorhinal cortex. *Hippocampus* 15:232-245.
- Yamada-Hanff J, Bean BP (2013) Persistent sodium current drives conditional pacemaking in CA1 pyramidal neurons under muscarinic stimulation. *The Journal of Neuroscience* 33:15011-15021.

Yartsev MM, Witter MP, Ulanovsky N (2011) Grid cells without theta oscillations in the entorhinal cortex of bats. *Nature* 479:103-107.

Yee BK, Rawlins JN (1998) A comparison between the effects of medial septal lesions and entorhinal cortex lesions on performance of nonspatial working memory tasks and reversal learning. *Behavioural Brain Research* 94:281-300.

Yoganarasimha D, Rao G, Knierim JJ (2011) Lateral entorhinal neurons are not spatially selective in cue-rich environments. *Hippocampus* 21:1363-1374.

Yoshida M, Giocomo LM, Boardman I, Hasselmo ME (2011) Frequency of subthreshold oscillations at different membrane potential voltages in neurons at different anatomical positions on the dorsoventral axis in the rat medial entorhinal cortex. *Journal of Neuroscience* 31:12683-12694.

Yoshida M, Hasselmo ME (2009) Persistent firing supported by an intrinsic cellular mechanism in a component of the head direction system. *Journal of Neuroscience* 29:4945-4952.

Zhang Z, Rebores A, Alonso A, Barker PA, Séguéla P (2011) TRPC channels underlie cholinergic plateau potentials and persistent activity in entorhinal cortex. *Hippocampus* 21:386-397.

Zilli EA, Hasselmo ME (2010) Coupled noisy spiking neurons as velocity-controlled oscillators in a model of grid cell spatial firing. *Journal of Neuroscience* 30:13850-13860.

Zilli EA, Yoshida M, Tahvildari B, Giocomo LM, Hasselmo ME (2009) Evaluation of the oscillatory interference model of grid cell firing through analysis and measured period variance of some biological oscillators. *Public Library of Science Computational Biology* 5:e1000573.

Zola-Morgan S, Squire LR, Amaral DG (1989a) Lesions of the hippocampal formation but not lesions of the fornix or the mammillary nuclei produce long-lasting memory impairment in monkeys. *Journal of Neuroscience* 9:898-913.

Zola-Morgan S, Squire LR, Amaral DG, Suzuki WA (1989b) Lesions of perirhinal and parahippocampal cortex that spare the amygdala and hippocampal formation produce severe memory impairment. *Journal of Neuroscience* 9:4355-4370.

CURRICULUM VITAE

CHRISTOPHER SHAY

Boston University
Graduate Program in Neuroscience
2 Cummington Mall Boston, MA

neuronerd9@gmail.com
Mobile: 603.819.9708

YOB: 1986

Education

2009-2015 Ph.D. in Neuroscience (Expected), Boston University

2004-2009 BS in Behavioral Neuroscience, Northeastern University

Research Experience

- 2009-Present Graduate Student, Center for Memory and Brain, Boston University
Research Advisor: Dr. Michael Hasselmo
- Characterized and compared the voltage dependence of resonance in cells of the medial and lateral entorhinal cortex along their respective anatomical axes to elucidate functional relevance to spatial processing in the two brain regions.
 - Investigated post-inhibitory rebound spiking properties of medial entorhinal neurons to test predictions of a computational model generating grid cell spatial periodicity.
 - Characterized cholinergic modulation of persistent spiking and afterdepolarization properties in principal cells of medial entorhinal cortex.
- 2008-2009 Biology Research Assistant, Molecular Insight Pharmaceuticals, Cambridge, MA
- Screened potential inhibitors for an enzyme up-regulated in hypoxic conditions associated with malignant solid tumors.
 - Conducted bio-distribution studies in tumor bearing mice and rats to characterize novel radiolabeled compounds with potential use in cancer diagnostic and therapeutics.
 - Performed in vitro radiolabeled cell binding assays.

- Maintained various cancer cell lines used for animal injections as well as in vitro studies.

2005-2008

Research Assistant, Department of Psychology, Northeastern University

- Learned and executed research protocols and experiments pertinent to cocaine drug abuse: drug reward, its effects on learning, as well as effects on behavior and locomotion.
- Conducted Radioligand Binding Assays as well as behavioral assays in effort to characterize numerous drugs for their anti-depressant properties.
- Studied transgenic mice expressing accessory protein coded by HIV and helped find potential relationship between the TAT protein and increased drug abuse among HIV patients.

Publications

1. Hasselmo ME, **Shay CF** (2014) Grid cell firing patterns may arise from feedback interaction between intrinsic rebound spiking and transverse traveling waves with multiple heading angles. *Frontiers in Systems Neuroscience* 8:201.
2. Paris JJ, Carey AN, **Shay CF**, Gomes SM, He JJ, McLaughlin JP (2014) Effects of conditional central expression of HIV-1 tat protein to potentiate cocaine-mediated psychostimulation and reward among male mice. *Neuropsychopharmacology* 39:380–388.
3. Heys JG, Schultheiss NW, **Shay CF**, Tsuno Y, Hasselmo ME (2012) Effects of acetylcholine on neuronal properties in entorhinal cortex. *Frontiers in Behavioral Neuroscience* 6:32.
4. Newman EL, **Shay CF**, Hasselmo ME (2012) Malignant synaptic growth and Alzheimer's disease. *Future Neurology* 7:557–571.
5. **Shay CF**, Boardman IS, James NM, Hasselmo ME (2012) Voltage dependence of subthreshold resonance frequency in layer II of medial entorhinal cortex. *Hippocampus* 22:1733–1749.
6. Carey AN, Lyons AM, **Shay CF**, Dunton O, McLaughlin JP (2009) Endogenous kappa opioid activation mediates stress-induced deficits in learning and memory. *Journal of Neuroscience* 29:4293–4300.

Publications Under Review

1. **Shay CF**, Ferrante M, Chapman IV GW, Hasselmo ME. Rebound spiking in layer II medial entorhinal cortex stellate cells: possible mechanism of grid cell function (Under review).
2. Heys JG, **Shay CF**, Macleod KM, Witter MP, Moss CF, Hasselmo ME. Physiological properties of neurons in bat medial entorhinal cortex exhibit an inverse gradient along the dorsal-ventral axis compared to medial entorhinal neurons in rat (Under review).
3. Ferrante M, **Shay CF**, Tsuno Y, Chapman IV GW, Hasselmo ME. Post-inhibitory rebound spikes in rat medial entorhinal cortex may contribute to grid cell generation (Under review).

Abstracts for Conference Presentations

1. **Shay CF**, Ferrante M, Chapman IV GW, Hasselmo ME (2014) Layer II medial entorhinal cortex stellate cells in rat display phase specific post-inhibitory rebound spiking properties. Society for Neuroscience Abstract 40:297.08.
2. Ferrante M, **Shay CF**, Tsuno Y, Chapman IV GW, Hasselmo ME (2014) Post-inhibitory rebound spikes in rat MEC layer II/III principal cells: In-vivo, in-vitro, and in-silico evidence and characterization. Society for Neuroscience Abstract 40:297.11.
3. Heys JG, Macleod KM, **Shay CF**, Witter MP, Moss CF, Hasselmo ME (2013) Neurons in bat entorhinal cortex show an inverse gradient of resonance frequency compared to neurons in rat entorhinal cortex. Society for Neuroscience Abstract 39:615.21.
4. **Shay CF**, Boardman IS, James, NM, Hasselmo ME (2011) Comparison of resonance frequency at different membrane potentials in rat medial and lateral entorhinal cortex. Society for Neuroscience Abstract 37:730.12.
5. **Shay CF**, Boardman IS, Hasselmo ME (2010) Comparison of resonance and subthreshold membrane potential oscillation properties in whole cell patch recordings in slices of rat medial and lateral entorhinal cortex. Society for Neuroscience Abstract 36:101.23.
6. Hillier SM, Lu G, **Shay C**, Maresca KP, Barone C, Zimmerman CN, Eckelman WC, Joyal JL, Babich JW (2009) Small molecule carbonic anhydrase IX inhibitors for targeted molecular imaging of cancer. Journal of Nuclear Medicine 50:1561.
7. Carey AN, **Shay CF**, McLaughlin, JP (2008) Potentiation of drug reward in a mouse model expressing HIV-Tat protein. AAAS Annual Meeting, Boston MA.

8. Carey AN, **Shay CF**, He JJ, McLaughlin JP (2006) HIV accessory protein impairs learning and memory but potentiates cocaine reward. International Narcotic Research Conference, St. Paul, MN.

Awards and Funding

2009-Present Research Assistantship, Boston University

2008 AAAS Student Poster Award Winner--First Place, Brain and Behavior

2004-2009 Presidential Scholarship, Northeastern University

References

Michael Hasselmo, Boston University, Hasselmo@gmail.com